Symmetric cladding thin-film waveguides

vorgelegt von

M.Sc. Karsten Simon Pufahl

ORCID: 0000-0003-4983-8480

von der Fakultät II — Mathematik und Naturwissenschaften
der Technischen Universität Berlin
zur Erlangung des akademischen Grades

Doktor der Naturwissenschaften
— Dr. rer. nat. —

genemigte Dissertation

Promotionsausschuss:
Vorsitzender: Prof. Dr. rer. nat. Andreas Knorr (TU Berlin)
Gutachterin: Prof. Dr. rer. nat. Ulrike Woggon (TU Berlin)
Gutachter: Prof. Dr. rer. nat. Kurt Busch (HU Berlin)
Gutachter: Prof. Dr. rer. nat. Michael Gradzielski (TU Berlin)

Tag der wissenschaftlichen Aussprache: 14. November 2019

Berlin 2020

Abstract

Intrinsic absorption is often considered an undesirable effect in waveguiding applications, severely limiting the propagation length. However, with appropriate design of a symmetric cladding, waveguiding can be achieved even with highly absorbing media, to the degree that increasing absorption has a positive effect on the propagation length. Here, this counterintuitive concept is developed further and put into perspective with long-range surface plasmon polaritons and TM waveguide modes. The range of accessible optical properties is discussed and the fitness of materials for symmetric cladding thin-film waveguides is calculated.

The concept of waveguiding in lossy materials is transferred to thin-films of disordered nano-composites. Experimental data of waveguides made from gold nano-particle incubated polymer brush film is presented. Poly(N-isopropylacrylamide) (PNIPAM) based functionalized surfaces are able to support symmetric cladding thin-film waveguide modes in spite of their disorder and material loss. The PNIPAM surface can be made to change its thickness and permittivity depending on a variety of environmental parameters. Waveguides made from polymer brushes may bring new optical sensing devices that combine the versatility of nano-engineered functionalized films with the well- defined propagation of thin film waveguides.

An attenuated total reflectance (ATR) geometry is used for k-space spectroscopy to prove the existence of modal solutions in the samples and to map out their dispersion. A white-light interferometry technique was developed to stabilize and control the evanescent coupling gap with nanometer precision.

Last, the limits of ATR spectroscopy are explored. Using a quantum optical approach the ultimate sensitivity of ATR based methods such as surface plasmon resonance sensing

(SPRS) is derived. Optical illumination and detection modes are shown that perform *optimally* in the sense that they extract refractive index changes with unsurpassable signal-to-noise ratio. A comparison with commercial-grade SPRS devices is given, revealing the potential of using symmetric cladding thin-film waveguides and optimized sensing modes.

Zusammenfassung

Intrinsische Absorption wird in Wellenleiteranwendungen oft als ein unerwünschter Effekt angesehen, der die Propagationslänge stark beschränkt. Bei Verwendung eines symmetrischen Claddings kann jedoch auch bei stark absorbierenden Medien ein Wellenleitung erreicht werden, so dass sich sogar steigende Absorption positiv auf die Propagationslänge auswirkt. Dieses kontraintuitive Konzept wird hier weiterentwickelt und mit langreichweitigen Oberflächenplasmon-Polaritonen und TM-Wellenleitermoden in Verbindung gebracht. Der Bereich zugänglicher optischer Eigenschaften wird diskutiert und die Eignung von Materialien für symmetrische Dünnschichtwellenleitung berechnet.

Das Konzept der Wellenleitung in verlustbehafteten Materialien wird auf Dünnschichten von ungeordneten Nanokompositen erweitert. Experimentelle Daten von Wellenleitern aus Gold Nanopartikel inkubierten Polymer-Bürstenfilmen werden vorgestellt. Diese auf Poly(N-isopropylacrylamid) (PNIPAM) basierenden funktionalisierten Oberflächen sind in der Lage, trotz ihrer Unordnung und ihres Materialverlustes symmetrische Dünnschichtwellenleitermoden auszubilden. Die PNIPAM-Oberflächen kann so gestaltet werden, dass sie ihre Dicke und Permittivität in Abhängigkeit von einer Vielzahl von Umgebungsparametern ändert. Wellenleiter aus Polymerbürsten könnten neue optische Sensoranwendungen hervorbringen, die die Vielseitigkeit von nanotechnologisch funktionalisierten Schichten mit der wohldefinierten Ausbreitung von Dünnschichtwellenleitern kombinieren.

Eine Abgeschwächte Totalreflexionsgeometrie (ATR) wird für die k-Raumspektroskopie verwendet, um die Existenz modaler Lösungen in den Proben nachzuweisen und deren Dispersion abzubilden. Eine Weißlichtinterferometrietechnik wurde entwickelt, um den evaneszenten Kopplungsabstand mit Nanometer Genauigkeit zu stabilisieren und

zu kontrollieren.

Schließlich werden die Grenzen der ATR Spektroskopie erforscht. Unter Verwendung eines quantenoptischen Ansatzes wird die ultimative Empfindlichkeit von ATR-basierten Methoden wie der Oberflächenplasmonresonanzspektroskopie abgeleitet. Es werden optische Beleuchtungs- und Detektionsmoden hergeleitet, die *optimal* in dem Sinne funktionieren, dass sie Anderungen des Brechungsindex mit einem unübertroffenen Signal-Rausch-Verhältnis extrahieren. Ein Vergleich mit kommerziellen SPRS Geräten zeigt das Potenzial der Verwendung vonsymmetrischen Dünnschichtwellenleiter und optimierten Modenprofilen.

Contents

List of Figures

Acronyms

Au-Np gold nano-particle

ADC analog-to-digital converter

AFM atomic force microscopy

ATR attenuated total reflectance

CCD charge-coupled device

ENZ epsilon near zero

GD group delay

GDD group delay dispersion

NIR near-infrared

LED light-emitting diode

LO local oscillator

LRSPP long-range surface plasmon polariton

LSPR localized surface plasmon resonance

PNIPAM poly(N-isopropylacrylamide)

PVD physical vapor deposition

QNL quantum noise limit

QST quantum state tomography

RIU Refractive index unit

SEM scanning electron microscopy

SCTW symmetric cladding thin-film waveguide

SISPP single-interface surface plasmon polariton

SNOM scanning near-field optical microscope

SNR signal-to-noise ratio

SPP surface plasmon polariton

TIR total internal reflectance

TMD transition metal dichalcogenide

VIS visible

Introduction

Optical waveguiding is one of the main building blocks of photonics and has become an indispensable part in almost all of today's optical communication devices and sensors.[1] To fulfill the ongoing demand for miniaturization of photonic devices, advanced techniques for sub-wavelength focusing and guiding of light are required. In the field of integrated photonics, metals play an important role: Their combination with dielectrics allows light to be confined far below its free-space wavelength.[2–5] Although electromagnetic properties of metals have been studied for a long time, new and unexpected findings in plasmonics are still being discovered. Metal nano-structures, with their outstanding ability to manipulate the propagation and polarization of light, show fascinating optical effects and can be used to construct planar optical elements.[6–9] Although radio frequency engineering and plasmonic research are founded on the same set of equations, only the latter can exploit the unique permittivity of metals in the visible (VIS) and near-infrared (NIR) spectrum. Approaching the optical frequency range, the electron inertia becomes relevant, resulting in an outstanding material response. The electrons lag behind the exciting field, thereby oscillating almost fully *out of phase*. This delayed polarization illustrates the biggest strength but also weakness of plasmonics. An out of phase polarization allows unique and mirrored electromagnetic fields that are impossible to achieve otherwise. However, a polarization not *fully* out of phase causes optical losses that eventually turn into unwanted heat.

Tremendous efforts have been undertaken to reduce the losses in plasmonic materials. While there was significant progress in improving the preparation techniques and reducing the losses, Khurgin [10] has shown that quantum mechanics limits the ultimate field confinement with metals. The free electrons are both the cause and the limiting boundary here, as inevitable loss remains from the evanescent confinement of carriers.

Optical losses are an integral part of light-matter interaction. From the Kramers–Kronig relations it is known that there is no optical response without absorption. Any material with a refractive index different from unity, will be an absorbing one.

A first glance unconventional and counterintuitive approach towards dealing with optical loss has been taken by Kovacs [11] and Yang et al. [12] who have used materials with extremely high absorption to build low-loss waveguides. If the absorbing material is prepared as a thin film with symmetric cladding, the propagation length of modes can exceed the material's bulk absorption length by orders of magnitude. In contrast to plane waves, the propagation length of these waveguide modes even benefits from increasing the absorption.

Since its discovery, waveguiding with strong absorbers has been considered in only a limited number of works.[13–17] In spite of its similarities with long-range surface plasmon polaritons, waveguiding with strong absorbers has remained outside the scope of plasmonic research. To some extent this is due to the unfortunate name "long-range surface exciton polariton" that was given to the mode. Since excitons are neither adequate nor necessary for the mode, the term is misleading. A comprehensive study on the influence of losses over a wide permittivity range has hitherto been lacking. Obtaining a deeper understanding of low-loss propagation in symmetric cladding thin-film waveguides is key for further application in novel nano-photonic surfaces or active materials for the purpose of quantum-optical effects.

This thesis aims to put waveguiding with absorbing materials into perspective and demonstrate their potential use for the next generation of attenuated total reflectance (ATR) based optical sensing.

The first two chapters will lay the theoretical groundwork for symmetric cladding thin-film waveguides. The theoretical part focuses on the influence of the permittivity on thin-film waveguiding. In particular, how material loss is transferred into propagation loss of modes is discussed. Available values of permittivity in nature are discussed in the *permittivity landscape* together with the suitability of individual materials.

Chapter 3 describes an ATR spectroscopy method for the excitation and detection of modes in thin-films. A white-light interferometry technique is presented that allows nanometer control of evanescent coupling gaps. The method is a valuable tool to

investigate the modal propagation properties with broad-band ATR spectroscopy.

In chapter 4, the concept of symmetric cladding thin-film waveguiding is transferred to functionalized polymer brush materials. These novel materials allow in-situ tuning of permittivity and thickness. It is shown that such materials – despite optical loss and disorder – are a promising platform for the design of reconfigurable waveguides and optical sensors for the field of life-sciences.

The quantum mechanical limits of ATR-based sensing are explored in the final chapter. Here, a full quantum optics approach is employed to derive the ultimate sensitivity limit of ATR spectroscopy. It is revealed that from a quantum optics perspective, large improvements are within reach by optimizing the optical modes in the excitation and detection of an ATR setup.

This work can serve as a guide to the design of new ATR-based sensing devices. Starting with the influence of lossy permittivities on symmetric cladding thin-film waveguiding, the range of accessible permittivities is given together with a performance benchmark for most available optical materials. White-light interferometry techniques for precise ATR waveguide coupling are shown together with perspectives on the use of new soft-matter functionalized surfaces. Lastly, quantum optics is employed to derive anticipated sensitivities and to relate them to available commercial technology.

For the design of symmetric cladding thin-film waveguides, material losses can be leveraged to become an intentional design parameter rather than an unsuppressible burden. It is envisioned that changing the perspective on optical losses in materials will bring up functional optical waveguides including new and more sensitive integrated photonic sensors.

Since parts of this work have already been prepublished,[18,19] some overlap to parts of this dissertation may arise. Related publications are listed at the end of this thesis.

Chapter 1

Surface waves and thin-film waveguiding

The existence of surface waves is intimately connected to the behavior of electromagnetic fields at boundaries. In particular, the contrast of material responses allows for a strongly confined field in the vicinity of a boundary. Provided that the right material combination is used, even a single interface is sufficient to create a bound mode that propagates along the interface with subwavelength lateral confinement.

1.1 Single interface surface waves

For the theoretical description of interface waves, we will restrict ourselves to a 2D description and align all of the interfaces either with the x, y-plane or parallel thereto. In the case of a single interface, two media are assumed to be semi-infinite, sharing a common interface in the x, y-plane. At least one of the two material responses, the permittivity ε and the permeability μ is required to be discontinuous at the interface, otherwise the interface would be fully transparent and without relevance. We can rule out a discontinuity in the permeability μ, as magnetic material responses have a limited frequency range, which does not extend up to the optical regime. The focus of this work will, therefore, lie solely on permittivity contrasts.

The permittivities are assumed to be piecewise homogeneous and isotropic in each media with ε_1 and ε_2 denoting the permittivity in the upper half-space ($z > 0$) and lower half-space ($z < 0$), respectively. The symmetry allows us to consider only waves propa-

gating along the x-direction without losing generality. For time harmonic fields, the Maxwell equations provide a set of six time-independent equations in either medium[a]

$$\begin{aligned}
\frac{\partial E_z}{\partial y} - \frac{\partial E_y}{\partial z} &= i\omega\mu_0 H_x & \frac{\partial H_z}{\partial y} - \frac{\partial H_y}{\partial z} &= -i\omega\varepsilon\varepsilon_0 E_x \\
\frac{\partial E_x}{\partial z} - \frac{\partial E_z}{\partial x} &= i\omega\mu_0 H_y & \frac{\partial H_x}{\partial z} - \frac{\partial H_z}{\partial x} &= -i\omega\varepsilon\varepsilon_0 E_y \\
\frac{\partial E_y}{\partial x} - \frac{\partial E_x}{\partial y} &= i\omega\mu_0 H_z & \frac{\partial H_y}{\partial x} - \frac{\partial H_x}{\partial y} &= -i\omega\varepsilon\varepsilon_0 E_z.
\end{aligned} \tag{1.1}$$

The superposition principle allows the fields to be split into transverse magnetic (TM) and transverse electric (TE) in order to solve each of them individually. TM waves have a magnetic field that is at any time orthogonal to the direction of propagation which is denoted by their k-vector. The TM wave is not guaranteed to be a transversal one, as the electrical field can have a longitudinal component along the direction of propagation. TE waves represent the opposite case, with a fully transverse electrical field and an optionally longitudinal component in the magnetic field. We can then separate the field and simplify the previous equation system for the TM case ($H_x = 0$):

$$E_x = -i\frac{1}{\omega\varepsilon\varepsilon_0}\frac{\partial H_y}{\partial z} \qquad E_z = i\frac{1}{\omega\varepsilon\varepsilon_0}\frac{\partial H_y}{\partial x} \tag{1.2}$$

with the corresponding wave equation

$$\frac{\partial^2 H_y}{\partial z^2} + (k_0^2\varepsilon - i\frac{\partial^2}{\partial x^2})H_y = 0. \tag{1.3}$$

Analogous thereto, the TE mode ($E_x = 0$):

$$H_x = i\frac{1}{\omega\mu\mu_0}\frac{\partial E_y}{\partial z} \qquad H_z = -i\frac{1}{\omega\mu\mu_0}\frac{\partial E_y}{\partial x} \tag{1.4}$$

with its wave equation

$$\frac{\partial^2 E_y}{\partial z^2} + (k_0^2\varepsilon - i\frac{\partial^2}{\partial x^2})E_y = 0. \tag{1.5}$$

Before continuing with an ansatz for a surface wave, we briefly revisit what is expected from a surface wave. We require confinement to the surface and vanishing amplitudes in the far-field:

$$E_{x,y,z}(z \to \pm\infty) = H_{x,y,z}(z \to \pm\infty) = 0. \tag{1.6}$$

[a]The mathematical introduction to surface waves is based on work by Maier [20] and shares the notation with a few minor exceptions.

The mode should furthermore have a finite norm to be meaningful and of practical relevance. With these two assumptions, we have restricted the description to bound modes thereby explicitly excluding leaky modes that have an evanescent profile growing away from the interface. It should be borne in mind, that leaky modes are not completely meaningless. They are useful in describing the coupling between far-field radiation and a bound mode.

For the TE wave or *s*-polarization we employ the following ansatz for the electrical fields

$$\begin{aligned} E_y^{(1)}(x,z) &= A^{(1-)}\mathrm{e}^{i\mathbf{k}_1^- \cdot \mathbf{r}} + A^{(1+)}\mathrm{e}^{i\mathbf{k}_1^+ \cdot \mathbf{r}} \\ E_y^{(2)}(x,z) &= A^{(2+)}\mathrm{e}^{i\mathbf{k}_2^+ \cdot \mathbf{r}} + A^{(2-)}\mathrm{e}^{i\mathbf{k}_2^- \cdot \mathbf{r}} \end{aligned} \tag{1.7}$$

and the magnetic fields

$$\begin{aligned} H_x^{(1)}(x,z) &= A^{(1-)}\frac{k_{1z}}{\omega\mu_0\mu_1}\mathrm{e}^{i\mathbf{k}_1^- \cdot \mathbf{r}} + A^{(1+)}\frac{-k_{1z}}{\omega\mu_0\mu_1}\mathrm{e}^{i\mathbf{k}_1^+ \cdot \mathbf{r}} \\ H_x^{(2)}(x,z) &= A^{(2+)}\frac{-k_{2z}}{\omega\mu_0\mu_2}\mathrm{e}^{i\mathbf{k}_2^+ \cdot \mathbf{r}} + A^{(2-)}\frac{k_{2z}}{\omega\mu_0\mu_2}\mathrm{e}^{i\mathbf{k}_2^- \cdot \mathbf{r}} \end{aligned} \tag{1.8}$$

where $\mathbf{k}_1^{\pm} = (k_{1x}, 0, \pm k_{1z})$ and $\mathbf{k}_2^{\pm} = (k_{2x}, 0, \pm k_{2z})$ are complex k-vectors with positive real and imaginary parts in the respective medium. $A^{(1\pm)}$ and $A^{(2\pm)}$ are the electrical field amplitudes in the upper and lower half-space, respectively. The superscript denotes upward (+) and downward (−) propagation. We can exclude components scaling with $A^{(1+)}$ and $A^{(2-)}$ as they are decaying toward the interface rather than away from it. Even in the case of a fully real-valued in-plane k-vector, the fields at $\pm\infty$ do not vanish. It is therefore justified to exclude these terms in the ansatz.

Finding waveguiding modes is essentially a puzzle of boundary conditions. The single interface case is, however, still quite simple. Additional interfaces increase the complexity, and finding a solution for all cases quickly becomes a cumbersome task without the help of numerical methods.

The continuity of the fields requires the following conditions for the normal and tangential components[21]

$$\begin{aligned} \hat{\mathbf{n}}_{12} \times \left(\mathbf{E}^{(2)} - \mathbf{E}^{(1)}\right) &= 0 \\ \hat{\mathbf{n}}_{12} \times \left(\mathbf{H}^{(2)} - \mathbf{H}^{(1)}\right) &= \mathbf{J}_s \end{aligned}$$

$$\begin{aligned}\hat{\mathbf{n}}_{12} \cdot \left(\mathbf{D}^{(2)} - \mathbf{D}^{(1)}\right) &= \rho_s \\ \hat{\mathbf{n}}_{12} \cdot \left(\mathbf{B}^{(2)} - \mathbf{B}^{(1)}\right) &= 0 \end{aligned} \tag{1.9}$$

where $\hat{\mathbf{n}}_{12}$ is the interface surface normal vector pointing toward the second medium. The Maxwell equations are flexible here and allow some hypothetical surface currents $\mathbf{J}_s$ and surface charges ρ_s along the interface. We will disregard them, although they can be useful for modeling interface roughness.[22] Application of the boundary conditions to the E-field yields

$$A^{(1+)} + A^{(2-)} = 0, \tag{1.10}$$

which is used together with the condition of the H-fields, yielding

$$\frac{k_{1z}}{\mu_1} + \frac{k_{2z}}{\mu_2} = 0. \tag{1.11}$$

This condition, however, cannot be met. It either requires permeabilities or k_z-components of opposite sign opposite signs. However, the permeabilities have been assumed to be of unity. A negative k_z is not allowed either, as that would not be a bound mode, but a leaky one, diverging on one side of the interface. This shows that a TE polarized surface wave does not exist unless the permeability is negative on one side of the interface. It is noted that such surface waves have however been demonstrated for microwave frequencies.[23]

In analogy to the above calculation, the TM-case can be processed with the ansatz

$$\begin{aligned} H_y^{(1)}(x,z) &= A^{(1-)} e^{i\mathbf{k}_1^- \cdot \mathbf{r}} + A^{(1+)} e^{i\mathbf{k}_1^+ \cdot \mathbf{r}} \\ H_y^{(2)}(x,z) &= A^{(2+)} e^{i\mathbf{k}_2^+ \cdot \mathbf{r}} + A^{(2-)} e^{i\mathbf{k}_2^- \cdot \mathbf{r}} \end{aligned} \tag{1.12}$$

and

$$\begin{aligned} E_x^{(1)}(x,z) &= A^{(1-)} \frac{k_{1z}}{\omega\mu_0\mu_1} e^{i\mathbf{k}_1^- \cdot \mathbf{r}} + A^{(1+)} \frac{-k_{1z}}{\omega\mu_0\mu_1} e^{i\mathbf{k}_1^+ \cdot \mathbf{r}} \\ E_x^{(2)}(x,z) &= A^{(2+)} \frac{-k_{2z}}{\omega\mu_0\mu_2} e^{i\mathbf{k}_2^+ \cdot \mathbf{r}} + A^{(2-)} \frac{k_{2z}}{\omega\mu_0\mu_2} e^{i\mathbf{k}_2^- \cdot \mathbf{r}}, \end{aligned} \tag{1.13}$$

resulting in a more promising condition that involves the permittivities rather than the permeabilities

$$\frac{k_{1z}}{\varepsilon_1} + \frac{k_{2z}}{\varepsilon_2} = 0. \tag{1.14}$$

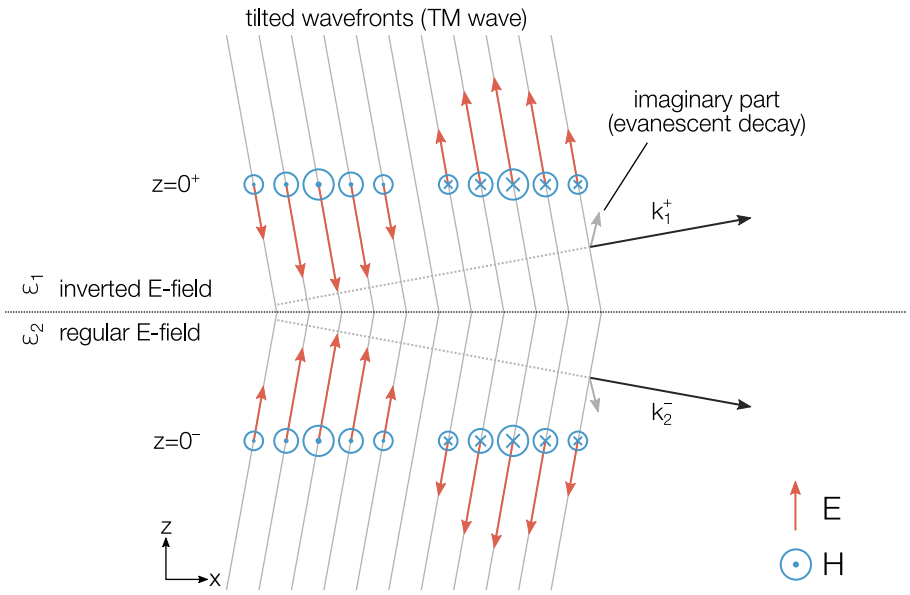

Figure 1.1: E and H-field of a surface wave between a metallic ($\varepsilon_1' \leq -1$) and a dielectric ($\varepsilon_2' \geq 1$) medium. The boundary conditions enforce that one or other of the media needs an E-field which is inverted. Evanescent k-vectors pointing away from the interface are otherwise impossible to construct.

Unlike in the TE-case, this is not an a priori contradiction to which a solution cannot be found. The boundary conditions require the in-plane components to match alongside the interface, giving $k_{1x} = k_{2x} = k_x$. The wave equation can be used to relate the lateral components k_z with the permittivity

$$\begin{aligned} \mathbf{k_1^-} \cdot \mathbf{k_1^-} &= k_x^2 + k_{1z}^2 = \omega^2 \mu_0 \varepsilon_0 \varepsilon_1 \\ \mathbf{k_2^+} \cdot \mathbf{k_2^+} &= k_x^2 + k_{2z}^2 = \omega^2 \mu_0 \varepsilon_0 \varepsilon_2. \end{aligned} \tag{1.15}$$

The complex modal propagation constant is then found by combining the above equations

$$k_x = k_0 \sqrt{\frac{\varepsilon_1 \varepsilon_2}{\varepsilon_1 + \varepsilon_2}}, \tag{1.16}$$

where $k_x = k_x' + ik_x''$ is the k-vector component in the direction of propagation. For a solution to exist, one medium needs to be dielectric with a positive ε_1' while the other one needs to have a metallic permittivity with a negative ε_1'. The pairing of negative permittivity metals and dielectric allows for a field that looks mirrored[b] at the boundary,

[b] The fields are not usually strictly mirrored. However, the handedness of electric and magnetic fields

creating what is called a surface plasmon polariton (SPP). The polarization originating from the free-carriers in the metal is delayed by almost half a cycle as illustrated in Figure 1.1. This effectively inverts the electrical field and allows the evanescent fields decaying on both sides of the interface to be matched. An exemplary field distribution of a surface plasmon polariton is also shown in Figure 1.2.

The propagation constant of modes will hereinafter always be normalized to the propagation constant of plane waves in the cladding

$$k_p = \frac{k_x}{k_0\sqrt{\varepsilon_2}}. \tag{1.17}$$

This allows evanescent solutions ($k_p' > 1$) to be easily identified and differentiated from unbound ones ($k_p' < 1$).

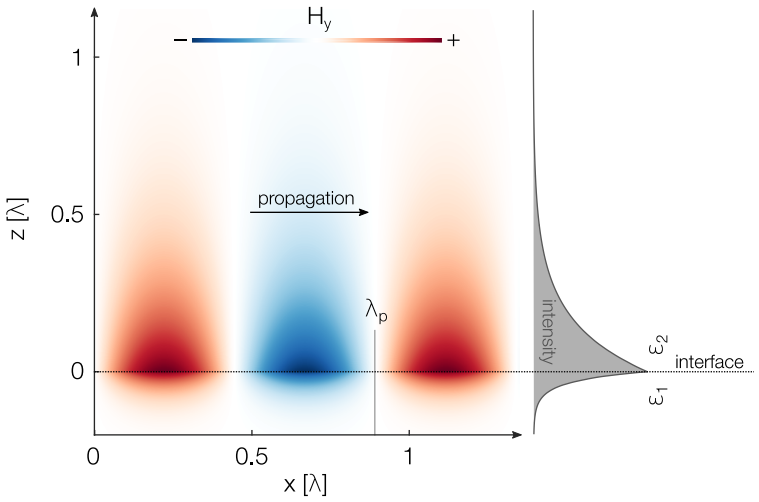

Figure 1.2: An example of a surface wave with propagating along the interface of a metallic ($\varepsilon_1 = -5$) and a dielectric ($\varepsilon_2 = 1$) medium. The surface wave is bound to the interface and evanescently decaying. Its wavelength λ_p is slightly shorter than the free-space wavelength λ due to the increased momentum required for the evanescent profile.

with respect to the k-vector is opposed on both sides of the interface.

1.2 Zenneck waves and other surface waves

The surface plasmon polariton is not the only surface wave that exists for a single interface boundary. If one softens the initial conditions that were demanding homogeneous and isotropic materials, other solutions can also be found. At the boundary between uniaxial anisotropic materials and a isotropic dielectric, Dyakonov waves[24] exist if the necessary symmetry conditions are fulfilled. If one allows nonhomogeneous permittivity at the interface, Tamm waves[25] are possible. Metamaterials and Metasurfaces with artificially designed permittivity can also be used to support single interface surface waves. A thorough review of single interface surface waves other than the surface plasmon polariton can be found in [26] and [27].

Apart from those, Zenneck waves exist at the interface between a lossy and a loss-free dielectric.[28–30] The Zenneck wave is certainly the most unorthodox of all surface waves. It is not only the oldest of all mentioned surface waves, but also the one that has created the greatest controversy.[31–34] Even the name of the Zenneck wave itself has been debated. While Zenneck's 1907 publication made the wave famous, it had been discovered earlier by K. Uller, of one of Zenneck's PhD students. Uller had already described the wave in his dissertation[28] four years before Zenneck published the results himself.

It was originally believed that the Zenneck wave was the driving force behind Marconi's first transatlantic radio communication. The transmission beyond the horizon was attributed to *ground wave propagation* – another name for surface waves between lossless air and lossy ground or water. It was later found to be the reflecting ionosphere and not the Zenneck wave that was carrying the radio frequencies over the ocean. Since then, the existence of the Zenneck wave has been questioned many times.[31,32,35,36] In particular, a sign error[37] was believed to be in Sommerfeld's mathematical description[30] of the wave. Only recently – almost a hundred years later – the controversy seems to have been mathematically resolved.[38]

The reason for highlighting Zenneck waves at this point is, that Zenneck waves obey the same dispersion relation as the surface plasmon polariton (Equation 1.16). Unlike the surface plasmon polariton, the Zenneck wave has no requirement for a negative permittivity. It is therefore of interest to differentiate both surface waves and to understand which of the previous conditions disallowed Zenneck waves in the previous derivation.

The most decisive difference between both modes is their phase speed. The surface plasmon polariton is a *slow wave* with a real part of the propagation constant larger than that of plane waves in the cladding ($k_x' > \sqrt{\varepsilon_2}k_0$ i.e. $k_\mathrm{p}' > 1$). It is situated on the evanescent side of the *light-line* ($\omega = c_0 k_0 \sqrt{\varepsilon_2}$), which separates the evanescently bound solutions, from the freely propagating solutions in the cladding. The Zenneck wave, being a *fast wave*, has a smaller propagation constant ($k_x' < \sqrt{\varepsilon_2}k_0$ i.e. $k_\mathrm{p}' < 1$), which has serious implications for the Zenneck wave. The Zenneck wave is not a guided mode in the sense that it is able to propagate by itself but requires an incident external field in order to exist. This case was implicitly excluded at the beginning, allowing only waves with k-vectors pointing away from the interface (see Figure 1.1). The k-vector on the dielectric side of a Zenneck wave always points toward the interface under the Brewster angle. The evanescent shape of the mode is only maintained as long as the external field is present. The wave is unable to exist and propagate on its own. The relevance for waveguiding applications is thereby quite limited. In addition, typical propagation lengths are much shorter than those of surface plasmon polaritons.

1.3 Thin-film waveguiding

The three layer case is the next level of complexity that can still be handled semi-analytically without much clutter. Similar to the single interface case, the modes can be calculated by making a suitable ansatz followed by enforcing the boundary conditions. The two parallel interfaces are arranged symmetrically about the (x, y)-plane, separated by a middle layer of thickness d. We assume the following permittivity profile representing a slab of thickness d together with a substrate and superstrate

$$\varepsilon(z) = \begin{cases} \varepsilon_2 & \text{if} \quad z < -\frac{d}{2} \\ \varepsilon_1 & \text{if} \quad -\frac{d}{2} < z < \frac{d}{2} \\ \varepsilon_3 & \text{if} \quad z > \frac{d}{2}. \end{cases} \tag{1.18}$$

The E and H-fields used for the ansatz are similar to those of the single interface case except the fields inside the slab where upward and downward propagation is allowed:

$$H_y^{(2-)}(x,z) = A^{(2-)} \mathrm{e}^{i\mathbf{k}_2^- \cdot \mathbf{r}} \qquad E_x^{(2-)}(x,z) = A^{(2-)} \frac{k_{2z}}{\omega \varepsilon_0 \varepsilon_2} \mathrm{e}^{i\mathbf{k}_2^- \cdot \mathbf{r}}$$

$$
\begin{aligned}
H_y^{(1+)}(x,z) &= A^{(1+)} \mathrm{e}^{i\mathbf{k}_1^+ \cdot \mathbf{r}} & E_x^{(1+)}(x,z) &= A^{(1+)} \frac{-k_{1z}}{\omega \varepsilon_0 \varepsilon_2} \mathrm{e}^{i\mathbf{k}_1^+ \cdot \mathbf{r}} \\
H_y^{(1-)}(x,z) &= A^{(1-)} \mathrm{e}^{i\mathbf{k}_1^- \cdot \mathbf{r}} & E_x^{(1-)}(x,z) &= A^{(1-)} \frac{k_{1z}}{\omega \varepsilon_0 \varepsilon_1} \mathrm{e}^{i\mathbf{k}_1^- \cdot \mathbf{r}} \\
H_y^{(3+)}(x,z) &= A^{(3+)} \mathrm{e}^{i\mathbf{k}_3^+ \cdot \mathbf{r}} & E_x^{(3+)}(x,z) &= A^{(3+)} \frac{-k_{3z}}{\omega \varepsilon_0 \varepsilon_3} \mathrm{e}^{i\mathbf{k}_3^+ \cdot \mathbf{r}}.
\end{aligned} \tag{1.19}
$$

Enforcing the boundary conditions at both interfaces leads to an equation system which can be written in matrix form as

$$
\mathbf{M} \cdot \mathbf{A} = 0 \tag{1.20}
$$

with

$$
\mathbf{M} = \begin{pmatrix}
\mathrm{e}^{ik_{2z}\frac{d}{2}} & -\mathrm{e}^{-ik_{1z}\frac{d}{2}} & -\mathrm{e}^{ik_{1z}\frac{d}{2}} & 0 \\
\frac{k_{2z}}{\varepsilon_1}\mathrm{e}^{ik_{2z}\frac{d}{2}} & \frac{k_{1z}}{\varepsilon_2}\mathrm{e}^{-ik_{1z}\frac{d}{2}} & -\frac{k_{1z}}{\varepsilon_2}\mathrm{e}^{ik_{1z}\frac{d}{2}} & 0 \\
0 & \mathrm{e}^{-ik_{1z}\frac{d}{2}} & \mathrm{e}^{ik_{1z}\frac{d}{2}} & -\mathrm{e}^{-ik_{3z}\frac{d}{2}} \\
0 & -\frac{k_{1z}}{\varepsilon_2}\mathrm{e}^{-ik_{1z}\frac{d}{2}} & \frac{k_{1z}}{\varepsilon_2}\mathrm{e}^{ik_{1z}\frac{d}{2}} & \frac{k_{3z}}{\varepsilon_3}\mathrm{e}^{-ik_{3z}\frac{d}{2}}
\end{pmatrix}, \quad \mathbf{A} = \begin{pmatrix} A^{(2-)} \\ A^{(1+)} \\ A^{(1-)} \\ A^{(3+)} \end{pmatrix}. \tag{1.21}
$$

Here, the odd and even rows of $\mathbf{M}$ reflect the boundary conditions at $z \pm {}^{d}/_{2}$ for the H and E field, respectively. For this homogeneous equation system to have a modal solution the determinant is required to be vanishing. Thereby, the equation system allows non-zero field amplitudes without external excitation. In a lengthy calculation the equation system can be brought into an upper triangular form to simplify the calculation of the determinant. By enforcing $\det|\mathbf{M}| = 0$, an implicit equation is found:

$$
\mathrm{e}^{-i2k_{1z}d} = \frac{\frac{k_{1z}}{\varepsilon_1} + \frac{k_{2z}}{\varepsilon_2}}{\frac{k_{1z}}{\varepsilon_1} - \frac{k_{2z}}{\varepsilon_2}} \frac{\frac{k_{1z}}{\varepsilon_1} + \frac{k_{3z}}{\varepsilon_3}}{\frac{k_{1z}}{\varepsilon_1} - \frac{k_{3z}}{\varepsilon_3}}. \tag{1.22}
$$

For slabs with a thickness much larger than the absorption length ($k_{1z}'' d \gg 1$) the left hand side is vanishing. This leaves a separable right hand side, having zeros for $\frac{k_{1z}}{\varepsilon_1} = -\frac{k_{2z}}{\varepsilon_2}$ and $\frac{k_{1z}}{\varepsilon_1} = -\frac{k_{3z}}{\varepsilon_3}$. These two dispersion relations represent uncoupled single interface surface waves at either side of the thick slab.

For thinner slab thicknesses, the mode profiles of the two surface waves overlap and can no longer be treated individually. The coupling between both parts needs to be taken into account. Two distinct modal solutions are known if the outer cladding layers are assumed to have equal permittivity. It will be evident later that this restriction is not

a critical limitation. With $\varepsilon_2 = \varepsilon_3$, Equation 1.22 can be reduced and separated into two branches[13,39]

$$\tanh\left(\frac{k_{1z}d}{2}\right) = -\left(\frac{\varepsilon_1 k_{2z}}{\varepsilon_2 k_{1z}}\right) \tag{1.23}$$

and

$$\tanh\left(\frac{k_{1z}d}{2}\right) = -\left(\frac{\varepsilon_2 k_{1z}}{\varepsilon_1 k_{2z}}\right). \tag{1.24}$$

The upper one is referred to as the symmetric branch or *long-range* mode. It possesses a longer propagation length with slightly reduced confinement compared to the corresponding single interface wave. The lower one is referred to as the antisymmetric branch or *short-range* mode. It is quite opposite and has a strong confinement together with a very short propagation length. The discrepancy of both modes is most evident for vanishing core thickness. Here, the long-range propagation constant converges against a cladding plane wave while the short-range propagation constant diverges. In both cases a smooth transition is found from the case of separated single interface surface plasmons with a large core thickness toward the thin-film regime.

In Figure 1.3, exemplary field distributions for the long and short-range mode are presented. The H_y component is shown as it is continuous at both interfaces. The E_x and E_z components of the field possess different symmetries. The in-plane component E_x shares the same parity as H_y i.e. even parity for the long-range branch and odd parity for the short-range branch. The out-of-plane component E_z has the corresponding opposing parity. The antisymmetric mode has a characteristic zero crossing as the fields on either side are out of phase, leading to cancellation along the mirror plane.

That which differentiates both modes, besides their confinement and propagation length, is the range of core permittivities for which solutions exist. The convergence of two single interface surface plasmon polaritons forming a hybrid mode is *one* solution of the symmetric slab. It is, however, not the *only one*. The remarkable and largely unknown feature of the long-range branch is, that solutions exist even for non-metallic and absorbing media. This includes media, that lack a single interface solution such as the surface plasmon polariton. For a symmetric cladding thin-film waveguide (SCTW), the boundary conditions at both interfaces need to be matched simultaneously. Figure 1.4 illustrates the different concepts that allow matching in metallic and non-metallic media. The matching for metallic media with negative ε' and small ε'' is very similar

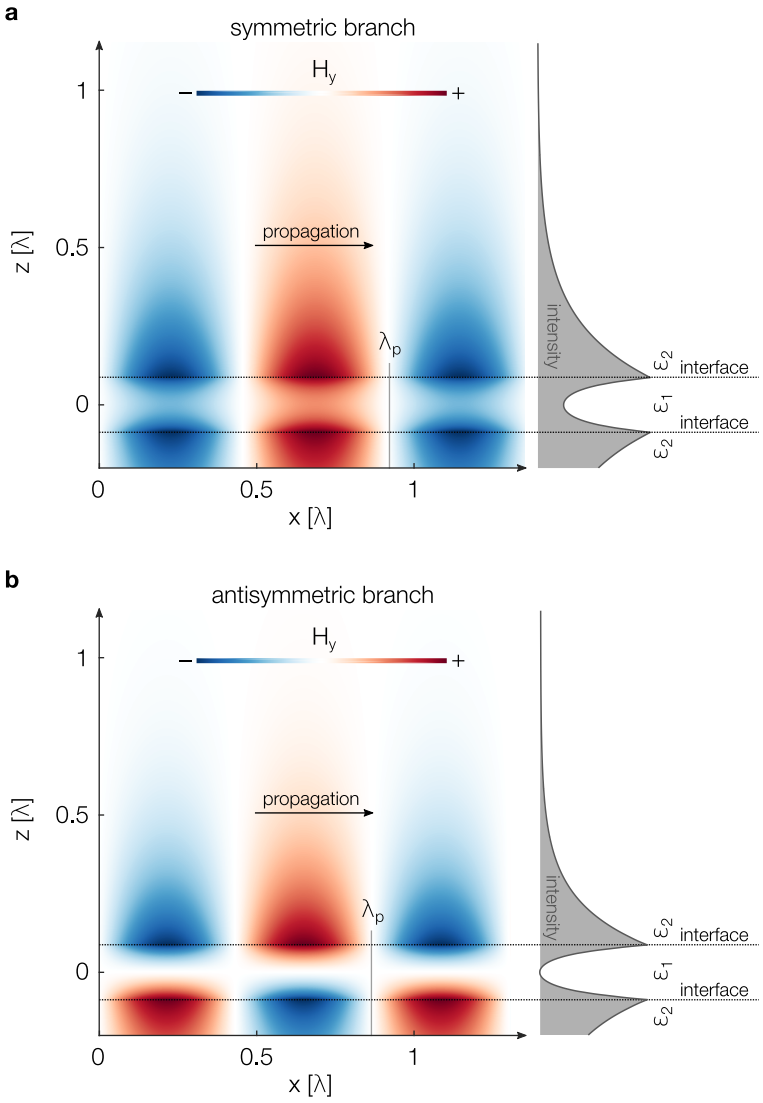

Figure 1.3: Field patterns for the two solution branches of a metallic thin-film waveguide with symmetric lossless cladding ($\varepsilon_1 = -5$, $\varepsilon_2 = 1$). According to their field symmetry, solutions are referred to as (a) symmetric and (b) antisymmetric mode. The former, known as the *long-range* branch mode, possesses a weaker confinement together with an increased propagation length. The latter, known as the *short-range* branch, possesses a stronger confinement and a reduced propagation length.

to the single interface case with an inverted E-field in the metal. The upward and downward propagating waves in the core have a strong lateral imaginary k-vector that localizes the wave to either of the two interfaces. For non-metallic media or highly lossy

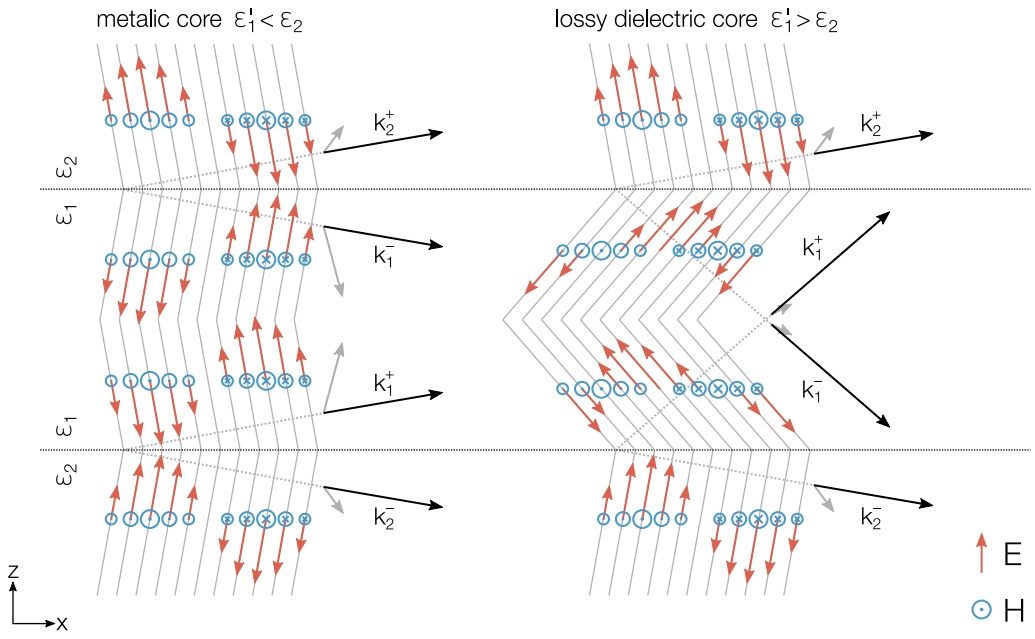

Figure 1.4: The boundary conditions of the symmetric cladding thin-film waveguide can be met for both metallic and dielectric core materials. In the case of a metal, an upward and a downward propagating wave, e.g. $\mathbf{k}_2^+$ and $\mathbf{k}_1^-$, are matched through the field inversion in the metal – in analogy to the single interface surface plasmon polariton. In the lossy dielectric case, the E-fields in the core are not inverted and surface-plasmon-polariton-like pairs cannot be formed. However, the boundary conditions can be met through pairing the respective upward and the downward propagating waves that form a Zenneck-wave-like pair on either interface. Although the matching is similar to Zenneck waves, the overall modes is a bound slow wave with a phase speed slower than light in the cladding.

media with large ε'' the boundary conditions are met in a different way. The two waves in the core have only a modest lateral confinement to the interfaces. Thereby not only an upward and a downward propagating wave can form a matching pair, but also waves of the same type i.e. respective pairs of upward or downward propagating waves. Thus, an inverted E-field, as in the single interface case, is no longer necessary.

Besides the core permittivity, the core thickness plays an important role in thin-film waveguiding. Figure 1.5 shows the complex propagation constant as a function of the thickness for three different permittivities. Three exemplary permittivity values are

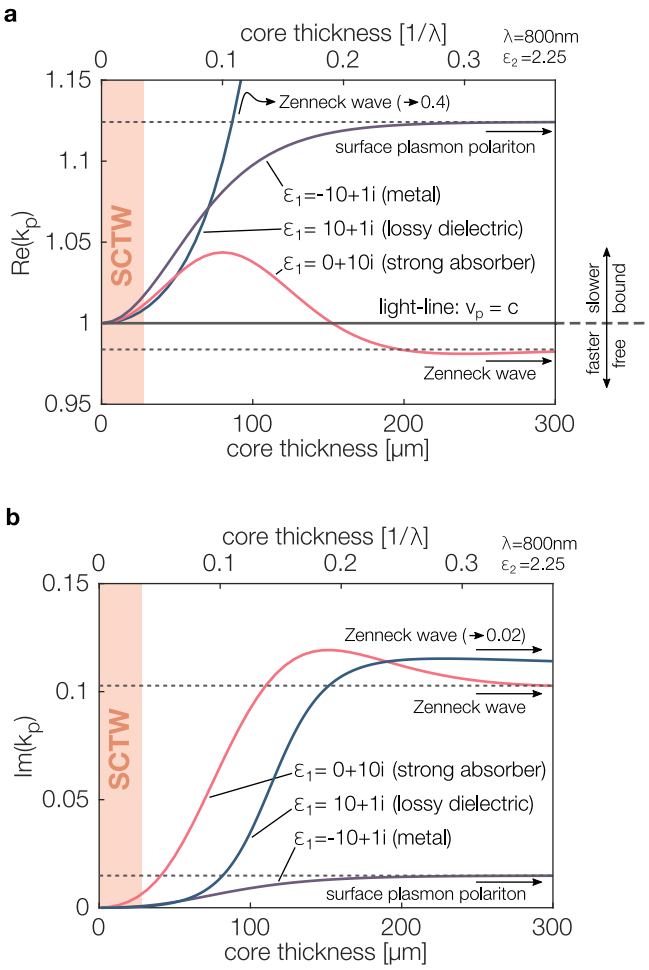

Figure 1.5: Solutions of TM polarized slab waveguide modes with symmetric cladding. (a) Real part of the normalized propagation constant k_p indicating the lateral confinement and the phase speed. (b) Imaginary part of k_p representing the propagation losses. On decreasing the waveguide thickness, the single interface solutions on either side couple, forming a hybrid symmetric cladding thin-film waveguide (SCTW) mode. At the price of reduced confinement, propagation losses are significantly reduced. For metallic media, the single interface surface wave is the surface plasmon polariton while for lossy dielectrics it is the Zenneck wave. The decisive point here is that for very thin but highly lossy dielectrics, the real part of the propagation constant is lifted above the light-line. The two coupled Zenneck waves become an evanescently guided mode that can propagate on its own without any incident wave from the cladding. The Zenneck wave solutions for the lossy dielectric core lies far outside the shown range with $k_p = 0.4 + 0.02i$.

show, representing a metal, a strong absorber[c], and a lossy dielectric. SCTW modes lie to the upper side of the *light-line* that separates evanescently bound solutions (*slow waves*, $k'_x > \sqrt{\varepsilon_2}k_0$ i.e. $k'_\mathrm{p} > 1$) from freely propagating solutions in the cladding (*fast waves*, $k'_x < \sqrt{\varepsilon_2}k_0$ i.e. $k'_\mathrm{p} < 1$). The formation of the hybrid SCTW mode can be seen for all three permittivities. For the strong absorber, the transition from the unbound Zenneck wave to the bound SCTW mode is visible. The real part of the propagation initially lies below the light-line. Upon thinning the core, it crosses the light-line coming from the lower side, followed by converging against it from the upper side. This transition is also present for the lossy dielectric, but occurs far outside the shown thickness range. The phase velocity of the modes increases, but never exceeds the speed of light in the cladding. At the same time, overall propagation losses of the modes are significantly reduced. The confinement of SCTW modes has fully vanished when approaching a thickness $d = 0$. At this point, the mode has converged against a loss-free plane wave in the cladding. SCTW modes are generally located very close to the light-line. The symmetry of the cladding permittivity – demanded earlier – is therefore not a restriction to the solution space but rather an indispensable requirement for propagation. Any significant asymmetry of the cladding permittivity would immediately open a radiative loss channel. On the higher index side the mode would no longer be bound, leading to light being radiated into the far-field.

SCTW solutions can be found in the whole permittivity plane except for a small region around the cladding permittivity. This cutoff is defined by[14]

$$|2\varepsilon_1 - \varepsilon_2| \overset{!}{>} |\varepsilon_2|\,, \tag{1.25}$$

which describes a circle of diameter ε_2, centered at $\frac{1}{2}\varepsilon_2$ (see Figure 1.6). For loss-free materials, Equation 1.25 is equivalent to the condition for total internal reflection ($n_1 > n_2$). If a material has sufficient permittivity contrast to the cladding, propagation is even allowed along highly absorbing materials. This includes materials with exceptionally strong absorption that would – as a bulk material – absorb light in a fraction of the light's free-space wavelength. One can think of the whole concept as the wave being trapped by the core and having no other option than to propagate along the slab. The

[c] The term 'strong absorbers' is used thereinafter for materials that have a predominantly imaginary permittivity. A Lorentzian resonance describes a circle in the permittivity plane that is placed on top of the background permittivity ε_∞. The center of a single resonance therefore lies close to imaginary axis.

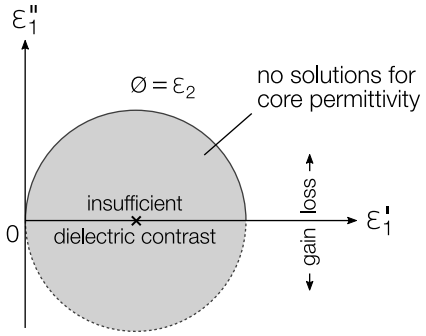

Figure 1.6: The only region that a core material is unable to support an SCTW mode is set by the cladding permittivity. Waveguiding is forbidden within a circle that has a diameter of the cladding permittivity. This is valid for both loss and gain material. The shown cutoff reduces to the total internal reflectance condition $n_1 > n_2$ if both materials are loss-free ($\varepsilon_1'' = \varepsilon_2'' = 0$)

momentum of the wave is too large to radiate into the cladding. At the same time, the thin core has too little volume to quickly absorb the wave. Unless momentum is subtracted by other means such as scattering, the wave keeps propagating with its evanescent profile until it is fully absorbed by the core material.

Chapter 2

Symmetric cladding thin-film waveguides

Material responses are at the same time a blessing and a curse for the guided propagation of light. There is no dispersion without absorption. The permittivity contrast that is required for the guidance of the wave always comes at the price of absorption. In particular, strong material responses are likely to come bundled with equally increased absorption features. Even materials with epsilon near zero, so called ENZ materials, are never loss-free. Due to the inherent relation of the permittivity and material losses, it is of interest to consider both together in the context of thin-film waveguiding.

Waveguiding in lossy material has been known for quite some time, dating back to initial publications by Kovacs [11] and Yang et al. [12]. Yet, the bigger picture on the influence of permittivity has been missing in literature. There have been, without doubt, quite a few noteworthy publications[a] that have discussed the concept of highly lossy waveguiding materials.[11–13,15,16,41–43] However, the majority of these works focused solely on materials with permittivity on or very close to the imaginary axis ($\varepsilon_1'' \gg \varepsilon_1'$). Given the similarities and dissimilarities with long-range modes in metallic media, a deeper understanding of the influence of material losses is desired to put SCTWs in a broader context.

[a] A well researched overview of waveguiding with lossy materials can be found in the review article by Berini [40]. Although the article focuses on long-range surface plasmon polaritons, it contains a subsection on lossy materials with a thorough literature list.

2.1 Permittivity contrast and propagation losses

This section aims to identify how the bulk material loss of a particular material transfers into propagation losses of modes in a thin-film. It should be borne in mind that material losses – as encoded in complex permittivity – describe the absorption of a plane wave in a bulk medium. It neither tells us how the light got in there, nor what losses are to be expected with other waves in different geometries. The bulk material absorption does not directly translate into propagation losses of a mode. One might intuitively think that a stronger absorption would always result in a decrease of the modal propagation length. However, quite the opposite is the case for thin-film waveguides. The core thickness plays an important role in thin-film waveguiding. The absorption of light is a function of the absorption strength, the volume of the lossy medium, and the individual field distribution. In an SCTW, the losses also provide permittivity contrast, which is responsible for the evanescent guidance that allowed the modal propagation in the first place. Guiding through permittivity contrast is an effect that is more related to an interface *area*, than it is to a *volume*. The waveguide thickness can be thought of as a tuning parameter, balancing volume and interface effects of the permittivity.

The answer to how material loss affects the propagation in an SCTW is far from being trivial. The solution to the long-range mode branch has many degrees of freedom. Any solution is always a compromise between confinement, propagation loss, and waveguide thickness. There is no single *best material* in this context. To explore the solution space, isolines of equal propagation properties have been calculated over the permittivity plane. Searching for isolines is equivalent to asking which permittivity can be substituted by another while retaining the propagation length and confinement. For a complex propagation vector k_p being a solution of the long-range branch, two additional degrees of freedom exist if the cladding permittivity is kept constant. The two parameters are the complex permittivity ε_1 and the core thickness d. Under variation of d, two materials with different permittivities can propagate in the same manner i.e. with equal k_p. Figure 2.1 illustrates these isolines for different propagation vectors. In the two subfigures, the (a) real and (b) imaginary part of the k-vector is varied[b]. The isolines form an opening

[b] The normalized propagation constants were varied around $k_\mathrm{p} = 1.044 + 0.001i$. At this point, the isolines in the upper region of the plane split into two parts. The choice of the point is otherwise arbitrary, albeit propagation length and confinement are within in the range of typical experimental realizations.

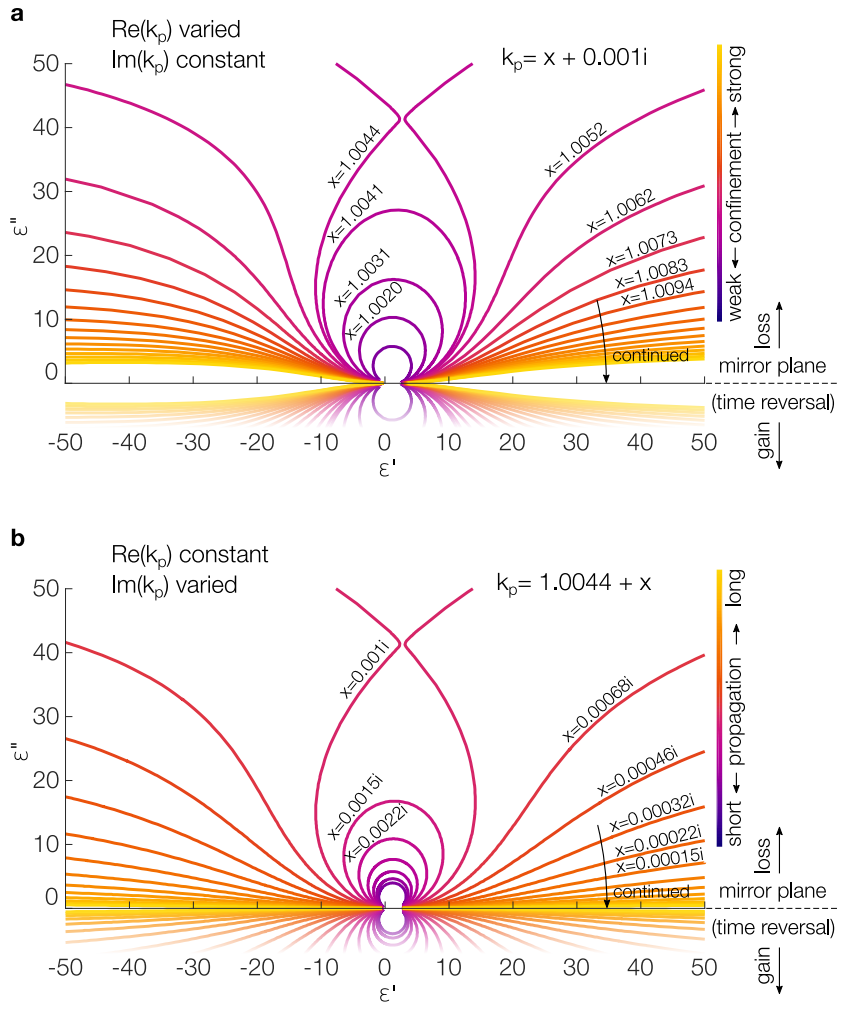

Figure 2.1: Isolines of equal propagation vectors over the core material permittivity. Variations of the (a) real and (b) imaginary part of the normalized propagation vector k_p around $1.044 + 0.001i$, respectively. In the symmetric cladding thin-film waveguide, bound modes exist for almost any permittivity $\varepsilon_1 = \varepsilon_1' + i\varepsilon_1''$. A continuous transition is found between modes supported by dielectric and metallic media. It can be seen that best confinement (large k_p') and longest propagation length (small k_p'') is found for materials with small ε_1'' and large absolute ε_1'. Along each isoline the field in the cladding ($\varepsilon_2 = 2.279$ i.e. BK7 glass at 860 nm) is indistinguishable. The core thickness along the isolines was continuously varied in the range $1\,\text{nm} < d < 500\,\text{nm}$. The propagation properties are mirrored along the real axis. Due to time reversal symmetry, any solution with absorbing core material has a counterpart in the lower half of the permittivity plane which shows gain instead of loss.

blossom centered close to the origin. The outer leaves belong to propagation vectors that either have a longer propagation length or a higher confinement. Isolines are found throughout the whole permittivity plane, spanning from negative permittivity metals over strong absorbers to lossy dielectrics. Materials with a strong material response, i.e. large $|\varepsilon|$, have a tendency for higher confinement. In addition, low ε'' brings both better confinement and propagation length. The lower half-space of the permittivity plane belongs to materials that have gain rather than loss. The solution space is mirrored along the real axis as a consequence of time reversal symmetry of the solution. Every lossy modal solution has a counterpart that is propagating backwards in time with gain. Ideal propagation i.e. modes that are free of loss or gain are only found for materials that lie precisely on the real axis. Any permittivity with $\varepsilon_1'' \neq 0$ leads to a complex propagation vector k_p resulting in loss or gain.

It can be seen in Figure 2.1 that the use of highly lossy materials does not, per se, exclude modal propagation. Despite strong material resonances and a permittivity near the imaginary axis, these materials can have low propagation loss. For plane waves in such a material, the propagation length scales inversely with $\sqrt{\varepsilon''}$ due to increasing absorption. The scaling for symmetric cladding thin-film waveguides is quite the opposite. Here, a stronger material response is in most cases beneficial to the propagation. *Beneficial* in this context means either a stronger confinement or a longer propagation length. Figure 2.2 illustrates how the propagation properties of a mode change under increasing absorption. The modal propagation constant is shown as a function of the film thickness for five permittivity values along the imaginary axis. The two axes show the real and imaginary part of the complex propagation constant. Modes with strong confinement lie on the right side. Modes with low loss are located near the real axis. As the thickness is reduced, the propagation constant moves along a spiral shaped path toward a cladding plane wave ($k_\mathrm{p} = 1 + 0i$) on the light-line. All curves intersect the light-line between 200 nm and 100 nm. By crossing the light-line, the modes become bound. Increased absorption significantly reduces the propagation losses, even if the thickness is kept constant. The confinement of the mode initially increases up to a thickness of around 70 nm. From there on, both confinement and propagation loss decrease. The magnitude of the core permittivity has significant influence on the propagation length. The five curves represent values of ε between 10 and 50. In particular, very thick and very thin

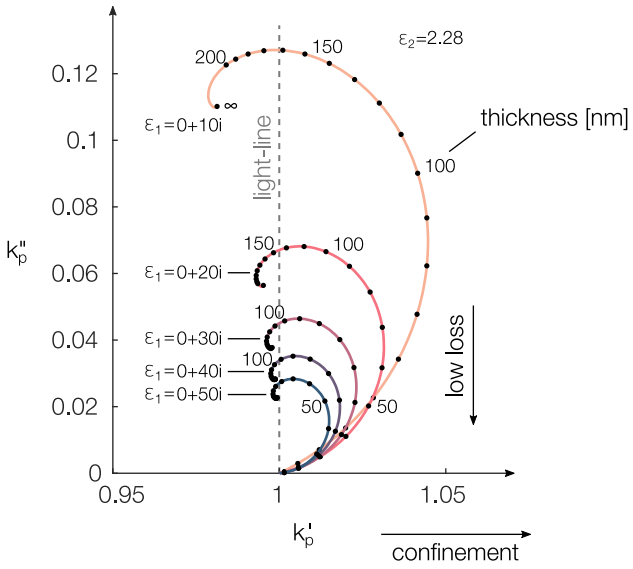

Figure 2.2: Influence of the core material loss ε'' on the normalized propagation constant k_p of an SCTW mode as a function of the thickness. Numbers along the curve denote the waveguide thickness d in nm. A low absorption allows for high confinement, yet only short propagation length. Counterintuitively, a strong absorption improves the propagation length for thin and thick slab waveguides.

waveguides can profit from the increased contrast. A film thickness of approximately 50 nm leads to very similar propagation length for all cases. Above and below, however, waveguides with higher index contrast show significantly better loss figures. Depending on the core's permittivity, the propagation loss k_p'' falls below 10^{-3} between 10 nm and 20 nm. For comparison, an Au based single interface surface plasmon polariton in the near infrared (780 nm) has a normalized propagation vector of $k_p \approx 1.06 + 0.004i$[c]

2.2 Mode transformation

The isolines of equal propagation length shown in Figure 2.1 raise the question whether modes in dielectrics or metals possess distinct properties that can be used to qualitatively differentiate them. The modal solutions for a given k_p were calculated only through the variation of the thickness d. Along the isolines, the variation of d is smooth and

[c]when paired with a typical glass such as BK7 as assumed in the calculations for Figure 2.2. A pairing with air would result in a normalized propagation constant of $k_p \approx 1.02 + 0.002i$

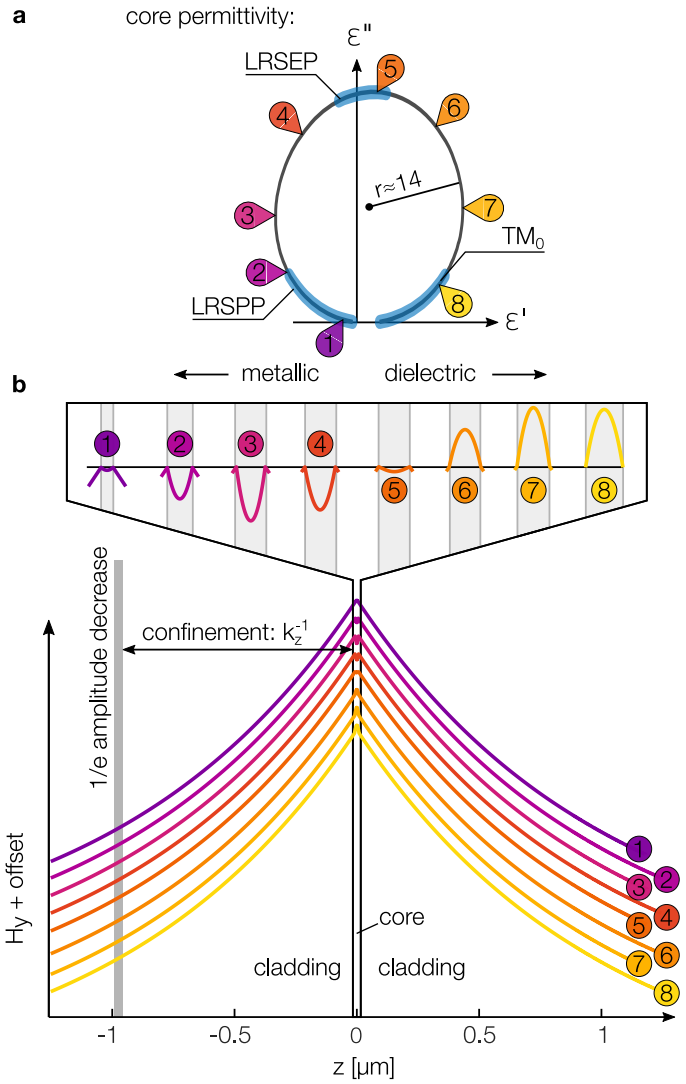

Figure 2.3: H-fields for a set of different symmetric cladding thin-film waveguides propagating in x-direction. Throughout the series of profiles 1 to 8, the core permittivity ε_1 was varied while the cladding was left unchanged ($\varepsilon_2 = 2.28$). Propagation length and confinement are the same ($k_p = 1.0041 + 0.001$) for all modes (1-8) as the core permittivities ε_1 were chosen to lie on a near circular isoline with radius $r \approx 14$ (see Figure 2.1). The field in the cladding is identical and differences are only found in the core. The mode profile in the core varies from an exponential shape with a predominantly imaginary k_z component (i.e. curve 1) to a cosine shape with predominantly real k_z component (i.e. curve 8). A continuous transformation is found between modes referred to as long-range surface plasmon polariton (LRSPP), long-range surface exciton polariton (LRSEP), and transverse magnetic waveguide modes (TM). The thickness of the core was varied from 7 nm for profile 1 to 40 nm for profile 8. Due to the equal propagation vector, these modes are indistinguishable if they are probed by techniques such as attenuated total reflection (ATR) spectroscopy.

continuous[d], indicating a seamless transformation of the mode. However, literature classifies modes in different permittivity regions under distinct names. The long-range modes in the metallic region close to the real axis are known as long-range surface plasmon polaritons (LRSPP).[40] On the other side, dielectric modes on or very close to the real axis are known as transverse magnetic (TM) waveguide modes.[44] In particular, the lowest order mode TM_0 with the smallest core thickness is of relevance here. Modes in materials with a core permittivity along the imaginary axis, such as those shown in the previous section, are known as long-range surface exciton polaritons (LRSEP). The name LRSEP originates from early publications by Yang et al. [12, 13]. The terminology can be seen as misleading, as excitons are neither the only cause of strong absorption nor are they required for the waveguiding.

Figure 2.3 shows several long-range modes with finite propagation length. The permittivities ε_1 have deliberately been chosen along an isoline covering both metallic and dielectric regions. The figure illustrates the similarities of symmetric cladding thin-film waveguides with metals, strong absorbers, and dielectrics. The H- and E-field in the cladding are identical as they are fully determined by k_p. Differences in the mode profile are only found in the subwavelength sized core. The mode shape inside the core is best characterized through the normal k-vector component of the field:

$$k_z = \sqrt{k_\mathrm{p}^2 - \varepsilon_1 k_0^2}. \tag{2.1}$$

The field inside the core of a waveguide with losses is by necessity a superposition of two exponential and cosine contributions. If the core permittivity is predominantly real ($\varepsilon' \gg \varepsilon''$), k_z is almost fully real or imaginary for positive and negative ε', respectively. An imaginary k_z describes a double exponential profile i.e. field decaying from both interfaces. The resulting field has a minimum in the center, such as curve 1. The modulation is rather weak, as the core is significantly subwavelength. Along the isoline, the curves following after (curves 2 to 4) still share a double exponential profile. Starting with curve 5, the profile becomes flat resulting from equal exponential and cosine

[d] The thickness d serves as a tuning parameter to navigate along an isoline. Small values of d locate the solution initially on the negative permittivity side (metallic). For increasing d, the solution moves clockwise toward the dielectric side in a circular motion. For stronger confinement or long propagation length, the isoline is split in the middle. The solution leaves on the left side and immediately returns on the right side.

contributions ($k_z' \approx k_z''$ e.g. curve 5). The profiles following after show a clear cosine shape with a pronounced maximum instead of a minimum.

In summary, the mode profile is mostly identical. The only differences are found in the core where the profile is a mixture of real and imaginary k_z components. Metallic waveguides have a stronger imaginary part while dielectric waveguides have a stronger real part. A continuous evolution of the mode profile and the thickness is found along isolines. This blurs the boundaries between LRSPP, LRSEP, and TM_0 modes and questions whether the distinct naming is justified. Any demarcation between LRSPP, LRSEP and TM_0 based on the mode shape or the permittivity has to be arbitrary. Long-range modes are a phenomenon that is not restricted to certain quasiparticles such as plasmons or excitons, but exist whenever there is permittivity contrast between cladding and core.

2.3 Permittivity landscape

After the theoretical exploration of the SCTW solution space, attention is now turned to the experimental side. Looking at the isolines in the permittivity plane shown previously, the immediate question arises as to which of these permittivity values is experimentally within reach. As no immediate answer was available in literature, the range of permittivities given by nature was gathered from published ellipsometry data. The study focused on solid materials in the VIS-NIR regime. Figure 2.4 shows the final result, a plot of the assembled *permittivity landscape*. A detailed list containing all citations can be found in Appendix C.[45–47] The complex permittivity plane can be subdivided into several regions. The lower right contains transparent insulators that lie close to the real axis. This includes all optical glasses that virtually occupy only a single point around $\varepsilon \approx 2$ with a few high refractive index glasses reaching up to 3. The losses of commercial glasses are usually in the order of $\varepsilon'' \approx 10^{-7}$ but increase significantly toward the UV. The loss angle δ, that describes the argument of the complex permittivity $\delta = \arg(\varepsilon)$, is close to 0. Above the transparent insulators one finds typical semiconductor materials such as Si, GaAs, and InP. Starting from the bandgap energy, their ε'' increases. Depending on whether the materials are direct or indirect semiconductors and on the individual doping levels, the increase in absorption

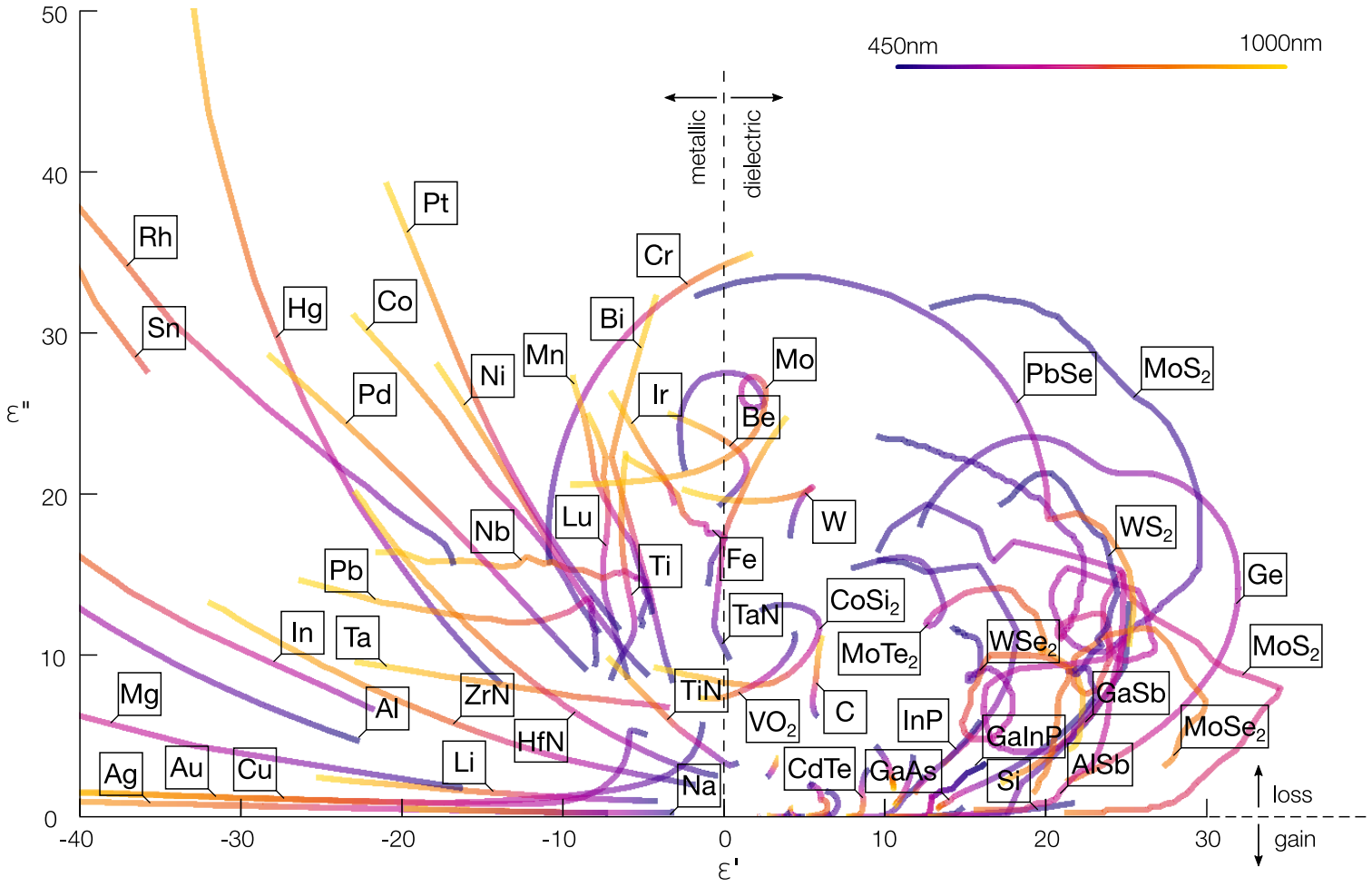

Figure 2.4: The *permittivity landscape* assembled from various ellipsometry data. The plot shows which values of $\varepsilon = \varepsilon' + i\varepsilon''$ are accessible with solid materials in the VIS-NIR regime. The color code ranges from 450 nm to 1000 nm wavelength. Plasmonic materials such as Al, Ag, Au, and Cu are found on the *metallic* permittivity side close to the real axis. Nitrides such as TiN, HfN, and ZrN are next best option for metallic low-loss materials. The majority of all metals have rather large imaginary permittivity that diverges for lower frequencies. At the shorter end of the wavelength range all metals approach the dielectric side. Above the bulk plasmon resonance that usually lies in the UV regime, metals become optically dielectric. On the dielectric side, strong resonances with large permittivity are found for semiconductors. Above their bandgap energy both losses and magnitude can take large values. Transition metal dichalcogenides (TMDs) such as WS_2 WSe_2 MoS_2 $MoSe_2$ together with PbSe and Ge possess the largest values.

with frequency can vary from almost flat to very steep. Semiconductors with very strong resonances such as PbSe, Ge, and transition metal dichalcogenides (TMDs) such as WS_2 WSe_2 MoS_2 $MoSe_2$ have loss angles that can reach up to 90°. The prominent resonance of these materials leads to a high refractive index even far off the resonance. Due to the Kramers-Kronig relations, material resonances lead to counterclockwise turns for increasing energy. The absorbing region around the imaginary axis is also approached from the metallic side of the permittivity planes. Transition metals occupy a large region with loss angles between 90° and almost 180°. The permittivity of these conducting materials is strongly altered by electronic transitions in the VIS and NIR. These broad resonances can completely dominate the permittivity over contributions from the free electrons. Molybdenum, chromium, and tungsten, for example – all metals from their band structure – effectively behave as dielectrics ($\varepsilon' > 0$) in the NIR regime. In addition, metallic media with free electrons possess a bulk plasmon resonance that usually lies in the UV. Beyond this point these materials become transparent and lose their negative permittivity behavior. The classical plasmonic materials Al, Ag, Au, and Cu are found very close to the real axis with a loss angle δ close to 180 degree. Apart from these, nitrides such as TiN, HfN, and ZrN have comparable permittivities, which explains the recent interest in them as alternative materials in the field of plasmonics.

2.4 Figure of merit for thin-film waveguides

Selecting a suitable material out of the permittivity landscape that has optimal performance for a particular application is far from trivial. Besides constraints imposed by processing technology, damage threshold, and chemical compatibility, the individual requirements for confinement and propagation diverge for different applications. There is no single optimal material that fulfills all demands. For example, space constraint integrated optics need a high degree of confinement, whereas applications in nonlinear optics may demand not only confinement but also sufficient propagation length for high field enhancement. Lastly, sensing applications require a long propagation length to reach high sensitivity for refractive index changes. In an SCTW the trade-off between confinement and propagation length is adjustable via the core thickness. Decreasing the film thickness will enhance the propagation at the price of reduced confinement.

Hence, it makes sense to calculate a figure of merit (FOM) that takes both confinement and propagation length into account. Several FOMs have been calculated for similar purposes. While they are mostly similar, they are not the same. An overview regarding the different approaches can be found in [48]. Here, the following variant will be used with the result, expressed in decibel units

$$\mathrm{FOM\,(dB)} = 10\,\log_{10}\frac{k''_{2z}}{k''_{\mathrm{p}}} = 10\,\log_{10}\left(\frac{\mathrm{Im}\left\{\sqrt{k_{\mathrm{p}}^2-\varepsilon_2}\right\}}{k''_{\mathrm{p}}}\right), \tag{2.2}$$

where k_{p} and k_{2z} are the complex components of the k-vector parallel and normal to the interface, respectively. The imaginary part of k_{2z} directly represents the confinement of the mode in the cladding, while the imaginary part of k_{p} is proportional to the propagation losses. The FOM possesses a singularity for lossless modes. It also diverges for vanishing film thicknesses since the losses decrease faster than the confinement. Still, it can serve as a benchmark for optical materials . In Figure 2.5 FOM values are plotted for a wide range of materials that are common in the field of optics. Each box shows the wavelength dependent FOM over the range 450 nm to 1000 nm. The upper and lower curves represent film thicknesses of 5 nm and 30 nm, respectively. The two numbers in each of the boxes denotes the minimum and maximum of the FOM for the respective material.

Among the plasmonic materials, Ag followed by Au and Cu possess the highest FOM values of 46 dB, 44 dB, and 44 dB, respectively. In general, materials with a permittivity close to the real axis show the highest FOM values. However, elementary high refractive index materials with a permittivity anywhere else, have values that lie only 10 to 15 dB below the those of the classical plasmonic materials.

Apart from the elementary materials, compound materials can reach even higher FOMs. Compound semiconductor materials benefit from high permittivity contrast combined with only modest loss below their band-gap energy. A tendency for better propagation properties at the low energy end is clearly visible. This is the result of strong resonances in the UV that also impact the blue end of the VIS spectrum. MoO_3 is the only exception among the selected materials, showing a much higher FOM toward the UV regime while having only a weak FOM in the NIR regime.

The presented FOMs need to betaken with a pinch of salt. Comparing the performance of SCTWs from plasmonic materials with those of highly lossy materials, one may

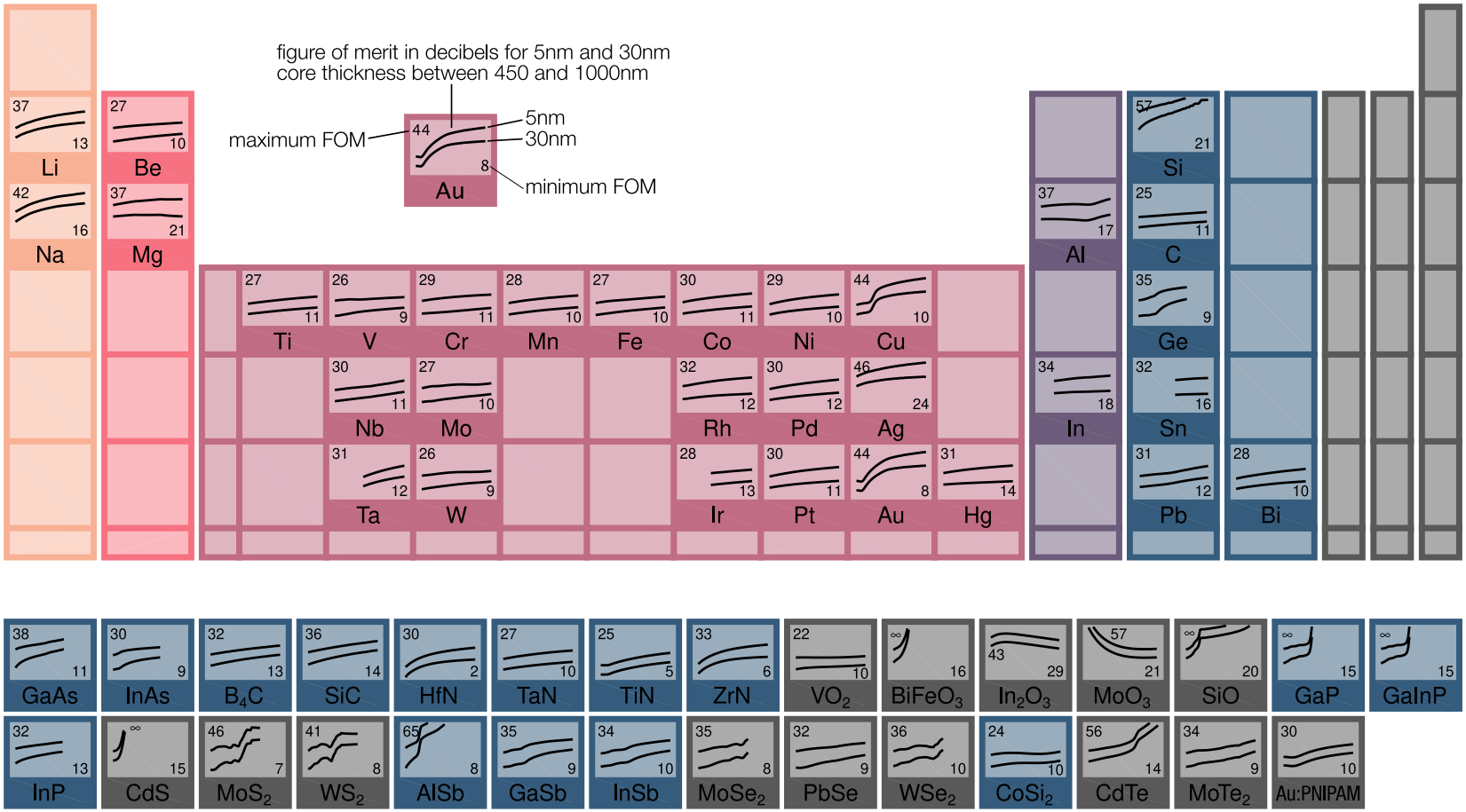

Figure 2.5: Figure of merit (FOM) in decibels for common materials, arranged as in the periodic table. For every material, the FOM is shown for an SCTW with 5 and 30 nm as a function of the excitation wavelength between 450 nm and 1000 nm. All values were calculated assuming an SiO_2 cladding ($\varepsilon = 2.11 + 0i$). The two numbers next to each plot denote the minimum and maximum of the FOM. The lower section contains non-elemental compound materials including, but not limited to, common semiconductor materials.

argue that the latter are unable to surpass the performance of established plasmonic metals. Although certainly true, this would disregard the fact that preparation problems of plasmonic materials can be overcome by using alternative materials. The common noble plasmonic metals – in particular Au – have a tendency to form islandized films if the thickness is very thin. Even with advanced physical vapor deposition (PVD) techniques,[49] high quality thin films of less than 30 nm remain challenging. Transition metals such as chromium or molybdenum, in contrast, allow for the fabrication of films of single digit nanometer thickness with exceptionally low surface roughness. Furthermore, their dispersion is advantageous for guiding at the higher energy end of the VIS/NIR spectrum – with potential extension toward the UV range. Accepting slightly lower confinement or reduced propagation length might be rewarded by other effects. Applications in nonlinear optics, for example, can benefit from SCTWs using materials with strong absorption. Greatly enhanced nonlinear susceptibility is found for excitation close to a resonance which easily outweighs lower field enhancement.[50] Here, using a specific material rather than a plasmonic one a lower FOM may easily be overcome.

2.5 Concluding remarks

SCTWs permit waveguiding with materials that are otherwise unsuitable for modal propagation with low loss. Modes are available to almost any material including plasmonic materials, strong absorbers and lossy dielectrics. Smooth mode transformation was shown between regions commonly known for long-range surface plasmon polaritons, long-range surface exciton polaritons and lowest order TM waveguide modes. SCTW should therefore be seen as a super-category for these modes which are otherwise hard to distinguish. The influence of the permittivity was discussed and isolines of equal propagation properties were shown, that span the whole permittivity plane. The theoretical description was contemplated by the permittivity landscape showing accessible values of permittivity. Additional guidance for practical applications was given through the presentation of figure of merits showing the individual capabilities of elementary and compound materials for the realizations of SCTWs.

It is believed that the findings will be useful in the design of novel photonic devices.

In particular, propagation isolines and mode transformation are important tools for impedance matched – i.e. reflection-free – insertion of lossy waveguide sections into larger assemblies based on plasmonic or near loss-free dielectric waveguides.

Chapter 3

ATR based evanescent coupling

Guided modes possess a k-vector that is larger than those of plane waves in the cladding material. This makes the mode a bound one as the light has too much momentum to radiate into free space i.e. the cladding. At the same time, it does not allow any coupling between the outer world and the bound mode. The mode, so to say, lives undisturbed and on its own.

There are multiple approaches to interacting with guided modes, in particular to feed in far-field radiation by means of a coupler. The most popular ones are grating coupling,[51] end-fire coupling,[52] rough surfaces,[53] edge coupling,[54] and attenuated total reflectance coupling.[55] The individual implementations are quite different but have in common that the momentum of the light is increased such that it can excite the mode. Grating or corrugated interfaces can add or subtract a momentum which corresponds to the periodicity of the surface modulation. Coupling through roughness works in a similar fashion. Although there is no strict periodicity, a rough surface can add momentum which becomes evident by looking at the spatial frequencies it contains. End-fire coupling aims to illuminate one end of a waveguide together with creating large mode overlap between the incident focused light and the mode profile of the waveguide. The step-like refractive index profile allows high spatial frequency components to add to the momentum. Edge coupling illuminates the edge of the structure, often combined with light being fed in by a scanning near-field optical microscope (SNOM) tip. Again, the high spatial frequencies incorporated in the edge profile hold k-vectors large enough

for the excitation.

Attenuated total reflectance coupling uses the evanescent fields with enlarged k-vector to couple the mode with the far-field. By overlapping evanescent near-fields, light can tunnel through barriers that would otherwise reflect it. Near-field coupling is the driving principle for various optical technologies such as fiber optic directional coupling,[56] near-field scanning optical microscopy[57] and total internal reflection fluorescence microscopy.[58] In the case of ATR spectroscopy, the evanescent waves are used to bridge the near fields of the confined modal propagation in the sample with the detection setup in the far-field.

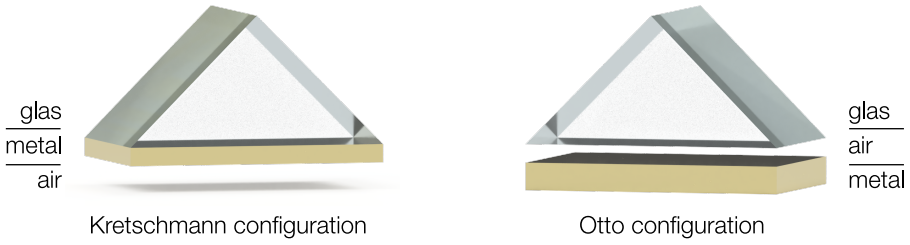

Figure 3.1: Evanescent prism coupling schemes; named after their inventors (left) Kretschmann[59] and (right) Otto.[55] They differ by the order of the stacked layers. The surface plasmon is, in both cases, excited at the air-metal interface. The middle layer, made out of metal, is usually much smaller than its counterpart made of air, due to the shorter optical path length of light in the metal. For plasmons, excited on gold in the VIS and NIR regime, a Kretschmann setup requires a coupling thickness of some tens of nanometers, while an Otto setup needs gaps between hundreds of nanometers and a few micrometers.

Historically, the first optical ATR coupler was the *Otto* configuration,[55] closely followed by the *Kretschmann* configuration.[59] Both configurations were named after their inventors and have been used for the excitation and spectroscopy of surface plasmon polaritons. They are practical realizations of an optical multilayer system consisting of three stacked layers. The implementations differ from each other in the arrangement of their layers. The top layer in both is a glass prism to provide the required photon momentum. In the Otto configuration this layer is followed by an air gap and then metal, whereas in the Kretschmann configuration, the metal sits in the middle, followed by air. In both cases, the surface plasmon is excited at the air-metal interface.

For ATR based coupling, both energy and momentum need to be matched. While the energy is given by the frequency of the light-field, momentum can be tuned accordingly through the angle of incidence θ. For a plane wave illuminating the prism hypotenuse, the k-vector is projected onto the surface. The x-component, which points in the direction of the surface wave propagation, can be tuned as $k_x = k_0\sqrt{\varepsilon}\sin(\theta)$, where θ is the angle between the surface normal and the k-vector of the incident wave. Compared with other available coupling techniques, attenuated total reflectance coupling is unsurpassed when well-defined k-vectors and minimal coupling loss is required. It does not require any resonant structure and can serve as a broad-band coupling device.

3.1 ATR coupling as a k-resolving spectroscopy method

The angular sensitivity of an ATR setup can be used as a spectroscopic method to obtain the k-vector of a mode. From the angular resonance profile, the modal propagation constant can be derived. Unknown parameters of the system can then be calculated, such as the mode's phase velocity, propagation length, layer thickness, permittivity or interface roughness. Similar to ellipsometry, not all unknowns can be found at the same time, as there is a significant amount of ambiguity that has to be considered when fitting the results.[60]

Technical challenges are likely to be the reason why coupling through an air gap, i.e. the Otto configuration, has seen very little adaption since its invention.[55] Most ATR experiments make use of the Kretschman-Raether geometry in which the sample is applied as a sub-wavelength thin-film directly on the prism. Although inherently more robust to mechanical and thermal effects, this geometry is unsuitable for bulk or opaque samples and requires separate samples for each desired coupling strength. The latter may be disadvantageous if the properties of the sample are not known a priori. Moreover, a precisely controlled coupling strength is important for the achievement of *critical coupling*. Critical coupling marks the point of loss-free coupling where intrinsic propagation losses of the mode match the radiative losses introduced by the evanescent coupling. Under critical coupling conditions all energy is coupled into the mode and absorbed by it. Critical coupling is originally known from the theory of coupled resonators where energy is transferred uni-directionally without loss upon

impedance match of the resonators.

3.2 Nanoscale coupling gaps

As the evanescent decay of the light field occurs on the order of the wavelength or even below, nanometer precision control of the gap size is an essential requirement for ATR spectroscopy. While the technical difficulties of evanescent coupling have long been solved for integrated photonics, coupling through wide-area nanometer gaps of air or liquid is still challenging. The nature of separation by a non-rigid gap makes Otto type ATR setups very prone to thermal expansion and vibration, both having severe impact on the stability. Due to the lossy nature of SCTW modes, depositing heat in the system is unavoidable. Upon matched impedance, all optical power is eventually absorbed in the lossy waveguiding core. This is of particular relevance when nonlinear processes that require high input powers are to be excited. Thermal drifts can also occur when the excitation beam is scanned over the angular resonance. Large variations of the heat flux can be found between on- and off-resonant excitation that perturb the thermal equilibrium, leading to undesired thermal expansion. Thus, a real-time feedback of the gap width is required to counter such effects and stabilize the coupling conditions.

Nanometer resolving technologies such as glass scale encoders, capacitive sensors, piezoresistive sensors, or differential transformers are readily available.[61] However, SCTW modes require an unobstructed coupling region which prevents the placement of such sensors directly in the gap. Encoder solutions mounted at an offset position are detrimental as their measurements are very prone to errors due to tilt and deformation which require external compensation.

3.3 White-light interferometry based distance readout

A technique has been developed that reduces the mechanical complexity and allows the gap to be sensed in a direct and non-invasive way, which is highly desirable to harness the full potential of ATR spectroscopy. The method employs spectrally resolved white-light interferometry to resolve the distance between the coupling prism and sample with nanometer resolution. Thereby, the parallelism of prism and sample can

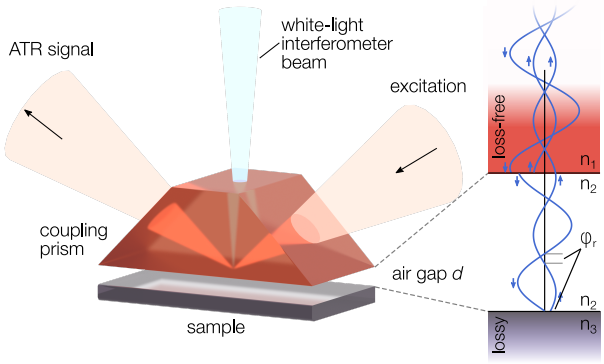

Figure 3.2: Sketch of the ATR geometry with integrated white-light interferometry for high-accuracy absolute coupling gap control. Back reflections from interfaces interfere in the spectrometer and provide a unique spectral modulation.

be brought down to a single arcsecond. The white-light coupled into the system is non-invasive and allows remote in situ monitoring of the coupling distance without perturbing the modal propagation in the sample.[50,62] Read at real-time, the signal can be used as a feedback to stabilize thermal drifts in the setup. The measured signal is a unique function of the gap-size providing an absolute valued distance readout. Initial referencing of an origin is not required as it is with monochromatic interferometers.

The ATR coupler forms an optical multilayer system together with the sample, as illustrated in Figure 3.2. The task at hand is to calculate the spacing between the prism and sample from the spectral modulation pattern of the back-reflected white-light. The gap can be theoretically treated as a Fabry-Pérot resonator formed by the prism-air and the air-sample interfaces. The overall complex reflectance coefficient of the multilayer system can be calculated. The system is then treated as a single interface with the computed reflectance function. In Figure 3.3, spectra taken at different coupling gaps are shown. The actual gap width d can be calculated from the unambiguous signature of the cavity. The condition for constructive interference from the two surfaces is

$$d \cdot n_2 \cdot \cos\theta = \left(m + \frac{\varphi_r}{2\pi}\right) \cdot \frac{\lambda}{2}, \qquad m = 1, 2, 3 \ldots, \tag{3.1}$$

where d is the interface spacing, n_2 the refractive index in the gap, θ the tilt angle of the white-light beam with respect to the sample surface normal, and φ_r the phase retardation due to reflection at the sample surface. Light reflected at the prism surface is in-phase with the incident wave ($n_1 > n_2$ as required by ATR spectroscopy). At the

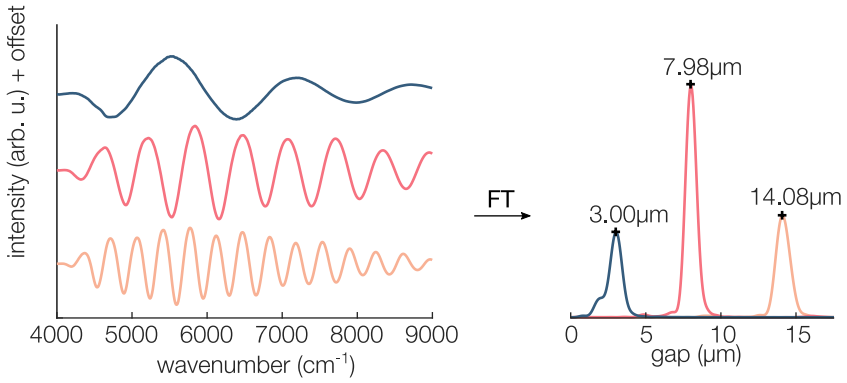

Figure 3.3: Reflectance spectra for an AlN sample close to an ATR coupling prism. The coupling gap size d can be determined by computing the Fourier transform of the reflectance signal.

sample surface, however, the phase retardation depends on the sample permittivity and the layer structure. For normal incidence, it can be anywhere between –180° and 0°. Figures 3.4 and 3.5 show the reflectance phase and the magnitude of a material as a function of its permittivity, respectively. The positive real axis has a stepwise profile with 0° for $\varepsilon' < 1$ and –180° for all media with $\varepsilon' > 1$. This is also known by the rule that light reflected at a higher index media is subject to a π phase jump. However, as soon as lossy materials come into play, this rule is no longer valid and φ_r varies between –180° and 0° over the permittivity plane. Consequently, φ_r has – in general – a non-constant spectral response that needs to be known in order to derive the absolute distance. Previous implementations[63,64] of the Otto-geometry using monochromatic interferometry have disregarded the reflection phase. This is likely the reason why in both cases the critical coupling distance was underestimated. Apart from this systematic error, these monochromatic implementations could only change the gap in discrete steps as they were based on counting interference fringes.

The gap width d can be extracted from the spectral reflectivity data by means of a Fourier transformation. The fundamental frequency f in the Fourier spectrum is used for the evaluation as follows:

$$2d \cdot n_2 \cdot \cos\theta = f + \frac{\partial \varphi_r(k)}{\partial k}, \tag{3.2}$$

where the left hand side is the optical path length of the light in the gap. The right

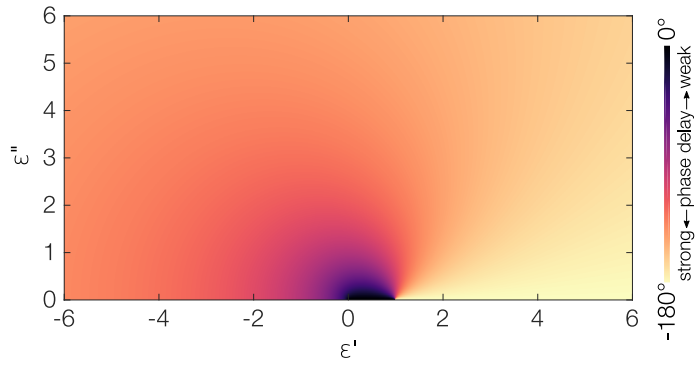

Figure 3.4: Reflection phase φ_r shown over the permittivity plane when illuminated from a medium with $\varepsilon = 1$ e.g. vacuum. Transparent media without any imaginary part in their permittivity give either a phase response of 0° or −180°, depending on whether epsilon is above or below those of the adjacent medium. All lossy media show a phase response that lies in between. The phase response has a singularity if both permittivities match; however, the reflectivity vanishes, too.

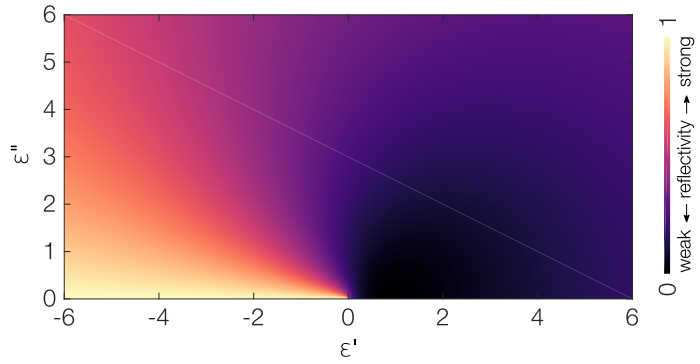

Figure 3.5: Reflectivity of a surface shown over the permittivity plane when illuminated from a medium with $\varepsilon = 1$, e.g. vacuum. The highest reflectivity is obtained from loss-free materials with negative permittivity, e.g. metals ($\varepsilon' < 0, \varepsilon'' = 0$). Here, the reflectivity is fully independent of the magnitude of ε. Fully vanishing back-reflection is only found for matching permittivities. A material with absorption always gives a back-reflection. A *perfect absorber*, therefore cannot be built from a single isotropic optical material.

hand side is composed of two influences on the spectral modulation pattern. First, the modulation frequency f resulting from spacing of the two interfaces. Second, the dispersion of the reflection phase φ_r, being non-zero for absorbing materials. The Fabry-Pérot cavity allows not only a single round trip for a photon, but multiple cycles. Thereby, higher harmonics, i.e. $2f, 3f, 4f \ldots$ are also present in the transformed signal. It is paramount that the lowest order of this series is taken. For ATR setups employing VIS with glass prisms, this is of no concern as the prism-gap interface has a reflectance of only a few percent. Multi-cycles in the cavity are thereby strongly suppressed.

Additional improvement to the accuracy is gained by evaluating not only the modulation frequency but also its spectral position. The spectral position is expressed by the phase of the modulation frequency α – not to be confused with the optical phase of the reflection φ_r. These quantities are related as

$$\alpha(k) = \varphi_r(k) + 2dn_2k\cos(\theta). \tag{3.3}$$

In particular, if the distance d is vanishing, $\alpha(k)|_{d=0} = \varphi_r(k)|_{d=0}$. However, measuring a modulated spectrum at $d = 0$ would require white-light of infinite frequency to resolve the wide spectral pattern of such a thin cavity. As the coupling distance d is already fully determined by the modulation frequency, the system becomes overdetermined by measuring α. This additional information can be used to improve the resolution by reducing the influence of noise as well as a verification of the underlying ellipsometry data. Figure 3.6 shows a polar plot with the frequency in radial direction and the corresponding phase in azimuthal direction. In this representation, a changing gap leads to a spiral around the origin. Especially for very narrow gaps with few or even single cycle modulation, evaluation of the phase significantly improves the accuracy. In the case of improper ellipsometry data, the evaluated frequency would be offset from the spiral.

3.4 Reflection phase dispersion

For absorbing materials with a non-constant $\varphi_r(k)$, $\alpha(k)$ is no longer a linear function of k that could be expressed as a single frequency $f = \frac{\partial\alpha}{\partial k}$. In such cases, it cannot directly be plotted as in Figure 3.6. However, the phase dispersion in the spectrum can

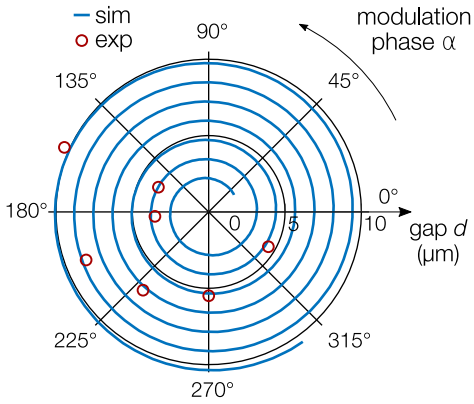

Figure 3.6: The modulation frequency f plotted together with its phase. In this representation, changing the coupling gap describes a spiral path. Concurrent evaluation of both quantities improves the accuracy and serves as a verification.

be precompensated by multiplying the modulation signal with $e^{-i\varphi_r(k)}$ before applying the Fourier transformation. This effectively cancels out the dispersion of φ_r in Equation 3.3 and reduces the modulation to a single frequency. If the sample's material absorption peaks are very broad and outside the spectral window, it might be sufficient to compensate the measurements by an offset $d_{\text{offset}} = \frac{1}{2n_2\cos(\theta)}\frac{\Delta\varphi_r}{\Delta k}$ that accounts for a linear slope in $\varphi_r(k)$. Figure 3.7 shows $\varphi_r(k)$ for a gold surface based on various permittivity data reported in literature. The d-band transitions around 500 nm that give gold its characteristic color are clearly visible as a peak in the phase response. Toward the NIR, the response becomes flat and can in most applications be approximated with a linear slope.

The presented method shares similarities with white-light Michelson interferometers or Fourier transform spectrometers used in the ultrashort pulse laser community. Here, white-light is uses to measure the group delay (GD) and group delay dispersion (GDD) of optical components.[65–69] Measuring the gap is to some extend the reverse process of measuring GD and GDD. For the calculation of GD and GDD from interferograms, the shifted distance in the reference arm is used to calculate the spectral phase. In our case, the reflection phase dispersion – that is a GD expressed as a distance rather than a propagation time – is previously known and the distance is to be calculated.

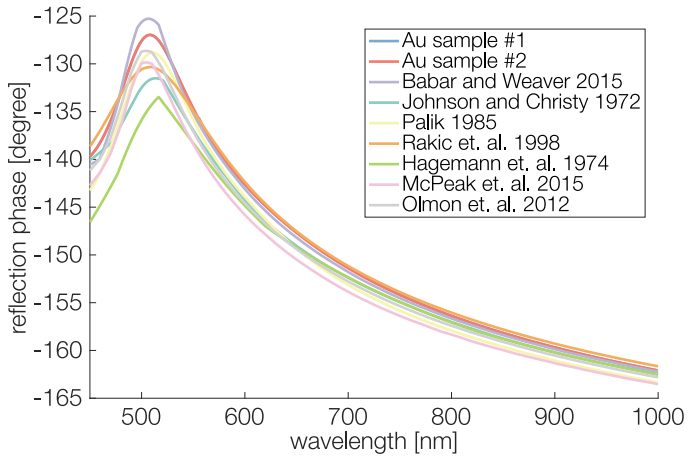

Figure 3.7: Reflection phase of gold samples reported by different authors. The peak in the phase response is a result of the d-band transitions that appear slightly above 500 nm and give gold its distinctive color. Differences between the underlying ellipsometry datasets are likely to stem from varying surface roughness as a result of individual sample preparation techniques.

3.5 Implementation

The white-light interferometry method was implemented in an ATR setup for k-space spectroscopy of SCTWs in the VIS and NIR regime. As sketched in Figure 3.2, the top of a conventional isosceles triangular prism was ground off parallel to the probing interface. The prism was made from SF11, a high refractive index glass with $n > 1.75$ ($\varepsilon > 3.06$) between 450 nm and 1000 nm. It provides sufficient permittivity contrast for most transparent materials.

A white-light beam coming from a fiber coupled white LED source (Cree XPEWHT-L1, 4000 K color temperature, 430-730 nm) is fed through the prism top. The beam is focused onto the sample with an opening angle of 1°. The divergence of the white-light is small enough for the Rayleigh length to be much larger than the coupling gap. Both interfaces are thereby in focus and interface reflections can interfere spatially coherent in the far-field. The white-light coming out of the fiber is fed in normal to the prism surface and the reflected signal coupled back into the fiber. After the fiber, a beam splitter is used to separate the forward and backward propagating signals. A significant part of the light is reflected at the fiber ends due to coupling losses. For such a spectrally broad beam these losses are virtually unavoidable and can be much larger

than the amplitude of the desired signal. The largest contribution comes from the initial coupling of the LED light into the fiber, where mode matching is hard to achieve due to the large emitter size and chromatic aberrations. The mismatched light, which would otherwise over-saturate the spectrometer detection, was blocked by placing a pair of crossed polarizers in the arms of the beam splitter. As the fiber is a non-polarization maintaining type, light that enters the multimode fiber is depolarized and a part of it is able to pass the second polarizer on the way back. Unmatched light that did not enter the fiber is, however, completely blocked at the second polarizer.

Besides absolute gap width readout, the method allows for parallel alignment of the prism and the sample. This is a crucial requirement for ATR spectroscopy; not only because the edges of a tilted surface would otherwise collide with the coupler. An uneven or tilted coupling gap leads to varying coupling conditions. It is experimentally challenging, if not impossible, to distinguish overcoupling or undercoupling from the losses of tilted coupling. Parallel surfaces with high accuracy (±1″) are adjusted by first, optimizing the contrast of the interference signal; and second, by laterally scanning the white-light measurement spot over the sample. By this means, the obtained constant gap width assures homogeneous excitation conditions across the complete light spot, being crucial for obtaining well-defined full-scale resonances in the ATR spectra.

3.6 Error estimation

It is obvious that the method stands and falls with the accuracy of the spectrometer. The lower end of the detectable range for the distance readout is limited by the signal-to-noise ratio (SNR) and dynamic range of the spectrometer. If the modulation period becomes wider than the spectrum, high resolution of the intensity is required to obtain sub-cycle frequencies[a]. The upper end of the range is set by the spectrometer wavelength resolution. When the spectral modulation period approaches the spectrometer resolution, it can no longer be resolved. This can also be thought of as the coherence

[a] This can no longer be done by means of a Fourier transform, as the finite spectrum of the light source acts as a windowing function to the spectrum. The frequency components of the spectral window dominate and limit the resolution in the frequency domain. However, sub-cycle periodicities resulting from gaps down to 370 nm were successfully fitted with a transfer-matrix-based multilayer model.

limit of the interferometer. While the overall broad-band white-light has a very short coherence length in the micrometer range, each of the separated spectral bins in the spectrometer has a much larger coherence length as they are very narrow-band. For the given case with a compact CCD spectrometer (Thorlabs CCS200/M, 200 nm–1000 nm, $\Delta\lambda = 2\,\text{nm}$, SNR $\approx$ 2000), the detectable range spans almost 3 orders of magnitude between 370 nm and 150 µm.

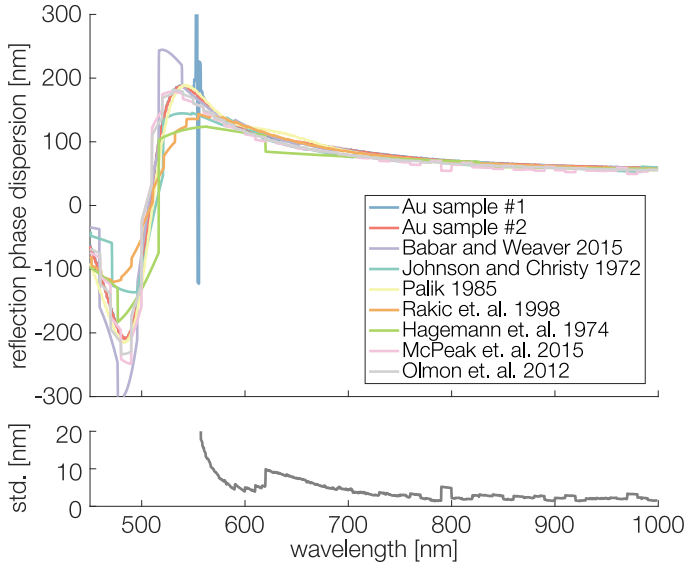

Figure 3.8: Dispersion of the reflection phase expressed as distance. Disregarding the spectral phase can lead to errors as large as 250 nm. The spectral dependency of the reflection phase is a large source of error in the determination of the coupling gap size. Precise ellipsometry data is therefore indispensable. The lower plot shows the standard deviation of literature data as a guide to estimate the influence of ellipsometry data. Far off any material resonances, the influence reduces to values as low as a few nanometers.

Given that the reflectivity spectrum is measured with sufficient precision and resolution, the dispersion of the reflection phase is left as the next largest source of error. Here, the accuracy of the ellipsometry data is of utmost importance, when absolute valued single-digit nanometer resolution is required. As there are many ways that ellipsometry data can miss the real dispersion curve, a straight forward derivation of the error is impossible. However, a test case was constructed as a practical guide for the accuracy of d. For an Au surface in the VIS region, d was calculated based on different ellipsometry

data reported in literature (see Figure 3.8). This has led to an uncertainty of $\Delta d = 1.7$ nm. Higher precision can be achieved through measuring the individual dispersion of the sample, which differs with material purity and surface roughness. Ellipsometry measurements of two Au film samples that were coated in the same batch and measured individually resulted in an error of less than 0.2 nm. In contrast, completely disregarding the influence of the reflection phase dispersion would result in an error as large as $\Delta d = 250$ nm.

Other possible sources of error are cosine errors, finite surface flatness, bending through compressed dust, and refractive index errors of the medium in the gap. Cosine errors occur when the beam is incident other than normal to the surfaces. The confocal beam path reduces this influence significantly. The angular mismatch was estimated to be ±0.1°, which translates into a relative error of on the order of 10^{-6}. The finite accuracy of optical surfaces contributes another source of error. Typically, polishing is guaranteed to be better than $\lambda/10$ or even $\lambda/20$ over a $L = 25$ mm aperture with $\lambda = 632.8$ nm. Over a smaller aperture it can be expected to scale down with $\sqrt{L}$ as the sample size is reduced. In the setup, samples with apertures no larger than 3 mm were used. Bending from compressed dust or other particles is another source of error, especially for sub-micrometer gaps. Although it is easily detectable thought the resulting force against the piezo actuators, it is hard to prevent in a non-cleanroom environment. Finally, the refractive index of air needs to be taken into account, in particular its dependency on temperature, atmospheric pressure and humidity. Being a relative contribution to the overall error, it is usually negligible, in particular for small gaps.

3.7 Concluding remarks

The presented setup can be used for gap control between 370 nm and 150 µm, serving as a versatile tool for precise evanescent coupling control. It is not limited to surface plasmon polariton and SCTW excitation, but has applications wherever well-defined air-gap based evanescent coupling is required. Among others, this includes ATR spectroscopy, waveguide coupling or excitation of ring-resonator structures. Although not required in the particular case, the spatial and galvanic isolation provided by the fiber connection between the compact sensing head and the detection system enables functionality

under a broad range of measurement conditions, including harsh conditions of high temperature, strong electromagnetic fields, and humidity. Applications in nonlinear optics can benefit from the real-time feedback to stabilize the coupling even under strong temperature drifts, as happens when tuning the excitation angle from off-resonance to on-resonance excitation.

In conclusion, spectrally resolved white-light interferometry was used to overcome technical challenges of the air-coupled Otto configuration. The technique allows angle resolved spectroscopy with stabilized critical coupling conditions, thus granting the possibility to experimentally determine mode dispersions of any flat sample. Tuning the coupling gap allows critical coupling for a large wavelength range compared with systems that are optimized for a fixed wavelength such as grating couplers or Kretschmann geometries. Quantifying the coupling gap not only assures repeatability and comparability but can also serve to measure propagation losses from previously unknown or uncharacteristic samples. By providing the necessary control over evanescent ATR coupling with tunable air gap in a reliable and widely applicable manner, it is envisioned that the method paves the way for multiple future studies in the field of nanophotonics.

Chapter 4

New materials for thin-film waveguiding

The existence of SCTW modes in film materials of arbitrary homogeneous permittivity has already been shown. Attention is now drawn to compound materials. The excitation of SCTW modes is not limited to homogeneous materials, but can be implemented with materials that have a subwavelength structure.

The focus will lie on compounds made from metal nano-particles embedded in a polymer brush host. It is not only popular nano-particles that can be made to have custom tailored functionality, but also the host matrix that can be functionalized though nano-engineering. Over the last two decades, polymer brushes have attracted the interest of many researchers coming from the fields of polymer science and chemistry. Polymer brush structures are thin films consisting of nanometer-thin polymer chains that are grafted to a substrate at one end.[70] These grass-like structures have the ability to shrink or swell depending on a variety of environmental parameters as depicted in Figure 4.1. It is the two counteracting influences of osmotic pressure and entropy that allow a reversible change between the two states. Osmotic pressure straightens the brush and increases the thickness. Entropy on the other hand lets the polymer chains collapse and decreases the thickness. Polymer films can be used for the functionalization of surfaces. Unconventional properties of the surface can be realized such as adjustable wettability e.g. tuning between a hydrophobic and hydrophilic state.[71] Furthermore, the friction between the brushes and a solid material has been shown to be controllable through the swelling.[72] Lastly, the biocompatibility and photophysical properties of

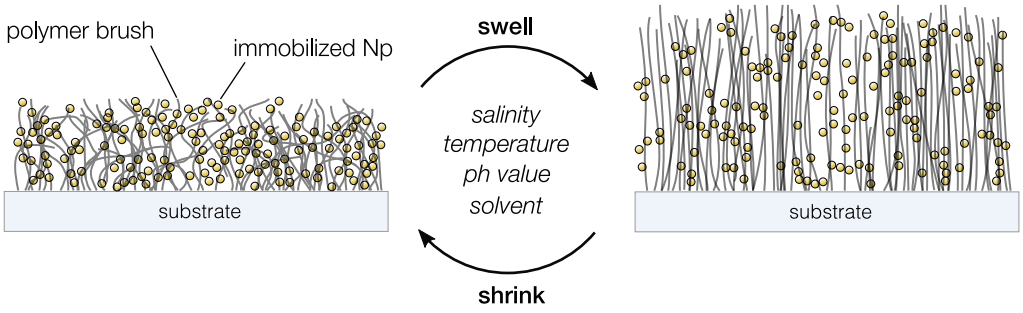

Figure 4.1: Polymer brush surfaces built from end-grafted polymer chains can form a grass like surface. A variety of parameters alter their morphology, switching between a collapsed and a straightened state of the brush. Metal nano-particles can be immobilized inside the brush structure to intensify the optical response of the reversible transition.

polymer brush surfaces are of great interest to the field of life-sciences.

Hybrid structures of metal nano-particles embedded in functionalized polymer brush films are of particular interest to the field of optics. The strong absorption of metallic nano-particles intensifies the optical response of structural changes happening at the nanometer-scale. Two aspects of these brush/metal nano-particle hybrids are especially relevant in the context of SCTW. First, the in-situ tunability of the optical properties and second, the response to external stimuli.

Swelling of brushes leads to changes in the dielectric environment surrounding the metallic nano-particles as water or solvent enters the straightening brush. This results in a shift of the localized surface plasmon resonance (LSPR) as the dielectric loading is reduced. Tuning the optical properties *in-situ* and in a reversible way is a powerful technique for the realization of customized and adaptable soft-matter optical devices. The ability of polymer brushes to support self-assembly of nanoparticles adds even more – making these brush/nano-particle hybrids a promising playground for the development of novel metamaterials and epsilon-near-zero media.[73]

The responsiveness to external stimuli is an obvious invitation for the design of optical sensors. In previous works, a multitude of planar sensors have been realized based on hybrid brush structures. The monitored environmental parameters range from temperature,[74] pH value,[75] electrochemical potential[76] to solvent concentrations[77] or

glucose level.[78] Resonance shifts accompanying the brush transition are easily resolved in the transmission or reflection spectra[70,79] using common UV/VIS spectrometers. This makes such sensors simple and cost efficient devices that allow remote readout without additional electronics. However, the spectral resonance of nano-particles is very broad. Common metal nano-particles made from gold, have a resonance width of many tens of nanometers. These sensors are very limited in their detection efficiency considering that the resolution of resolving a resonance position decreases with the resonance width. The LSPR linewidth of gold nano-particles is broad and the interaction length for the transmitted light is as small as the brush films are thin. The former limits detectable wavelength changes, while the latter sets a lower limit to the detectable concentration.

The length of the interaction between the light and sensor surface can be increased in a symmetric cladding setup directly employing the functionalized film as a waveguide. The light is guided along the film of subwavelength thickness rather than straight through it. Thereby, the interaction length of the light and the thin film is prolonged from a few tens of nanometers to many hundreds of micrometers. Probing the sharp k-vector ($k'' \ll k'$) by ATR spectroscopy rather than the spectral amplitude is more sensitive by many orders of magnitude. Conventional ATR spectroscopy, as used in surface plasmon resonance spectroscopy (SPRS) sensors, is a well proven laboratory method used to resolve molecular concentrations.[80] In this chapter it is shown that functionalized nano-composites – despite strong optical losses and disorder – can form waveguides.

4.1 SCTW modes in Au:PNIPAM thin-films

To demonstrate the suitability of brush/metal nano-particle films for symmetric cladding thin-film waveguiding, a poly(N-isopropylacrylamide) (PNIPAM) polymer brush sample was designed. The film was synthesized in a two-step process. First, a monolayer of 2-bromo-2-methyl-N-(3-(triethoxysilyl)propyl)propan-amide (BTPAm) was applied to a substrate. A 500 µm thick optical grade polished fused silica substrate (Microchemicals GmbH) was used. In a second step, the polymer chains were end-grafted to the prepared BTPAm-coated substrates. After preparation of the PNIPAM brush film, the

sample was incubated in a 5 nm gold nano-particle (Au-Np) solution for 24 h to allow the particles to diffuse into the polymer matrix. More details on the synthesis procedure can be found in Appendix A.

The thickness of the final film was measured with atomic force microscopy (AFM) and found to be in the range of 60 nm in the collapsed state under ambient conditions. To validate the homogeneity of the Au-Np distribution and to check for possible agglomerations, scanning electron microscopy (SEM) images were taken of the sample (Zeiss DSM 982 GEMINI at ZELMI, TU Berlin). The results are shown in Figure 4.2.

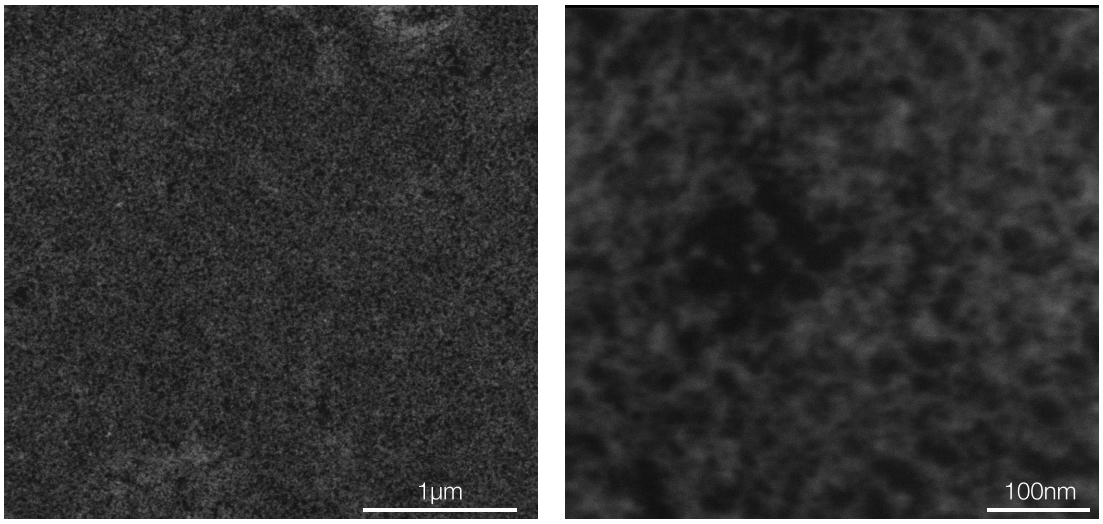

Figure 4.2: Scanning electron microscopy (SEM) images of the PNIPAM surface with immobilized Au nano-particles. The sample homogeneity is sufficient to treat the response of the materials with an effective medium approach for VIS/NIR wavelengths. Some small clusters are visible, yet their characteristic size is clearly subwavelength, thereby having negligible influence in the form of scattering losses. Images were taken with a Zeiss DSM 982 GEMINI at ZELMI, TU Berlin.

Two types of Au-Nps coating were evaluated, based on citrate and MDA coated Au-Nps. The MDA capped particles were favored for their high concentration while still being free of agglomerations. The resolution of SEM is limited due to the charging effects of the non-conductive sample. Although individual particles (5 nm) are hard to demarcate, a homogeneous distribution is visible over the scan-field of several micrometers. The penetration depth of the beam is rather short and only particles close to the surface

contribute to the signal. SEM studies with higher resolution have previously been done by growing the same PNIPAM brush structure on conductive silicon waves.[70]

4.2 Optical properties

The coated PNIPAM wavers were measured for transmission in a UV/VIS spectrometer under standard ambient conditions in an air atmosphere. The results are shown in Figure 4.3. It follows from the nature of the coating process, that wavers are always coated on both sides. A clear LSPR is visible around 550 nm with roughly a 25 % decrease over the off-resonance value in the NIR. The line-width of the resonance is very broad, spanning more than 50 nm.

The typical resonance shift for a transition from an unswollen state to a swollen state is known from literature[70] to be in the range of 5 to 15 nm, while being contemplated by a 5 % refractive index change decrease. Direct inter-particle coupling of the LSPR has been shown to result in red-shifted resonances.[81] These studies report resonances around 540 nm and below for moderately packed nano-particles inside a PNIPAM brush. The shifted resonance wavelength is an indication of tight particle packing inside the sample.

Spectroscopic ellipsometry was employed to obtain the permittivity of the sample. The incubated film was measured with the help of three reference samples in a spectroscopic ellipsometer (SENresearch 4.0, Sentech Instruments GmbH). First, an uncoated quartz substrate was measured and validated against literature values[a]. Then, bare unswollen PNIPAM films with different thicknesses were measured. The film thicknesses were chosen above and below the thickness of the final sample containing the Au-Nps. The 60 nm film incubated with the MDA coated Au-Nps was measured under 50° and 70° inclination over the range 450 to 1000 nm.

The results of the ellipsometry data – shown in Figure 4.4 – were fitted with SpectraRay (Sentech Instruments GmbH) to extract the desired permittivity data. The response of the brush/nano-particle hybrid was modeled as an effective medium being a bare PNIPAM host matrix with Au inclusions. The response of the Au-Nps was modeled with a sum of Lorentz oscillators. A transmission spectrum (0° inclination) was added

[a] See Appendix C for references of the permittivity data used.

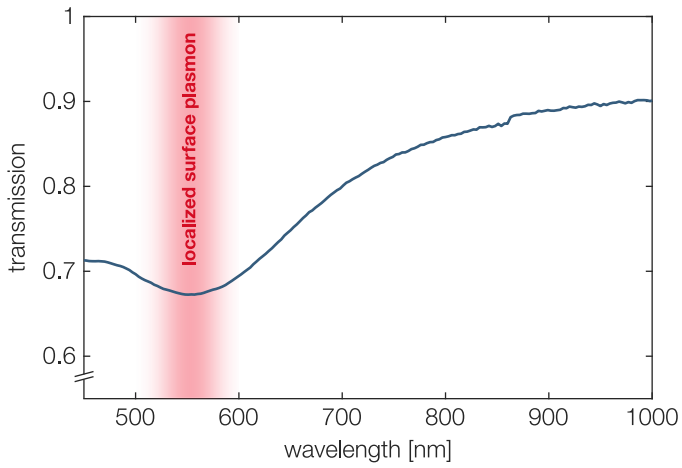

Figure 4.3: Transmission spectra of a PNIPAM polymer brush with immobilized 5 nm Au nano-particle. A broad localized surface plasmon resonance is visible around 550 nm having more than 50 nm line-width. The shown spectra refers to a double sided Au:PNIPAM coating on a polished fused silica waver under standard ambient conditions in air atmosphere – i.e. in an unswollen state.

to improve the fit. The thickness of the sample was found to be in agreement with the AFM measurement. The contribution from the back-side of the sample was assumed to add in an incoherent manner to the reflectance stemming from front-side.

The results of the ellipsometry are shown in Figure 4.5. The bare PNIPAM possesses a permittivity in the range of 2.26 to 2.18, corresponding to a refractive index of 1.50 to 1.48. The permittivity lies very close to the permittivity of the fused silica substrate (2.15 to 2.10). The incubation with the nano-particles boosts the optical response from the initial values on the real axis toward a higher permittivity around $\varepsilon \approx 4 + 1.5i$. A clear resonance is visible, having a clockwise circular path in the permittivity plane. The highest imaginary values are found around 550 nm, while the highest magnitude is clearly red-shifted. In particular, excitations with NIR light benefit from the strong increase of permittivity contrast with only modest losses.

4.3 Inhomogeneous nano-particle distribution

It is known that nano-particles are not distributed homogeneous throughout PNIPAM brushes.[70] While the horizontal distribution can be easily verified by means of SEM,

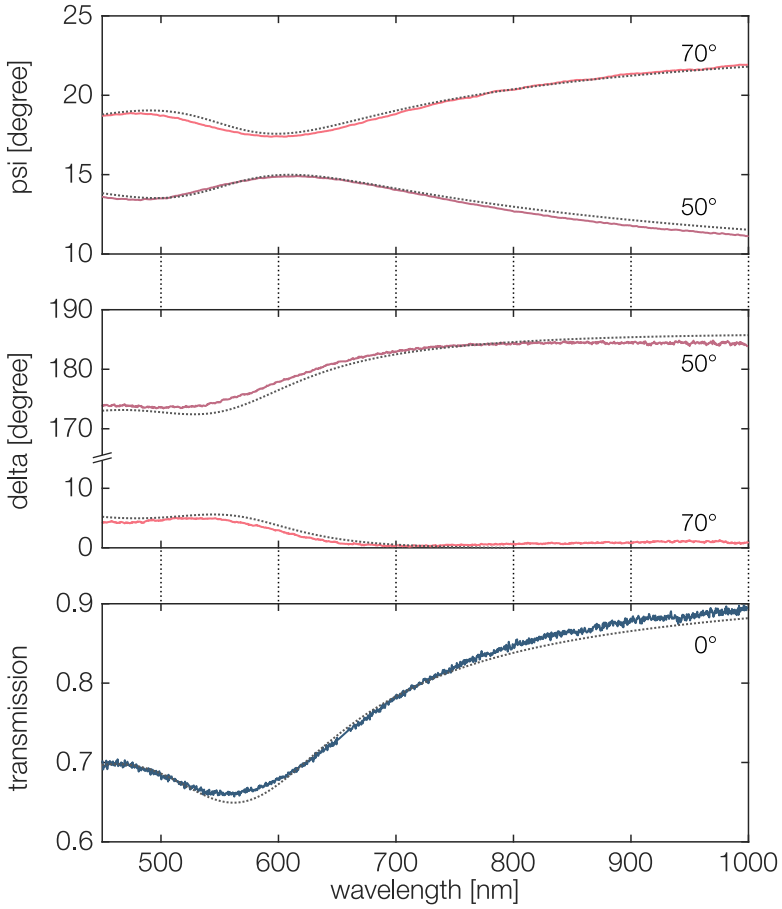

Figure 4.4: Ellipsometry data used to fit the permittivity values of the PNIPAM brush/gold nano-particle film on a polished fused silica substrate. Experimental data (solid) and fitted model (dotted) show good agreement over the VIS/NIR range. The two angular settings were fitted together with the transmission measurement. The sample was coated on both sides of the 500 µm waver. The incoherent reflection from the back-side was also considered in the model.

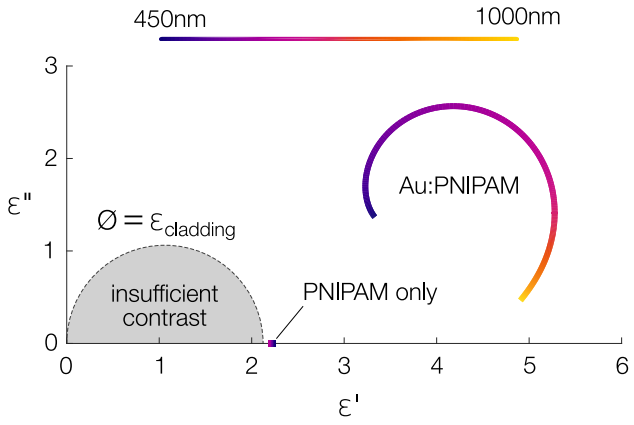

Figure 4.5: Ellipsometry data of film that was used in the experiment. The values for ε' increase from 2.2 up to 5.3 through the incubation. The dielectric contrast to the fused silica substrate with $\varepsilon' \approx 2.11$ is significantly improved.

the lateral distribution requires much more sophisticated techniques such as neutron reflectometry. The distribution of the particle and any characteristic length is clearly sub-wavelength in a 60 nm film. A trustworthy extraction from ellipsometry data alone is therefore challenging. Neutron reflectivity measurements of PNIPAM brush/nano-particle have shown that the particle coating has a strong impact on the distribution in the brush.[70] In particular, the hydrophobic nature of MDA prevents the coated nano-particles to fully penetrate the brush and spread with lateral homogeneity. Unlike citrate coated nano-particles, that distribute easily inside the brush, MDA coated particles are assumed to form a thin 2D layer in the upper regions of the brush. Here, SCTW propagation properties – being highly sensitive to the film thickness – can give additional insight on the particle distribution. Although a full reconstruction of the profile is impossible from a single propagation vector, characteristic lengths of a distribution can potentially be found through variation of the particle distribution in a multilayer transfer matrix model.

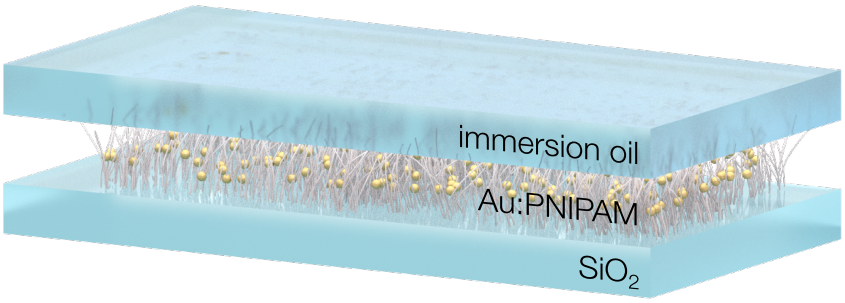

Figure 4.6: Illustration of an SCTW based on a brush/nano-particle hybrid structure. An immersion liquid – precisely matched to the refractive index of the substrate – is used to mimic a symmetric cladding.

4.4 Au:PNIPAM waveguide preparation

The necessity of a symmetric cladding for SCTW propagation requires the preparation of a superstrate with matched optical properties. A matching liquid (Cargille #06350) with refractive index precisely replicating the dispersion of fused silica was used on the top side of the sample. The refractive index of the liquid is specified to four decimal places up to 840 nm wavelength and three places above (25 °C). It has a temperature coefficient of $-3.6 \cdot 10^{-4}\,{}^{1}/_{\mathrm{K}}$ and a viscosity of 80 cSt. The influence of the matching liquid oils on the swelling of the PNIPAM brush was studied using atomic force microscopy. The PNIPAM sample was tested against a broad range of immersion oils[b]. Through indentation measurement it was verified that the oils did not cause any swelling. This is in accordance with the hydrophilic nature of the brush. The structure was assumed to remain in a collapsed state when covered with the immersion oil, which in turn allows

[b] The tested oils were Zeiss Immersol 518F and 518N, Cargille immersion oil type A and B, and Cargille fused silica matching liquid #06350.

the use of the optical properties measured under air atmosphere.

4.5 ATR spectroscopy setup

An attenuated total reflectance setup was employed to confirm the existence of waveguide modes in the sample as well as to determine their dispersion. The custom built broad-band k-spectroscopy setup (see Figure 4.7) was used to resolve both the angular and spectral dependency of the reflectance signal. The coupling prism was made from SF11, a high refractive index glass with $n \approx 1.8$ ($\varepsilon \approx 3$). The top of the prism was ground off and polished to allow interferometric distance control as explained previously.

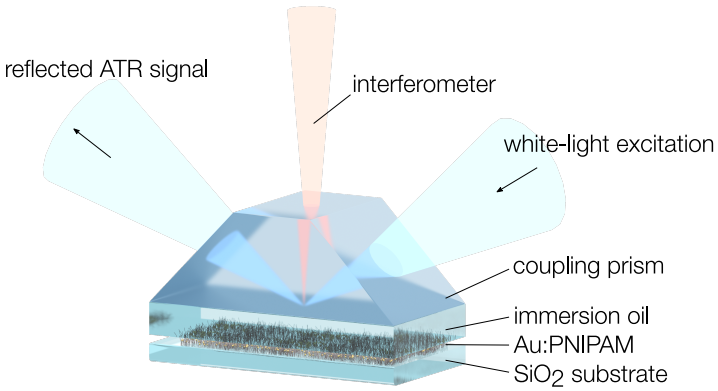

Figure 4.7: Sketch of the attenuated total reflectance (ATR) setup used to probe excitable modes in the SCTW waveguide. The high refractive index coupling prism (SF11) was illuminated by white-light. A spectrometer was used to analyze the reflected signal with respect to exit angle and wavelength. A second white-light source is fiber-coupled through the prism top and used for interferometric measurements of the gap between the sample and the coupling prism.

For the ATR spectrograms, a broad-band beam was used as the excitation source. It was combined from an LED (Osram Oslon SSL, 4000 K color temperature) and a halogen light source to achieve full coverage of the VIS and NIR spectrum (450 nm–1000 nm) with an acceptable power level. The light sources were collimated individually to a 20 mm diameter beam and then focused onto a pinhole. The pinhole acted as a spatial filter, matching the beam characteristics of both sources. The combined beam was filtered for p-polarization before being focused onto the sample surface with an f = 40 mm achromatic lens (see Figure 4.8). The prism was positioned such that the

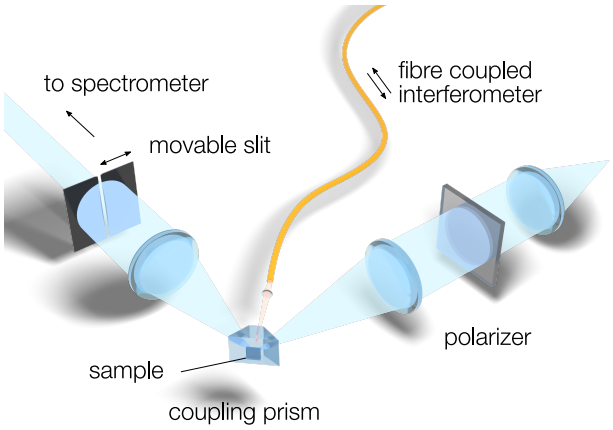

Figure 4.8: The spectroscopic ATR setup used for the linear excitation of surface waves and SCTW modes in the VIS and NIR regime. A movable slit was used to analyze the reflected signal with respect to exit angle and wavelength. A whitelight interferometer is fiber-coupled through the prism top and used to control the gap between sample and coupling prism. Relay lenses present in the original setup have been omitted in the illustration.

angular center position of the beam illuminated the total internal reflection (TIR) edge of the SF11/SiO_2 interface with an angular spread of ±10°. The TIR angle is located between 53.5° and 55.5° for the pairing of SF11 and SiO_2, with smaller angles at the blue end of the spectrum. All angles indicate internal angles between the surface normal of the prism and the incident beam. The reflected beam exiting the prism was collimated by another achromatic doublet, identical to the focus lens.

The angular spectrum forming in the back-focus of the collimating lens was imaged with a relay lens configuration (not shown in the figures) onto the 20 µm entrance slit of a spectrometer (Thorlabs CCS200). The spectrometer was mounted on a motorized linear stage. The entrance slit served as an angle selective filter to extract the ATR signal as a function of both wavelength and angle.

For the measurement of the Au:PNIPAM sample, the gap between prism and sample surface was fully filled with the matching fluid. A liquid with low viscosity was chosen for better flow in and out of the sub-micron coupling gap. The sample was mounted on a platform with six degrees of freedom to adjust position and parallelism. A second platform, driven by piezo actuators, was used for fine-grained control of the coupling gap. The spacing was monitored with the white-light interferometer presented earlier.

Spectral data was recorded with 1.3 s integration time for each of the 512 positions. Before the immersion oil was applied between the coupler and the sample, an angle dependent ATR scan was taken of the prism-air interface. This material combination has a significantly lower critical angle than the SF11/SiO_2 matching liquid interface. As, by theory, the reflection coefficient above the critical angle is exactly 1, this scan was used to normalize all subsequent measurements thereby correcting for any vignetting or otherwise inhomogeneous illumination. A scan from the prism-immersion oil interface was taken to precisely locate the critical angle and map out its dispersion. The TIR edge was fitted and later used for referencing the light-line in the final measurements.

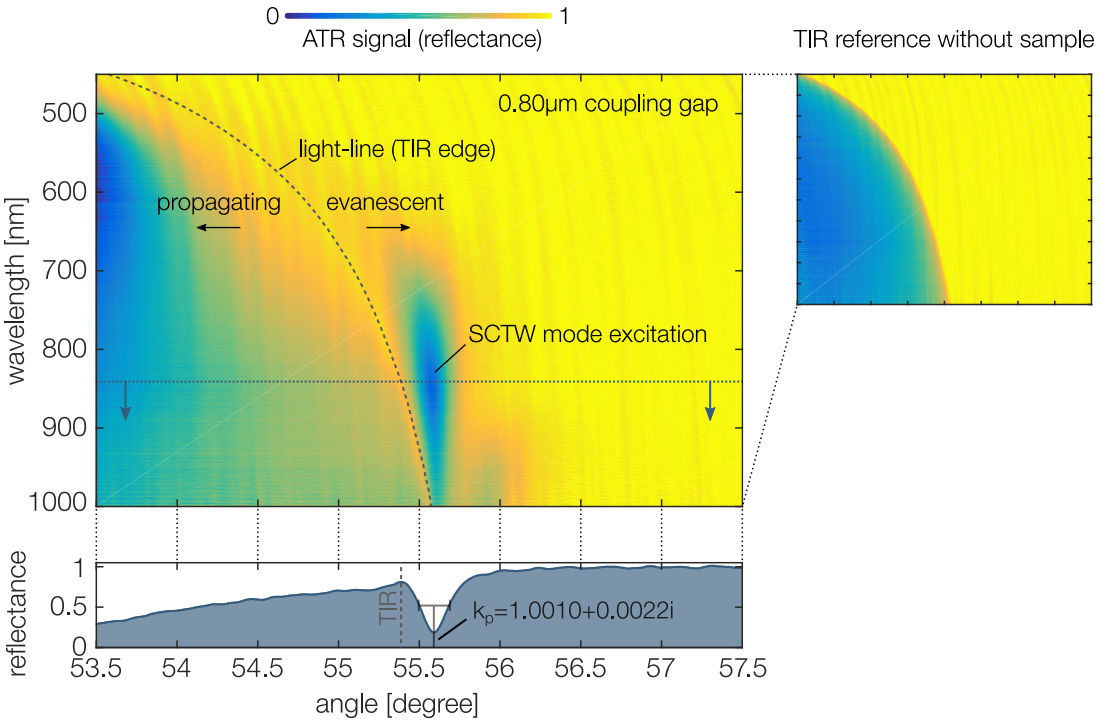

Figure 4.9: Broad-band ATR spectrogram of an Au:PNIPAM SCTW coupled with a 0.80 µm gap. The insert on the right depicts the TIR angle dispersion out of which the light-line was extracted. A clear excitation dip is visible in the NIR with critical coupling around 850 nm excitation wavelength. From the angular width and the center position of the reflectance dip, the propagation constant can be calculated.

An ATR spectrogram of the Au:PNIPAM brush sample measured with 0.8 µm coupling gap is shown in Figure 4.9. The light-line was extracted from the TIR edge measured

separately. With the help of the light-line, evanescently confined modes can be separated from the Fabry-Pérot modes that are also present in the multilayer stack. A resonance beyond the total internal reflection angle is visible, centered around 850 nm with a spectral width of more than 100 nm. This dip provides clear evidence of evanescent in-plane modal propagation. The position of the resonance together with its angular width was used to calculate a propagation constant of $k_p = 1.0010 + 0.0022i$ at the point of critical coupling.

SCTW excitations in other spectral regions were measured through variation of the coupling distance. The gap was used to control the coupling strength between the incident field and the modes in the sample. Excitations at the blue end of the spectrum require much narrower gaps for three reason. First, the characteristic length of the evanescent decay is shorter, which results in weaker coupling. Second, the film thickness is larger in relation to the wavelength, resulting in shorter propagation length that in turn requires stronger coupling. Last, the permittivity as measured for the Au:PNIPAM sample is more suited for propagation at the red end of the spectrum due to a larger $|\varepsilon_1|$ and slightly lower ε_1''. Results of the coupling strength variation from 300 nm to 1.6 µm are shown in Figure 4.10. Evanescent mode excitations have been determined throughout the whole spectral range, matching the expectations derived from the permittivity data. As the coupling was varied, critical coupling was found throughout the whole wavelength range. The measured propagation properties vary between 1.0013 and 1.0001 for the real part. Higher confinement with lower propagation length appears at the shorter wavelength end. Here, the optical thickness of the core is larger, thereby biasing the compromise between confinement and propagation length toward confinement. The imaginary part of the propagation constant was found to be between 0.013 and 0.001 with a clear tendency for better propagation in the NIR region. Here, the angular resonance width of the SCTW excitation even approaches the setup resolution of 0.1°, leading to a washed out reflectance dip. The propagation length at the blue end is slightly below 100 wave cycles while at the other end, around 1000 cycles were achieved.

Compared to the plane-wave absorption length of the sample – lying between 3.3 and 22 wave cycles – these results demonstrate a vast increase of propagation length. It is concluded that the disorder of the composite structure was not found to have any negative impact, which would present itself in the form of scattering.

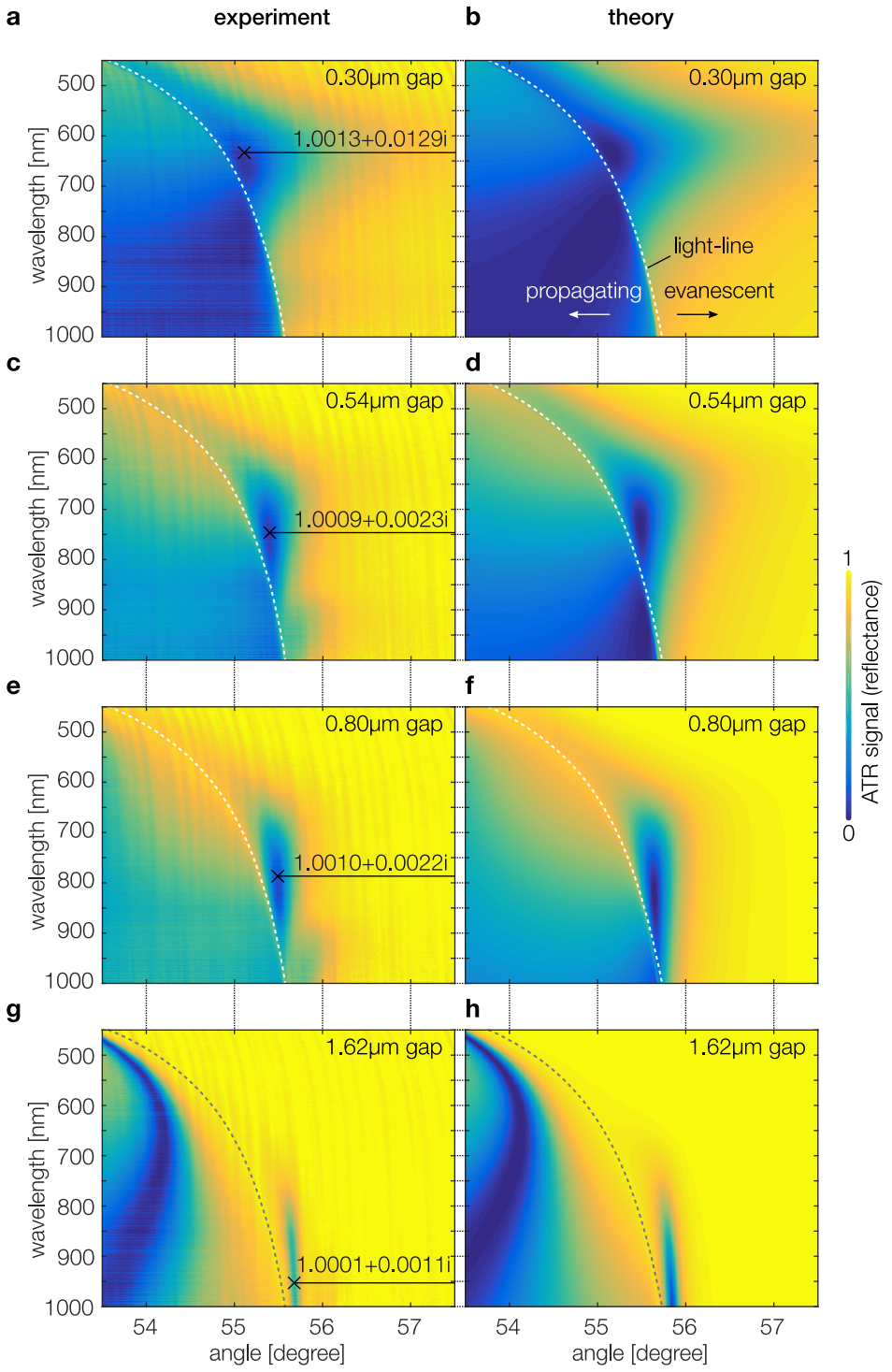

Figure 4.10: (a,c,e,g) Experimental and (b,d,f,h) theoretical ATR signals as a function of angle and excitation wavelength for different coupling gaps. A decrease in intensity indicates coupling to modes. The light-line marks the border for bound solutions that are evanescently confined to the waveguide structure. Sharp resonances can be seen that demonstrate the excitation of SCTW modes inside the Au:PNIPAM structure. The coupling gap was varied to excite the SCTW modes at all wavelengths and to map out the dispersion. The position and width of the resonances were used to extract the normalized propagation constant k_p that are displayed alongside the point of critical coupling.

The ATR response was additionally calculated theoretically with a transfer matrix algorithm. The results are shown in the right column of Figure 4.10. A straight forward implementation with a homogeneous 60 nm permittivity profile did not bring comparable results but resulted in large deviation from the recorded ATR spectrograms. The experimental data proved much shorter propagation length and different resonance profiles than the calculation. An inhomogeneous permittivity profile was therefore modeled and fitted to the experiment. A decreasing particle concentration was modeled with a Gaussian ($\propto \mathrm{e}\{-x^2/(2\sigma^2)\}, \sigma \approx 13\,\mathrm{nm}$) profile. For the multilayer transfer matrix algorithm, the permittivity profile was discretized into sufficiently thin layers. The coupling gap sizes were taken from the corresponding experimental interferometer measurements.

The half-sided Gaussian distribution was found to have excellent agreement with the experimental data over the whole wavelength range. The resulting theoretical curves resemble both the position and width of the resonance over the whole spectral region as well as for a range of different coupling strengths. The characteristic length of the inhomogeneity being $\sigma \approx 13\,\mathrm{nm}$ is in accordance with the expectation. The hydrophobicity of the MDA coated nano-particles allows only a very shallow penetration into the hydrophilic PNIPAM brush. This leads to a greatly increased particle density close to the surface which effectively decreases the core thickness and increases the permittivity contrast.

4.6 Nonlinear ATR spectroscopy

The propagation of light inside a waveguide or along a surface also has applications in the field of nonlinear optics. The mode – fed by a coupled far-field – provides a resonator structure that can be harnessed for a variety of effects that are beyond reach with linear optics. The local intensity at the interfaces of the waveguide can have greatly increased values compared to the field outside of the structure. It comes as no surprise, that waveguides have been used for the generation of nonlinear optical effects that depend strongly on high intensity.

In a co-authored publication,[50] it was demonstrated earlier that the concept of field enhancement in waveguides can also be used with SCTW structures in highly absorbing

transition metals. Absorbing materials are well-suited candidates as their nonlinear susceptibility experiences a strong boost close to optical resonances.[82–84]

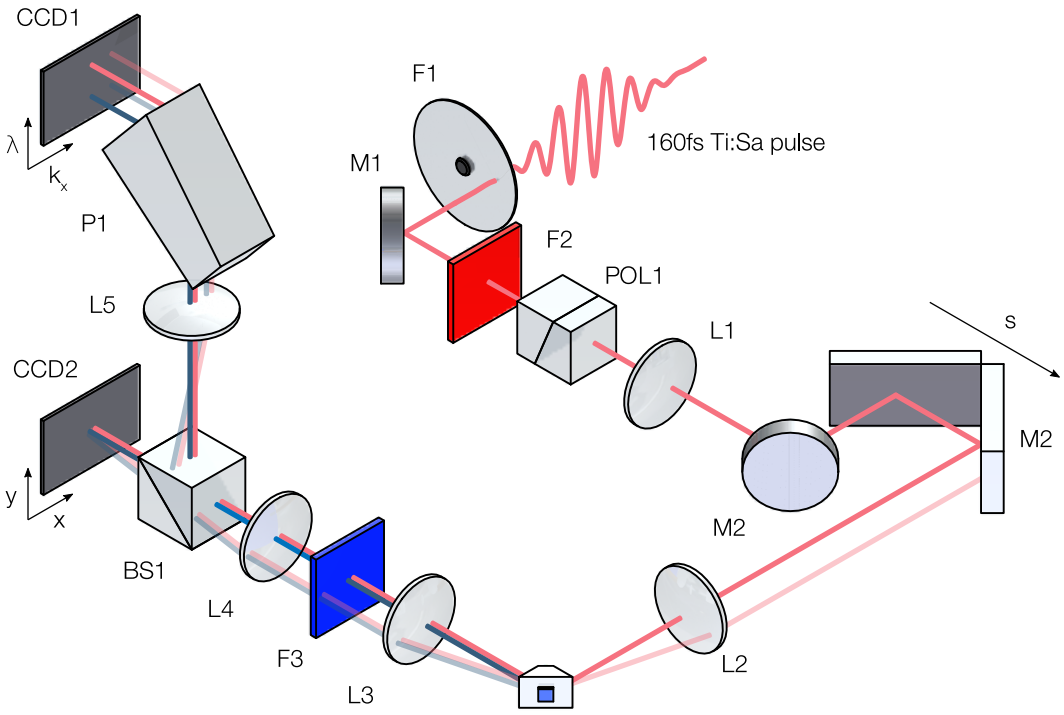

Figure 4.11: For the nonlinear ATR spectroscopy, a p-polarized 160 fs titanium sapphire laser pulse is filtered (F1,F2) and positioned with a motorized retroreflector assembly (M2). A matched pair of f = 60 mm lenses is used for excitation and detection of the angle-specific scan. Two CCD detectors map out k-space and x-space of the sample reflection. The spectral domain is mapped through a dispersive Pellin-Broca prism and allows the separation of nonlinear contributions of the fundamental excitation beam.

The bespoke Au:PNIPAM sample was measured with nonlinear k-space spectroscopy to demonstrate that not only homogeneous transition metals, but also brush/nanoparticle based SCTWs can have applications in the field of nonlinear optics. The setup, as sketched in Figure 4.11, allows the ATR coupled excitation with short femtosecond NIR pulses and spectroscopic detection of the system response. The setup shares the sample positioning mechanics and white-light interferometry with the linear ATR setup

described before. A 160 fs titanium sapphire (Ti:Sa) laser pulse with a center wavelength of 860 nm was used for the excitation of nonlinear effects inside the Au:PNIPAM sample. The beam was filtered using a gray filter wheel (F1) and a colored glass filter (F2) for intensity control and laser fluorescence suppression, respectively. A retroreflecting mirror assembly (M2) was mounted on a motorized stage to position the beam ahead of the excitation lens (L2). A long focal length lens (L1) was used to focus the collimated beam from the laser onto the back-focus plane of the excitation lens (L2), allowing an angle-specific excitation scan. All lenses were set up in an *f-f* scheme with coinciding focal planes such that position (x-space) and momentum (k-space) could be clearly separated according to Fourier optics. A matched detection lens collected both the fundamental beam and the generated second harmonic beam coming from the sample. The colored glass filter (F3) absorbed most of the fundamental light to equalize the intensity of both beams. Without equalizing, both beams could not have been measured on the same CCD to the limited dynamic range of these. Through a relay lens configuration and a prism, the angular image (k-space) of the sample was mapped onto CCD1. The horizontal axis mapped the projected momentum k_x of the beams exiting the sample. The vertical axis provided spectral dispersion that was used to separate fundamental and nonlinear parts of the beam. A non-polarizing beamsplitter (BS1) divided the beams. An x-space image was additionally projected onto CCD2 to characterize both position and momentum of light coming from the sample[c].

The same Au:PNIPAM sample used for the linear measurements was excited with 860 nm pulsed laser light from the Ti:Sa source. The incident beam was scanned from 53° to 59°. The reflectance of the fundamental beam was recorded on the CCD together with light originating from second harmonic generation (SHG). Higher order nonlinearities such as third harmonic generation (THG) are inaccessible due to the limited UV transmission of the used optical components. The results of the measurement are depicted in Figure 4.12. The fundamental reflectance curve shows a dip in the evanescent regime. A frequency doubled signal resulting from second harmonic generation is found at the same position. Angles on the x-axis refer to the input angle of the fundamental beam for both curves. The signature of the SHG signal clearly relates the peak to the SCTW mode that acts as a resonator. A slight shift to smaller angles is observable for

[c] This refers to an incoherent detection and does not violate the Heisenberg uncertainty.

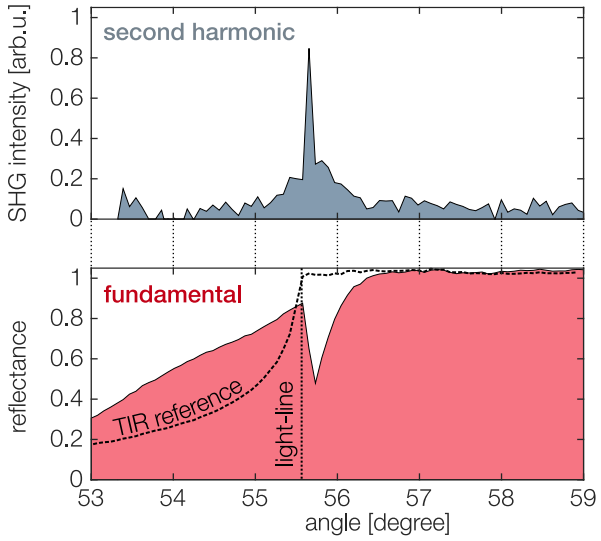

Figure 4.12: Second harmonic yield of Au:PNIPAM brush, measured together with the fundamental reflectance under pulsed Ti:Sa short femtosecond pulsed illumination. A strong increase of the SHG intensity is found upon excitation of the SCTW mode as indicated by the drop in the fundamental reflectance.

the peak compared to the dip position. This is an accordance with a previous study[85] that investigated second harmonic yield in the Otto and Kretschmann configuration. It was shown that the outcoupling efficiency shadows a large portion of the SHG. Its angle-dependency favors outcoupling of light with smaller momentum and results in a shifted centroid of the peak.

It has to be noted that even-order non-linear processes are forbidden in centrosymmetric materials such as the Au:PNIPAM brush. The origin of frequency doubling in centrosymmetric materials lies in the symmetry breaking at interfaces of dissimilar materials.[86,87] Thereby, the nano-particle inclusions in the brush can contribute a non-linear response under short pulse excitation. From the angular profile of the SHG yield it can be derived that the highest local fields are found upon coupling the waveguide mode. The *absolute* nonlinear yield of surface nonlinearity remains a difficult task both experimentally and theoretically.[88,89] Comparison with previous measurements[50] done with chromium or molybdenum based SCTWs under similar conditions revealed that

the yield of Au:PNIPAM waveguides is at least half an order of magnitude lower.

4.7 Concluding remarks

Functional surfaces such as PNIPAM brushes can be made to actively react on a variety of environmental parameters. They provide an excellent platform for the construction of low cost and chemically stable sensor platforms. With the help of an Otto-type ATR setup, a nano-particle filled PNIPAM brush was tested for SCTW modes. It was demonstrated that even highly disordered brush/nano-particle films can be used for waveguiding with superior propagation length. The modal propagation constants, found through variation of the coupling strength, have proven an immense increase of the interaction length compared to a transmission type geometry. A gain of almost two orders of magnitude is expected to result in greatly enhanced sensitivity of polymer brush based sensors. The material system used in the experiments can be modified to use low refractive index polymer substrates with optical properties matched to water. This would make the sensor system compatible with surface plasmon resonance based sensor (SPRS) systems that are widely used in life-sciences. SCTW modes in brush/nano-particle films, such as the ones demonstrated, can easily propagate with losses that are an order of magnitude lower than single-interface surface plasmon polaritons on gold surfaces.

Chapter 5

Quantum noise in ATR-based sensing

The surface plasmon resonance sensor (SPRS) is one of the prominent applications in the field of plasmonics. While many other discoveries in the field of plasmonics are still waiting to be applied in commercial products, SPRS has already become an established analytical method for chemistry, biology, and life sciences. Its sensitivity stems from the surface plasmons propagation along the interface, being highly sensitive to small changes of the dielectric environment near the surface. In the course of the propagation, analytes perturb the modal phase velocity, which is detectable as an angular resonance shift by techniques such as attenuated total reflectance. Starting with initial works[90,91] in the early 1980s, the field of SPRS has since evolved tremendously. To date, SPRS devices are capable of detecting a myriad of substances at very low concentrations.[80] Specifically coated surfaces provide the required selectivity, differentiating SPRS devices from classical refractometers. In many cases, ligands are immobilized in a thin Dextran matrix on top of a gold surface and bind the analyte flowing past the surface (see Figure 5.1). The range of applications covers, for example, medical diagnosis with the detection of biomarkers, drugs, antibodies, and hormones.[92–95] Food inspection benefits from the detection of antibiotics, proteins, vitamins, and bacteria.[96–100] In public safety applications SPRS is used to monitor traces of explosives, pesticides, heavy metals, and other dangerous substances.[101–105] All measurements share that the concentration is found from a refractive index change with respect to a baseline. The dielectric medium adjacent to the metal surface is usually water with a refractive index $n \approx 1.3$. Besides ATR based sensors, being the most common choice, sensors based on fibers, gratings,

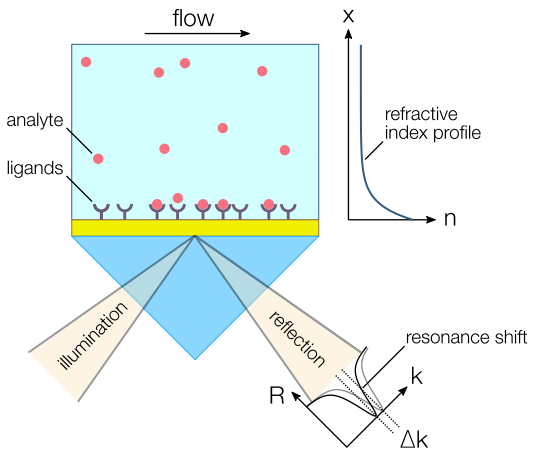

Figure 5.1: The surface of an ATR based surface plasmon resonance sensor is commonly modified with ligands that are able to bind a specific analyte. The locally increased refractive index after binding, perturbs the phase velocity of the surface phase. The corresponding resonance shift is detected either in the angular or in the wavelength spectrum. The shift is used together with the volume flow to calculate the analyte concentration in the medium. A buffer solution is used afterwards to release the analyte and regenerate the sensor.

as well as nano-particles have been used (see Figure 5.2).[80,106] Common to all of these is that they are refractometric measurements. The refractive index is detected indirectly through the analysis of the reflected beam after coupling to a surface plasmon mode. The profile can be a wavelength spectrum or an angular spectrum. In both cases, it is the lack of light rather than the light itself that needs to be measured.

Resolving very small changes of the refractive index is paramount to meeting the high requirements for detection at a molecular level and to competing with other analytic methods. The sensitivity Δn is clearly the key figure for every device. It is usually given in units of RIU (refractive index units) and refers to a bulk refractive index change in the liquid medium. High resolution SPRS requires detecting very weak or fully vanished intensities, as the signal comes from absorption. Whenever low intensities are to be measured, photon quantization needs to be considered. Quantum noise, stemming from the discrete energy portion of the photons, sets an inevitable and impenetrable noise barrier. For a normal photodetector the quantum noise limit is also known as the shot-noise limit.[107] In ATR based SPRS, the accuracy of tracking the resonance cannot

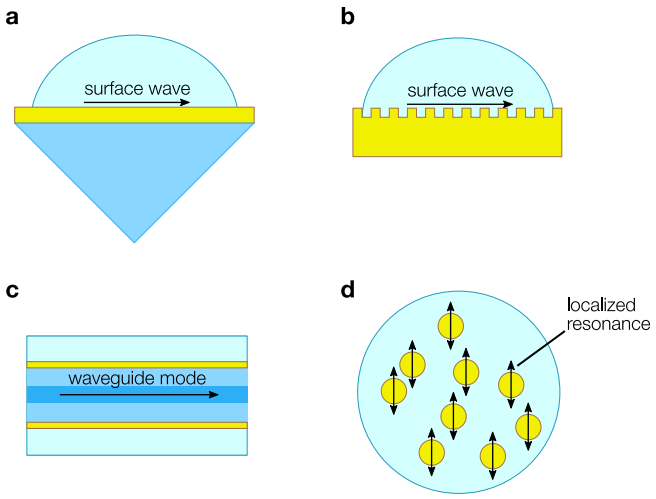

Figure 5.2: The most common types of SPRS sensor configurations. The (a) prism coupled ATR geometry, and (b) grating coupled variants use the change of the excitation angle of a surface wave to detect the refract index. The (c) fiber based SPRS exploits a metal coated fiber that is exposed to the medium that alters the waveguide mode. (d) Localized surface plasmon resonance based sensors use resonant metal nano-particles with an absorption spectrum that is sensitive to the dielectric environment.

be reduced to the detector shot noise in a straightforward manner. Illumination mode, resonance width, coupling condition, and detector arrangement influence both signal and noise. Previous works on resolution limits have concentrated on noise and sensor resolution in a semi-classical concept.[108–110] Obtaining a resolution limit due to photon quantization, however, requires a full quantum optics treatment both of the excitation and detection, which has hitherto been lacking.

The simplest way to circumvent quantum noise is to increase the intensity up to the point where the relative influence is sufficiently small. This optimization is mostly either impractical or has already been fully exhausted. The obvious limitations that prohibit further increase of the illumination power are laser safety, material damage thresholds, heating effects, and photodetector saturation. Improving the efficiency of given technology through a quantum mechanical description of the sensing scheme is, therefore, of great interest.

5.1 The quantum mechanical limit of sensing

Tracking a resonance has similarities with sensing the position and tilt of beams. It has been shown that common detection methods such as quadrant photodiodes have only 64 % efficiency at detecting the position and angle of a Gaussian beam.[111] An optimized homodyne detection with a specially crafted mode profile can be made *optimal*, in the sense that it is able to achieve the highest signal-to-noise ratio allowed by quantum mechanics. The surface wave mode – as excited in the ATR geometry – is unfortunately not of a Gaussian type. The reflected signal is inverted as it contains only the light that has not been matched to the surface wave mode. Light that is coupled to the surface wave gets absorbed along the propagation. It is irretrievably lost and can no longer contribute to the detection. For an optimized detection, a suitable illumination mode needs to be chosen that generates maximum response to resonance shifts. This chapters aims to answer the following questions by employing a full quantum-optical treatment of the ATR detection:

- What is the influence of the illumination profile on the overall detection efficiency?
- How much information on the resonance shift can be obtained with a given number of photons?
- Where is the ultimate detection limit for ATR sensing methods and what illumination is required to achieve it?
- How much more resolution can be gained by employing a homodyne detection scheme with a specially crafted sense mode?
- How can SCTWs contribute to an improved detection sensitivity?

Measuring an optical signal can easily become a challenging task once ultimate precision is demanded. ATR spectroscopy is no exception here, and a typical setup comes with a myriad of noise sources that deteriorate the measurement if not handled properly.

A brief discussion of intensity noise will be given before focusing purely on the quantum noise limit (QNL). The fluctuations of the field and the vacuum are typically quite small compared to the intensity fluctuations of a common light source. Yet, optical detection at the QNL has been shown in many experiments. It can be achieved with low noise

laser sources and appropriate detection techniques. The QNL presents the ultimate noise barrier for any photonic detection.[112,113] If only linear optics are considered, the QNL coincides with the shot-noise limit which is the result of the involved Poissonian photon statistics. Further improvements can be gained through Sub-Poissonian light sources having a lower quantum noise. Representative examples are squeezed light, single photons, and NOON states.[114–116] As all of these require a remarkable increase in experimental complexity, they should be seen as an addition on top of the improvements discussed in the following sections.

5.2 Balanced optical detection

The major source of noise in a setup is the light source used to illuminate the resonance. In contrast to quantum noise, intensity fluctuations of the light source can be circumvented by techniques such as heterodyning or balanced detection.[117,118] In particular, the balanced detection method is a simple, yet very effective technique to suppress noise from the illuminating light source.[119]

Besides optical noise, electrical noise comes into play once the photons are converted to electrons in a device such as a CCD or a photodiode. From that point on, low-noise operational amplifiers and analog-to-digital converters are responsible for efficient detection. It is clear that any experimental setup will require the lowest noise from both the optical and the electrical parts. Low-noise electrical detection is unable to eliminate noise from the optical side and vice versa. The focus of this work will lie solely on the optical side of ATR spectroscopy. Optimizations of the electrical side will be left to the corresponding discipline.

Intensity noise and quantum noise can be distinguished based on how they scale with the number of photons. Intensity noise scales at least linearly with the number of photons n. So, increasing the power will also increase the noise and will leave the overall signal-to-noise ratio (SNR) unchanged at best, and if not, worsen it. Quantum noise originates from the discretization of photons in the beam. Its relative influence is reduced as more photons are involved in the measurement. For a classical monochromatic light source this quantization noise scales with $\sqrt{n}$. On the other hand and unlike in the former case, the SNR benefits from an increased number of photons. Conversely, reducing the

photon count will worsen the SNR to the point where the signal is completely immersed in noise.

The intensity of a light source is impacted by several influences that modulate the momentary power. The frequencies of the noise are spread over orders of magnitude in the frequency domain covering a range from mHz to GHz. Common sources – roughly arranged with respect to their frequency band – are thermal fluctuation, acoustic influences, power supply noise, laser resonator instabilities, and relaxation oscillations. Balanced detection involves measuring the difference between two detectors rather than employing only a single detector. The experiment needs to be constructed as a differential measurement. A zero value of the signal is required to correspond to equal intensities on both detectors. The following comparison will illustrate the advantage of a balanced detection where both the raw signal a and its baseline reference value b are subject to the same intensity fluctuation σ.

	unbalanced detection	balanced detection
intensity noise	σ	σ
signal	$\sigma \cdot a$	$\sigma \cdot a$
reference	b	$\sigma \cdot b$
measured quantity	$s = \sigma \cdot a - b$	$s = \sigma(a - b)$

(5.1)

While intensity noise is present in both an unbalanced and balanced detection scheme, its influence differs significantly. For equal amplitudes of a and b, i.e. the steady state, noise in s is fully vanishing with balanced detection, but completely present with unbalanced detection. But even for a perturbed signal where a and b are slightly different in magnitude, the noise is reduced as its contribution scales with the difference $(a - b)$ rather than a. As a result, employing balanced detection reduces the influence of intensity noise from a zero order effect to a first order effect.

One way to implement balanced detection for ATR sensing is the split detection method that employs two adjacent photodiodes placed such that each records one side of a resonance.[120,121] The subtracted output of both reproduces the angular shift to first order. For improved noise figures, a segmented photodiode is used. It is made from a single waver cut into two sections to obtain two tightly packed photodiodes with matched optoelectronic characteristics. Balancing of the photodiodes can be performed in a

fully analog way through directly subtracting the photocurrents before amplification and subsequent analog-to-digital conversion.

The split detection scheme can be seen as a fundamental detection method that – although not immediately visible – is found in other implementations of ATR sensing. As illustrated in Figure 5.3, any circuit or algorithm that detects the resonance shift from an imaging detector can be expressed as a weighted sum of split detector pairs. The split detection can be thought of as a two pixel array detector, while detectors with more pixels can be treated as interconnected balanced detector assemblies. Looking at Figure

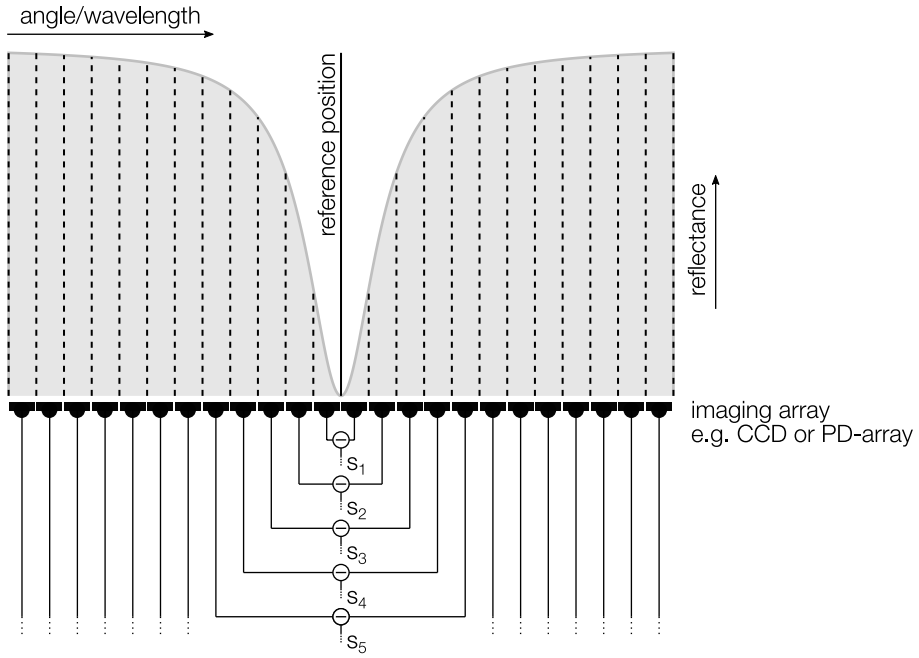

Figure 5.3: An imaging detector resolving resonance shifts can be broken down into a series of balanced detection pairs. Any such scheme can be expressed as being composed of multiple concurrent split detection measurements. The shift Δ – angular or spectral – can be expressed to first order as a weighted sum of the signals s_i: $\Delta = \sum_i w_i s_i$.

5.3, we can see that not all split detector pairs will respond with the same magnitude to a given angular shift Δ. Pixels far off the resonance centroid will see less intensity change than pixels that are located closer to where the slope is steep. On the other hand, the relative error from the detector shot-noise is large close to the center where little intensity is detected, and small for pixels that are far away from the center. This leads us to the question: If not all pixels possess the same SNR for a shift Δ, which pixels

are most effective in the detection process? In the terminology of quantum optics this reads as the question: Which optical modes should be used for excitation and detection, yielding maximum SNR?

In the following paragraphs, the reflectance spectrum carrying the angular resonance will be described by a complex function $r(k,n)$ that holds both the amplitude and phase response of the reflection. This function can be easily calculated numerically with a multilayer transfer matrix algorithm. It is by no means restricted to three-layer systems as the Kretschmann configuration that is used in conventional SPRS devices. The reflectance function $r(k,n)$ depends on the in plane k-vector component of the incident light and the refractive index of the liquid medium.

The illuminating mode – the quantity to be optimized – is characterized by its normalized complex amplitude spectrum $u(k)$ with $\int_{-\infty}^{\infty} |u(k)|^2 \mathrm{d}k = 1$. Combined with the angular response we obtain a mode profile

$$w(k,n) = u(k)\, r(k,n) \tag{5.2}$$

that arrives at the detector. For the response of $r(k,n)$ to changes in n, we employ a first order expansion to describe the small signal response of the system:

$$r(k, n+\delta n) \approx r(k,n) + \delta n \, \frac{\partial r(k,n)}{\partial n}, \quad \delta n \ll 1. \tag{5.3}$$

As we know that the modal propagation constant of an SPP or SCTW mode scales to first order with n, we additionally use

$$\delta n \approx \delta k \underbrace{\frac{\partial n}{\partial k}}_{\approx \frac{n}{k}} \approx \frac{n}{k} \delta k \tag{5.4}$$

to rewrite our problem to depend only on shifts δk:

$$r(k+\delta k) \approx r(k) + \delta k \, \frac{\partial r(k)}{\partial k}, \quad \delta k \ll 1. \tag{5.5}$$

Illuminated with $u(k)$, we get the resulting mode at the detector. It can be separated into two parts

$$w(k+\delta k) \approx w_\mathrm{b}(k) + \delta k \, w_\mathrm{s}(k), \tag{5.6}$$

namely the static background w_b and the signal w_s. The task is now to find an illumination pattern that maximizes the signal contribution and minimizes the background.

For the analysis of the quantum noise contribution to the final sensitivity, we dissect the total electromagnetic field into three modes. This allows us to identify their individual influence on the overall detection efficiency. Each of these modes is considered to be time-harmonic and composed of a weighted integral of plane waves[113]

$$\begin{aligned}
\hat{\mathcal{E}}'_\mathrm{illum}(x,z,t) &:= 2\pi Q \int_{-\infty}^{\infty} \hat{a}(k)\, e^{\mathrm{i}k_x x} e^{\mathrm{i}k_z z} e^{-\mathrm{i}\omega t}\, \mathrm{d}k \\
\hat{\mathcal{E}}'_\mathrm{LO}(x,z,t) &:= 2\pi Q \int_{-\infty}^{\infty} \hat{b}(k)\, e^{\mathrm{i}k_x x} e^{\mathrm{i}k_z z} e^{-\mathrm{i}\omega t}\, \mathrm{d}k \\
\hat{\mathcal{E}}'_\mathrm{vac}(x,z,t) &:= 2\pi Q \int_{-\infty}^{\infty} \hat{c}(k)\, e^{\mathrm{i}k_x x} e^{\mathrm{i}k_z z} e^{-\mathrm{i}\omega t}\, \mathrm{d}k.
\end{aligned} \tag{5.7}$$

Here, $\hat{\mathcal{E}}'_\mathrm{illum}$ is the illuminating mode incident on the resonance. $\hat{\mathcal{E}}'_\mathrm{LO}$ is the local oscillator (LO) mode that is used only for the balanced homodyne detection. $\hat{\mathcal{E}}'_\mathrm{vac}$ represents the vacuum mode that accounts for all losses in the system, in particular the dominating one stemming from the ATR resonance. All scaling factors have been condensed into $Q = \sqrt{\hbar\omega/(16\pi^3\varepsilon_0 cA)}$. The weighting of the plane waves is accounted for by the latter operators $\hat{a}, \hat{b}, \hat{c}$ with the commutating relations

$$\begin{aligned}
\left[\hat{i}(k), \hat{j}^\dagger(k')\right] &= \delta(k-k') \quad && \text{for } \hat{i} = \hat{j}, \quad \hat{i},\hat{j} = \hat{a},\hat{b},\hat{c} \\
\left[\hat{i}(k), \hat{j}^\dagger(k')\right] &= 0 && \text{for } \hat{i} \neq \hat{j}, \quad \hat{i},\hat{j} = \hat{a},\hat{b},\hat{c}.
\end{aligned} \tag{5.8}$$

The creation and annihilation operators of each individual mode are non-commutating, while the orthogonality of the three modes demands that pairs such as $\left[\hat{a}(k), \hat{b}^\dagger(k')\right]$ are commutating.

Describing the problem in k-space instead of position space can simplify the notation significantly. Applying the Fourier transformation and omitting the time harmonic term $e^{-\mathrm{i}\omega t}$, the electrical field operators become

$$\begin{aligned}
\hat{\mathcal{E}}'_\mathrm{illum}(x,z) &\xrightarrow{\mathcal{F}} \hat{\mathcal{E}}_\mathrm{illum}(k) = Q\hat{a}(k) \\
\hat{\mathcal{E}}'_\mathrm{LO}(x,z) &\xrightarrow{\mathcal{F}} \hat{\mathcal{E}}_\mathrm{LO}(k) \;\; = Q\hat{b}(k) \\
\hat{\mathcal{E}}'_\mathrm{vac}(x,z) &\xrightarrow{\mathcal{F}} \hat{\mathcal{E}}_\mathrm{vac}(k) \;\; = Q\hat{c}(k).
\end{aligned} \tag{5.9}$$

As Q is only a scaling factor, we shorten the notation even further by assuming $Q = 1$ henceforth. This needs to be borne in mind when real-world electrical fields are to be calculated.

The angular resonance introduces losses to the illumination mode. Quantum-mechanically, this process is described by $\hat{\mathcal{E}}_{\text{illum}}$ mixing with the vacuum mode $\hat{\mathcal{E}}_{\text{vac}}$. The optical equivalent of a mixer is a beamsplitter with two inputs and two outputs. It has complex reflection and transmission factors $r(k)$ and $t(k)$ that obey

$$\begin{aligned} |r(k)|^2 + |t(k)|^2 &= 1 \\ r^*(k)t(k) - r(k)t^*(k) &= 0 \end{aligned} \tag{5.10}$$

in the absence of any losses inside the beamsplitter. We can then describe the reflected mode as $\hat{\mathcal{E}}_{\text{illum}}$ mixed with $\hat{\mathcal{E}}_{\text{vac}}$ in a beamsplitter-like device:

$$\hat{\mathcal{E}}_{\text{refl}}(k) = r(k)\,\hat{\mathcal{E}}_{\text{illum}}(k) + t(k)\,\hat{\mathcal{E}}_{\text{vac}}(k). \tag{5.11}$$

From here, there are a few more steps to arrive at the desired result. The defined modes need to be populated with photons by making use of the displacement operator. The resulting mode needs to be fed into the detector. Depending on the setup, this can either be a split detection setup or a balanced homodyne detector. In the latter case, the mode is interfered with the local oscillator. In each of the arms of the balanced homodyne detector, an intensity measurement will be performed that demodulates the reflected beam.

The displacement operator acts on the modes and is able to shift their position in the *optical phase space*. A shift using a complex parameter allows preparation of both the amplitude and phase of electrical field, effectively lifting the field from its initial vacuum state at the origin. Applied to $\hat{a}(k)$ and $\hat{b}(k)$, we get

$$\begin{aligned} \hat{D}^\dagger(k,\alpha)\,\hat{a}(k)\,\hat{D}(k,\alpha) &= \hat{a}(k) + \alpha\,u(k) \\ \hat{D}^\dagger(k,\beta)\,\hat{b}(k)\,\hat{D}(k,\beta) &= \hat{b}(k) + \beta\,v(k). \end{aligned} \tag{5.12}$$

The preparation of a state in the optical phase space is illustrated in Figure 5.4. The initial vacuum state together with its uncertainty is displaced by a complex offset. As long as only linear optics are concerned – as in our case – the shape of the noise that encircles the center point remains unchanged.

The displaced mode $\hat{a}$ can now be fed through the ATR resonance where it mixes with the vacuum after which it is forwarded to the detection. Here, we will have to separate our description according to the two detection schemes, namely the split detection (incoherent) and the balanced homodyne detection (coherent).

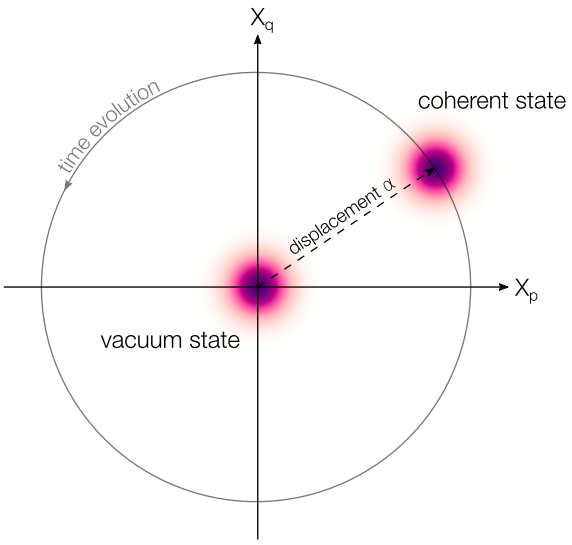

Figure 5.4: The displacement operator is able to prepare a coherent state in both amplitude and phase by shifting the initial vacuum state in the optical phase space. The two axes represent the quadratures of the electrical field. Although not directly related, they can be thought of as momentum p and position q of a quantum mechanical harmonic oscillator. A time evolution leads to a rotation around the origin. The fluctuations of the vacuum state contribute to the uncertainty of the coherent state, which is shown by the Gaussian point spread function around the origin. The uncertainty keeps its circular shape as long as only linear optical effects are considered.

5.3 Incoherent detection

The displaced illumination field $\hat{\mathcal{E}}_{\text{illum}}$ mixes with the ATR resonance thereby modulating the system response onto the incoming illumination:

$$\hat{\mathcal{E}}_{\text{refl}} = \left(r\hat{a} + \alpha r u + t\hat{c}\right). \tag{5.13}$$

An intensity measurement is performed thereafter by two adjacent photodiodes (see Figure 5.5). The intensity operator $\hat{I} = \hat{\mathcal{E}}\hat{\mathcal{E}}^{\dagger}$ is applied yielding

$$\hat{I}_{\text{refl}} = \left(r\hat{a} + \alpha r u + t\hat{c}\right)\left(r^{*}\hat{a}^{\dagger} + \alpha^{*} r^{*} u^{*} + t^{*}\hat{c}^{\dagger}\right). \tag{5.14}$$

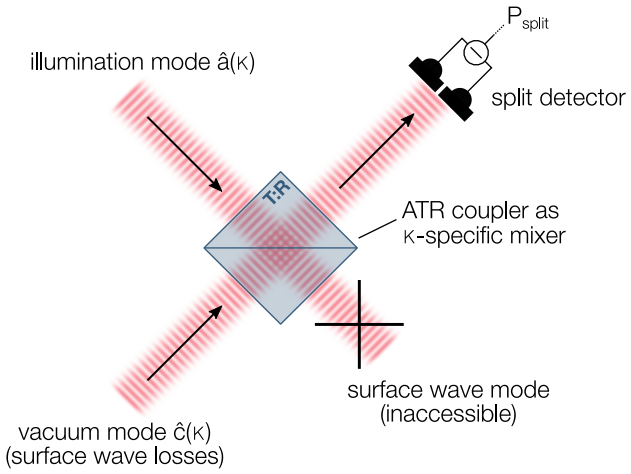

Figure 5.5: For the split detection scheme, a beam splitter model is employed to model the losses occurring upon reflection in the ATR coupler. The beam splitter has a κ-dependent reflection and transmission function that replicates the ATR reflectance curve. It mixes the incident illumination mode with the vacuum mode. The surface wave itself is represented by the mixed mode exiting at the lower beamsplitter output. It remains inaccessible in an ATR experiment, as the mode is both absorbing and evanescent.

The terms are reordered according to how they scale with the amplitude α:

$$\begin{aligned}\hat{I}_{\text{refl}} &= \underbrace{\alpha^2|r|^2|u|^2}_{\hat{I}^{\text{static}}} \\ &+ \underbrace{\alpha|r|^2\left(u^*\hat{a}+u\hat{a}^\dagger\right)+\alpha r^* t\left(u^*\hat{c}+u\hat{c}^\dagger\right)}_{\hat{I}^{\text{fluct}}} \\ &+ \underbrace{|r|^2\hat{a}\hat{a}^\dagger+|t|^2\hat{c}\hat{c}^\dagger+rt^*\left(\hat{a}\hat{c}^\dagger+\hat{c}\hat{a}^\dagger\right)}_{\hat{I}^{\text{vac}}}. \end{aligned} \tag{5.15}$$

Separated like this, we can identify different contributions of noise. The first line scales with α^2 and describes the classical reflection. It is noise-free as it contains no terms that have mixed with either of the vacuum fluctuations $\hat{a}$ or $\hat{c}$. We will refer to this as the static part of the intensity. The second line scales linearly with α. It comprises the mixed component of the illumination and the vacuum modes, describing the quantum noise originating from the discrete nature of photons. In the last line, the vacuum fluctuations and their mixing terms are collected. As they do not scale with the

illumination amplitude, they are present even in the absent of any illumination.

The dependency on κ is removed through integration. Each of the two detectors in the split detection scheme is assumed to detect one half of the k-space. To keep the terms compact we rotate the coordinate system such that the z-axis aligns with the optical axis of the reflected beam. Without loss of generality, the center of the angular ATR resonance is assumed to coincide with the optical axis. The parameterizing k-vector component transversal to the optical axis is denoted by κ henceforth. The static power at the end of the balanced detection becomes

$$\begin{aligned} \hat{P}^{\text{static}} &= \int_0^\infty \hat{I}^{\text{static}} \mathrm{d}\kappa - \int_{-\infty}^0 \hat{I}^{\text{static}} \mathrm{d}\kappa \\ &= \alpha^2 \int_{-\infty}^{\infty} \operatorname{sign}(\kappa)\, |r|^2 |u|^2 \mathrm{d}\kappa. \end{aligned} \tag{5.16}$$

Here, both illumination $|u(\kappa)|$ and resonance $|r(\kappa)|$ have been assumed to be symmetric around the resonance center. This allows the use of the signum function, which simplifies the integral. $\hat{P}^{\text{static}}$ vanishes for an unperturbed balanced detection.

The quantum efficiency η of both detectors has been assumed to be of unity to keep the calculation compact. Quantum efficiencies of 1 are unachievable in reality, however, InGaAs photodiodes with efficiencies $\eta > 0.95$ are readily available.[122] This imperfect detection would be modeled by another loss channel mixing with $\hat{\mathcal{E}}_{\text{refl}}$ before the photoelectrical conversion.

To calculate the ultimate performance of ATR sensing, we are interested in the SNR. The *signal* is found using a perturbed reflectance function $r(\kappa + \delta\kappa) \approx r(\kappa) + \delta\kappa \frac{\partial r(\kappa)}{\partial \kappa}$ with an infinitesimal angular shift $\delta\kappa$

$$\begin{aligned} \mu_{\text{split}} &= \hat{P}_{\text{split}}^{\text{static,pert}} - \hat{P}_{\text{split}}^{\text{static}} \\ &\approx \alpha^2 \int_{-\infty}^{\infty} \operatorname{sign}(\kappa) \left| r + \delta\kappa \frac{\partial r}{\partial \kappa} \right|^2 |u|^2 \mathrm{d}\kappa - P_{\text{split}}^{\text{static}} \\ &\approx \alpha^2 \int_{-\infty}^{\infty} \operatorname{sign}(\kappa) \left(|r|^2 + \delta\kappa\, r \frac{\partial r}{\partial \kappa} + \delta\kappa^2 \left| \frac{\partial r}{\partial \kappa} \right|^2 \right) |u|^2 \mathrm{d}\kappa - \alpha^2 \int_{-\infty}^{\infty} \operatorname{sign}(\kappa)\, |r|^2 |u|^2 \mathrm{d}\kappa \\ &= \delta\kappa\, \alpha^2 \int_{-\infty}^{\infty} \operatorname{sign}(\kappa) \left(r \frac{\partial r^*}{\partial \kappa} + r^* \frac{\partial r}{\partial \kappa} + \delta\kappa \left| \frac{\partial r}{\partial \kappa} \right|^2 \right) |u|^2 \mathrm{d}\kappa \\ &= 2\, \delta\kappa\, \alpha^2 \int_{-\infty}^{\infty} \operatorname{sign}(\kappa)\, |u|^2 \underbrace{\operatorname{Re}\left\{ r^* \frac{\partial r}{\partial \kappa} \right\}}_{\text{demodulation}} \mathrm{d}\kappa. \end{aligned} \tag{5.17}$$

The term scaling with second order in $\delta\kappa$ has been dropped as it is an odd function and evaluates to zero after integration. In the last line, we have marked the *demodulation* term, which extracts the actual signal. The reason for this designation will become evident once we get to the coherent detection.

The *noise* term for the incoherent detection scheme is found from the variance of the fluctuating terms scaling with α as well as the vacuum fluctuations. It requires a rather lengthy calculation which is given in Appendix B.1. The result for σ^2_{split} is quite compact and reads

$$\begin{aligned}\sigma^2_{\text{split}} &= \left\langle 0\middle|(\hat{P}^{\text{fluct}}_{\text{split}} + \hat{P}^{\text{vac}}_{\text{split}})^2\middle|0\right\rangle \\ &= \int_{-\infty}^{\infty} \alpha^2|r|^2|u|^2 + 1\,\mathrm{d}\kappa. \end{aligned} \tag{5.18}$$

It expresses what one would intuitively expect considering detector shot noise: σ^2_{split} depends on the classical reflection coefficient $R = |r|^2$ and the illumination intensity $I = |u|^2$. So, it is proportional to the number of photons that arrive at the detector. In addition, σ^2_{split} comprises the variance of the vacuum fluctuations that are present even in the absence of any reflection.

5.4 Coherent detection

If one aims to exploit information that is encoded solely in the phase of the reflected mode, an incoherent detection scheme is of no use. To extract the optical phase of the reflected beam, it needs to be interfered with a static reference – the local oscillator. In a homodyne detection scheme, the mixing with the LO is performed by a second beamsplitter with a 50:50 T:R ratio (see Figure 5.6). The two detectors A and B, positioned at the output port of the second beamsplitter, are confronted with the superpositioned fields $\hat{\mathcal{E}}_{\text{A}}$ and $\hat{\mathcal{E}}_{\text{B}}$, respectively:

$$\begin{aligned}\hat{\mathcal{E}}_{\text{A}}(\kappa) &= \frac{1}{\sqrt{2}}\left(\hat{\mathcal{E}}_{\text{LO}}(\kappa) + \hat{\mathcal{E}}_{\text{refl}}(\kappa)\right) \\ \hat{\mathcal{E}}_{\text{B}}(\kappa) &= \frac{1}{\sqrt{2}}\left(\hat{\mathcal{E}}_{\text{LO}}(\kappa) - \hat{\mathcal{E}}_{\text{refl}}(\kappa)\right). \end{aligned} \tag{5.19}$$

An intensity measurement is performed for both A and B. The intensity operator $\hat{I} = \hat{\mathcal{E}}\hat{\mathcal{E}}^\dagger$ is applied after displacing the illumination field $\hat{\mathcal{E}}_{\text{illum}}$ and the LO field $\hat{\mathcal{E}}_{\text{LO}}$ by $\alpha u(\kappa)$

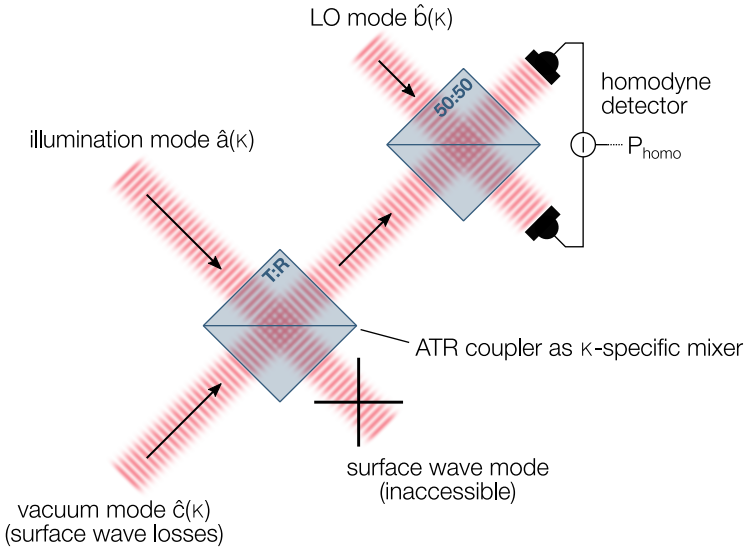

Figure 5.6: The coherent homodyne detection model uses the same κ-dependent beamsplitter as the incoherent split detection to reproduce the surface wave excitation. In addition, a second beam splitter with a 50:50 transmission ratio is used for the homodyne detection. The local oscillator (LO) mode is interfered with the reflected beam and both ports of the mixer are measured and subtracted. The mode amplitude and phase profile of the LO can be used as a mode specific filter during the demodulation. A specially crafted LO mode can make the homodyne output sensitive to certain signals, while immune to others.

and $\beta v(\kappa)$, respectively:

$$\begin{aligned}\hat{I}_\mathrm{A} &= \frac{1}{2}(\hat{b} + \beta v + r\hat{a} + \alpha r u + t\hat{c})(\hat{b}^\dagger + \beta^* v * + r^*\hat{a}^\dagger + \alpha^* r^* u^* + t^*\hat{c}^\dagger) \\ \hat{I}_\mathrm{B} &= \frac{1}{2}(\hat{b} - \beta v - r\hat{a} - \alpha r u - t\hat{c})(\hat{b}^\dagger - \beta^* v * - r^*\hat{a}^\dagger - \alpha^* r^* u^* - t^*\hat{c}^\dagger). \quad (5.20)\end{aligned}$$

The above intensities are still a function of κ and need to be integrated to get the optical power at each detector. The two measurements are subsequently subtracted to obtain the balanced signal of the homodyne detector

$$\begin{aligned}\hat{P}_\mathrm{homo} &= \hat{P}_\mathrm{A} - \hat{P}_\mathrm{B} \\ &= \int_{-\infty}^{\infty} (\hat{I}_A(\kappa) - \hat{I}_B(\kappa))\mathrm{d}\kappa \\ &= \int_{-\infty}^{\infty} (r\hat{b}\hat{a}^\dagger + r^*\hat{a}\hat{b}^\dagger + t\hat{b}\hat{c}^\dagger + t^*\hat{c}\hat{b}^\dagger)\,\mathrm{d}\kappa \quad (5.21)\end{aligned}$$

$$= \int_{-\infty}^{\infty} (r(\hat{b} + \beta v)(\hat{a}^\dagger + \alpha^* u^*) + r^*(\hat{a} + \alpha u)(\hat{b}^\dagger + \beta^* v^*) \tag{5.22}$$

$$+ t(\hat{b} + \beta v)\hat{c}^\dagger + t^* \hat{c}(\hat{b}^\dagger + \beta^* v^*)) \, \mathrm{d}\kappa. \tag{5.23}$$

We can simplify the above equations with the assumption that the LO has a strong field ($\beta \gg \alpha$) and its noise dominates other contributions. In the incoherent case, we could not a priori guarantee that the reflected beam contains any photons. Hence, the vacuum fluctuations need to be taken into account. In the homodyne case, the LO illuminates the detector independently of r and t and we can safely assume its variance is much higher than that of the vacuum fluctuation. In experimental setups, the LO is usually maximized to the point where the detector is not yet saturated and still delivers a distortion free output. Boosting the LO has the effect of amplifying the actual signal. In the following, terms not scaling with β are dropped, yielding

$$\hat{P}_{\mathrm{homo}} \approx \int_{-\infty}^{\infty} (\beta^* v^* r(\hat{a} + \alpha u) + \beta v r^*(\hat{a}^\dagger + \alpha^* u^*) + \beta^* v^* t \hat{c} + \beta v t^* \hat{c}^\dagger) \, \mathrm{d}\kappa. \tag{5.24}$$

As for the incoherent detection, we can now sort the terms and identify static and fluctuating components. $\hat{P}_{\mathrm{vac}}$ has been dropped as its contribution is virtually negligible when an LO is used

$$\begin{aligned} \hat{P}_{\mathrm{homo}} &= \hat{P}_{\mathrm{homo}}^{\mathrm{static}} + \hat{P}_{\mathrm{homo}}^{\mathrm{fluct}} \\ &= 2\alpha\beta \int_{-\infty}^{\infty} \mathrm{Re}\{v^* u r\} \, \mathrm{d}\kappa \\ &+ \int_{-\infty}^{\infty} \big(\beta(v^* r \hat{a} + v r^* \hat{a}^\dagger + v^* t \hat{c} + v t^* \hat{c}^\dagger) + \alpha(u^* r^* \hat{b} + u r \hat{b}^\dagger)\big) \, \mathrm{d}\kappa. \end{aligned} \tag{5.25}$$

We now perturb the system response function $r(\kappa) \to r(\kappa) + \delta\kappa \frac{\partial r}{\partial \kappa}$ to obtain the *signal*

$$\begin{aligned} \mu_{\mathrm{homo}} &= \hat{P}_{\mathrm{homo}}^{\mathrm{static,pert}} - \hat{P}_{\mathrm{homo}}^{\mathrm{static}} \\ &= 2\alpha\beta \int_{-\infty}^{\infty} \mathrm{Re}\left\{v^* u \left(r + \delta\kappa \frac{\partial r}{\partial \kappa}\right)\right\} \mathrm{d}\kappa - 2\alpha\beta \int_{-\infty}^{\infty} \mathrm{Re}\{v^* u r\} \, \mathrm{d}\kappa \\ &= 2\alpha\beta\delta\kappa \int_{-\infty}^{\infty} \underbrace{\mathrm{Re}\left\{v^* u \frac{\partial r}{\partial \kappa}\right\}}_{\text{demodulation}} \mathrm{d}\kappa. \end{aligned} \tag{5.26}$$

Here, the mode of interest $\frac{\partial r}{\partial \kappa}$ is multiplied with the local oscillator and the illumination. This can be interpreted as a demodulation scheme in k-space. The angular resonance modulates a spatial amplitude and phase pattern onto the incident beam. The aim

of the detection is to demodulate the beam and extract the spatial information. The scheme can be seen as a spatial variant of *heterodyning*. Time domain heterodyning uses different frequencies for the carrier wave and the demodulating wave. In our case, both the incident beam and the LO are time-harmonic monochrome waves. The time-domain frequency is exactly the same – hence the name homodyne detection. The spatial frequencies out of which the angular shift signal is reconstructed, however, can be different. The detection scheme uses homodyning in the time-domain and heterodyning in the spatial domain i.e. the k-space. The demodulation of the beam is carried out with the help of v. The goal is to extract the system response that has been encoded into the beam upon reflection in the ATR sensor. Unlike for incoherent detection, the demodulating function i.e. v is under full control and can be chosen to have a specific amplitude and phase profile. The split detection scheme – in contrast – uses the function $u{\cdot}r$ to demodulate the shift. It has a fixed amplitude and phase response resulting from the ATR resonance and cannot be tuned for optimal demodulation.

For the calculation of the *noise*, the reader is again referred to Appendix B.2. The lengthy evaluation of the noise variance yields

$$\begin{aligned}\sigma^2_{\text{homo}} &= \left\langle 0 \middle| (\hat{P}^{\text{fluct}}_{\text{homo}})^2 \middle| 0 \right\rangle \\ &= \beta^2 \,+\, \alpha^2 \int_{-\infty}^{\infty} |u|^2 |r|^2 \,\mathrm{d}\kappa. \end{aligned} \tag{5.27}$$

The result is similar to the variance for split detection, however, it contains the LO noise, which is the only relevant contribution when $\beta \gg \alpha$, as assumed.

5.5 Detection limit

With the signal and noise terms derived for coherent and incoherent detection we are finally in the position to calculate the SNR for both detection schemes and discuss the influence of different illumination patterns on the overall sensitivity

$$\text{SNR}_{\text{split}} = \frac{\mu_{\text{split}}}{\sqrt{\sigma^2_{\text{split}}}} = \frac{2\alpha^2\,\delta\kappa \int \operatorname{sign}(\kappa)\,|u|^2\,\mathrm{Re}\left\{r^* \frac{\partial r}{\partial \kappa}\right\}\mathrm{d}\kappa}{\sqrt{\int \alpha^2 |r|^2 |u|^2 + 1\,\mathrm{d}\kappa}} \tag{5.28}$$

$$\text{SNR}_{\text{homo}} = \frac{\mu_{\text{homo}}}{\sqrt{\sigma^2_{\text{homo}}}} = \frac{2\alpha\beta\,\delta\kappa \int \mathrm{Re}\{v^* u \frac{\partial r}{\partial \kappa}\}\,\mathrm{d}\kappa}{\sqrt{\beta^2 \,+\, \alpha^2 \int |u|^2 |r|^2\,\mathrm{d}\kappa}}. \tag{5.29}$$

These terms could be numerically evaluated with r and $\frac{\partial r}{\partial \kappa}$ found using a multilayer transfer matrix algorithm, as was done in the previous chapter. We will, however, replace r with an analytical function that allows for a deeper understanding of the relevant influences for optimal detection. Following the textbook result originally given by Raether [53], we approximate the ATR resonance using a Lorentzian function

$$r(\kappa) = \frac{\kappa + \frac{i}{2}(1-\zeta)}{\kappa + \frac{i}{2}(1+\zeta)}, \quad \zeta = \frac{k''_{\mathrm{rad}}}{k''_{\mathrm{p}}}, \tag{5.30}$$

where ζ describes the ratio of the intrinsic propagation losses and the radiative losses induced by the prism. It is unity for *critical coupling* when both contributions of losses are equal. Larger and smaller values denote *overcoupled* and *undercoupled* situations, respectively. Furthermore, κ is renormalized to the propagation losses k''_{p} to obtain a dimensionless width of the resonance:

$$\kappa \to \frac{\kappa}{k''_{\mathrm{p}}}. \tag{5.31}$$

The Lorentzian reflectance profile and its derivative are shown in Figure 5.7. The illumination function $u(\kappa)$ acts as a complex weighting function and needs to be chosen to maximize the signal-to-noise ratio. The integrand in the nominator of $\mathrm{SNR}_{\mathrm{split}}$ is $\mathrm{sign}(\kappa) r^* \frac{\partial r}{\partial \kappa}$, weighted by the illumination $|u|$. Looking at Figure 5.8, we can see that the integrand has its maxima at $\pm\frac{1}{\sqrt{2}}$, close to the points of the highest slope. Although the signal experiences the strongest modulation at these points, it is a common misconception[109] to consider these points as optimal for the detection of resonance shifts. This will be evident when taking into account the integrand in the denominator that scales with $|r|$. The largest contribution to $\mathrm{SNR}_{\mathrm{split}}$ therefore comes from the center of the resonance. We can also see that the maximum at the origin is global. The optimal function u is, therefore, a delta function describing a plane wave illumination:

$$u^{\pm}(\kappa) = \delta(\kappa \pm \gamma) \quad \gamma \to 0. \tag{5.32}$$

As the singularity stemming from the pole in $\frac{1}{|r|}$ is located in the center, we shift the plane wave slightly off-center. A small $\pm\gamma$ is added as a positive or negative bias, respectively. The bias allows the singularity to be circumvented and the functions to be handled numerically.

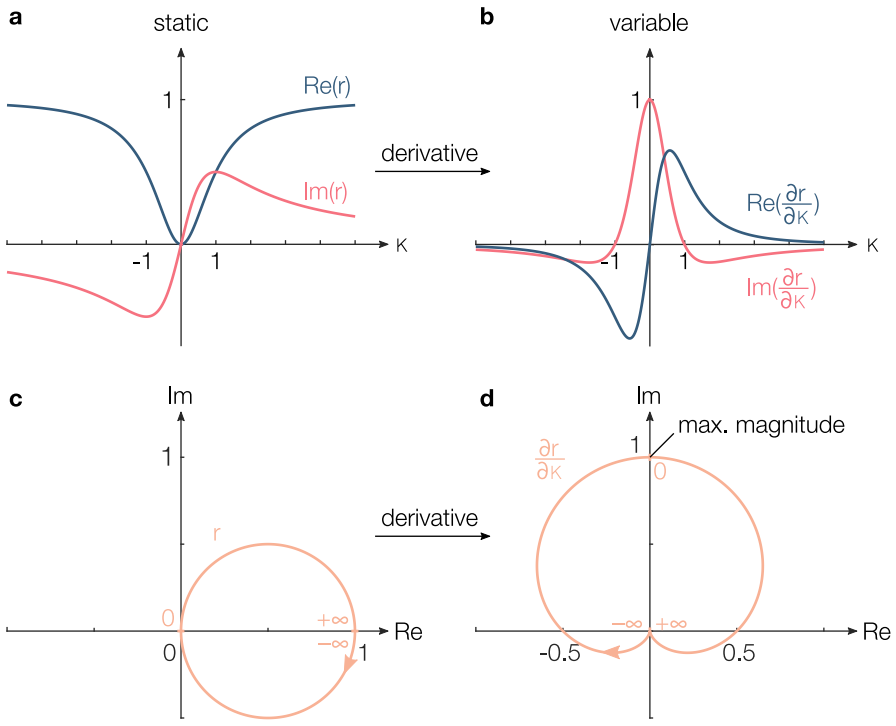

Figure 5.7: The angular resonance is approximated by a Lorentzian profile shown in (a,c). The profile describes a circle in the (c) complex plane that goes through the origin at $\kappa = 0$. The variable part and quantity of interest in ATR based sensing – the derivative with respect to κ – is shown in (b) and (d). The variable part of the ATR response is centered around the imaginary axis in the complex plane. The illuminating mode u applies a weighting function over both the static and the variable part. For optimal detection, u needs to be chosen to maximize the variable contribution and at the same time minimize the static background. The largest signal is found at $\kappa = 0$ where $|\partial_\kappa r(\kappa)|^2$ has its maximum. At the same time, the static part is vanishing.

Another way of removing the singularity would be to take into account the vacuum fluctuations. At this point we have ignored the vacuum fluctuations. If the plane wave is precisely centered at the resonance, no light arrives at the detector, yet the vacuum fluctuations are still present. This is accounted by 1 in the integrand of the noise term in Equation 5.28. Considering the vacuum fluctuations at this point, however, would require setting a number for α to obtain the scale between the photon noise and the vacuum noise. We will ignore the influence of the number of photons for now but will get back to it later.

In analogy to the split detection, we can find the optimal solution for the homodyne

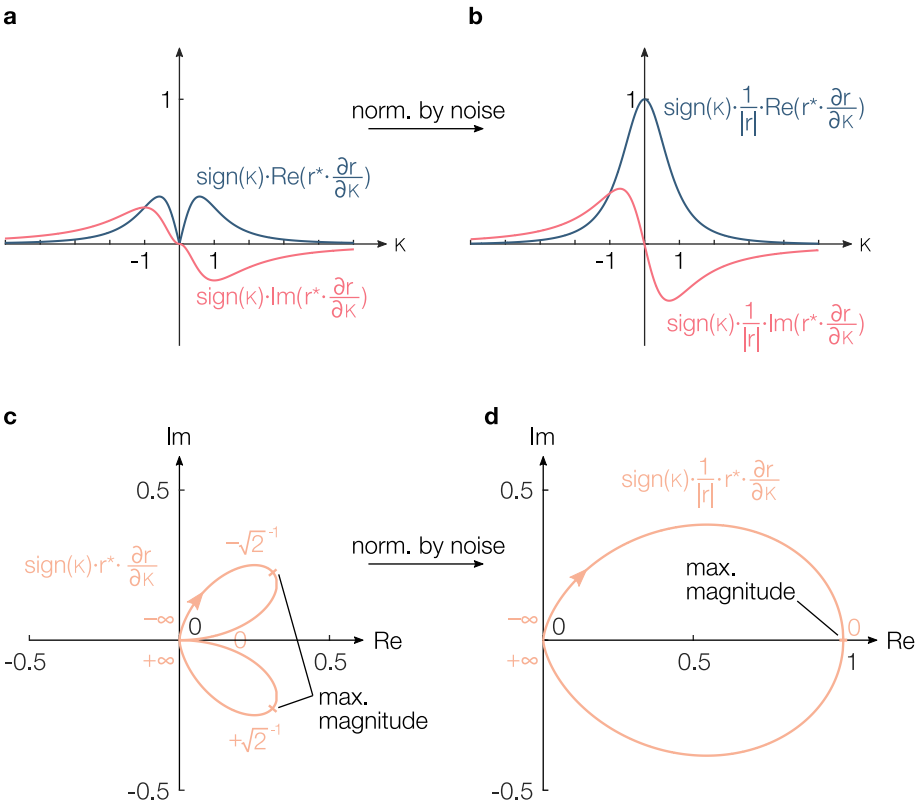

Figure 5.8: (a,c) The signal contribution to the SNR for the split detection scheme. It is zero in the center of the ATR resonance as the reflected beam is fully absorbed. However, the quantum noise vanishes, too. (b,d) The integrand of the signal contribution normalized to the influence of the noise contribution. It can be seen that the highest response is expected to come from illumination of the center region. The points of the highest slope are therefore *not* optimal as often believed.

detection. Two things are different, here. First, not only the illumination mode needs to be chosen, but also the detection mode of the LO. Second, the phase of both these modes has an influence. Additionally, we make use of the property $\beta \gg \alpha$ again to simplify $\mathrm{SNR}_{\mathrm{homo}}$. Although β dominates the noise term, it also serves as a gain to the signal. For sufficiently large photon numbers the influence of β on the overall SNR vanishes

$$\begin{aligned}\mathrm{SNR}_{\mathrm{homo}} &= \frac{2\alpha\beta\,\delta\kappa \int \mathrm{Re}\{v^* u\,\frac{\partial r}{\partial \kappa}\}\,\mathrm{d}\kappa}{\sqrt{\beta^2 + \alpha^2 \int |u|^2 |r|^2\,\mathrm{d}\kappa}} \\ &= \frac{\beta}{\sqrt{\beta^2 + \alpha^2 \int |u|^2 |r|^2\,\mathrm{d}\kappa}} \cdot 2\alpha\,\delta\kappa \int \mathrm{Re}\{v^* u\,\frac{\partial r}{\partial \kappa}\}\,\mathrm{d}\kappa\end{aligned}$$

$$\approx 2\alpha\,\delta\kappa \int \mathrm{Re}\{v^* u\,\frac{\partial r}{\partial \kappa}\}\,\mathrm{d}\kappa. \tag{5.33}$$

Given that the greatest magnitude of $\frac{\partial r}{\partial \kappa}$ (see Figure 5.7) is 1 and both u and v are normalized, we cannot expect the integral to deliver any values larger than we found for the case of split detection.

There is a certain degree of freedom to construct modes that, after integration, will deliver this optimum. If we again use a plane wave illumination $u(\kappa) = \delta(\kappa)$, the integral evaluates to 1 and we obtain the ultimate SNR

$$\mathrm{SNR}_{\max} = 2\alpha\delta\kappa. \tag{5.34}$$

The ultimate detection limit is derived by assuming the SNR to be unity. The smallest resolvable change $\Delta\kappa$ then becomes

$$\Delta\kappa = \frac{1}{2\alpha}. \tag{5.35}$$

which can be transferred into a refractive index change with the help of the relation $\frac{\partial k_\mathrm{p}}{\partial n} \approx \frac{k'_\mathrm{p}}{n}$ and $\kappa = \frac{k}{k''_\mathrm{p}}$. The ultimate limit for refractive index sensing with ATR geometries thereby becomes

$$\frac{\Delta n}{n} \approx \frac{1}{2\alpha}\frac{k''_\mathrm{p}}{k'_\mathrm{p}}. \tag{5.36}$$

The detection limit is inversely proportional to the square root of the number of photons, similar to photodetector shot noise. As the surface wave damping is inversely proportional to the resonance width, we can conclude from $\frac{k''_\mathrm{p}}{k'_\mathrm{p}}$ that increasing the propagation length directly improves the sensitivity.

5.6 Optimal homodyne sense mode

The strength of the homodyne detection scheme lies in its unique way to shape its sensitivity through engineering a suitable LO mode. The advantage will be evident upon comparing the demodulation scheme of split detection and homodyne detection:

split detection			homodyne detection		
$\mathrm{Re}\Big\{$	$\underbrace{\big(u\,r\big)^*}_{\text{LO}}$	$\otimes\ \underbrace{\Big(u\frac{\partial r}{\partial \kappa}\Big)}_{\text{signal of interest}}\ \Big\}$	$\mathrm{Re}\Big\{$	$\underbrace{\big(v\big)^*}_{\text{LO}}$	$\otimes\ \underbrace{\Big(u\frac{\partial r}{\partial \kappa}\Big)}_{\text{signal of interest}}\ \Big\}$

(5.37)

In the split detection scheme, no external local oscillator is present. We can interpret this as a signal that demodulates itself. This makes the detection incoherent as the control over the LO phase is lost. This is detrimental once the signal to be demodulated is not fully real. In the homodyne scheme, the functions u and v allow the phase response to be altered before the real part operator is applied. We therefore have precise control over which part of the angular spectrum is projected to the real or to the imaginary axis of the optical phase space. The output of the balanced detection for both methods is only able to detect the real part. The imaginary part appears as a common mode signal that is eliminated by the photocurrent subtraction. The corresponding quantum noise of the imaginary part is, however, still present and degrades the overall SNR.

The measurement scheme has similarities with quantum state tomography (QST) methods, used to reconstruct the quantum state in the optical phase space. In homodyne based QST, the LO phase is rotated to record all possible projections of the quantum state. With the help of tomographic algorithms, the individual marginal distributions of the phase space are assembled into the reconstructed quantum state. In our particular case, only a single projection containing the full variable part of the quantum state is desired. The static part of the quantum state is of no interest. After mixing with the LO mode, the static contribution is desired to be orthogonal i.e. fully imaginary. The role of the optimized LO mode can be thought of as sorting different parts of the reflected beam into orthogonal states, selecting what to be measured and what to be ignored. An optimal implementation uses u and v such that the LO and the *signal* – the variable part of the ATR response – have opposite phase. This turns the overall response fully to the real axis. We can use a specially crafted LO sense mode v_s

$$\begin{aligned} v_\mathrm{s} &= u\,\frac{\partial r}{\partial \kappa} \\ &\Rightarrow \int \mathrm{Re}\{v^* u\,\frac{\partial r}{\partial \kappa}\}\,\mathrm{d}\kappa = \int \mathrm{Re}\{u^*\frac{\partial r^*}{\partial \kappa}\,u\,\frac{\partial r}{\partial \kappa}\}\,\mathrm{d}\kappa \\ &= \int \left|u\right|^2 \cdot \left|\frac{\partial r}{\partial \kappa}\right|^2 \mathrm{d}\kappa \;\leq 1. \end{aligned} \tag{5.38}$$

Such a configuration is able to extract the full magnitude of $\frac{\partial r}{\partial \kappa}$, weighted by the illumination intensity $|u|^2$. The resulting signal becomes *optimal* for the given illumination pattern.

5.7 Non-ideal illumination

It was shown previously that both split detection and homodyne detection perform optimally under plane wave illumination. Given that the homodyne detection scheme involves a much more sophisticated setup and a stable LO phase, its implementation might not be justified considering the additional experimental efforts. While the plane wave illumination is the simplest one to employ in the theoretical description, its practical implementation is virtually impossible. Experimental setups require a finite focal length beam, which inevitable leads to broadened $k-$spectra. Depending on how much spatial resolution of the sensing surface is demanded, the beam divergence can be anywhere from arc-seconds in high-resolution detectors up to several degrees in surface plasmon resonance microscopy setups.

We now want to compare the split detection scheme with the homodyne detection scheme using the sense mode v_s under a real-valued Gaussian illumination u. The Gaussian beam is technically simple to prepare and its angular spectrum converges against a plane wave for vanishing angular width. In Figure 5.9, detection efficiencies are shown for beams of different angular width and coupling conditions. The detection efficiency is calculated from the integral over the demodulation terms yielding 1 for the optimal case and respectively less for the non-optimal cases with finite focus beams. Homodyne detection is able to provide a high detection efficiency even for beams spreading far over the angular resonance. Split detection, in contrast, can only compete for narrow angular beam widths. The virtues of the homodyne methods are even more pronounced for overcoupled or undercoupled excitation. In particular, overcoupled systems can be detected with an efficiency of more than 0.5 over the whole range. Also evident from the plots is that an undercoupled excitation, having a narrower resonance than the critical excitation, does not enhance the resolution. Figure 5.10 shows the influence of (a) the vacuum fluctuations and (b) the beam offset on the detection efficiency for the split detection. When using the split detection scheme, the total number of photons involved in every measurement matters as soon as quantum noise and vacuum fluctuations get closer. That is when $\alpha^2|r|^2|u|^2 \approx 1$, or in other words, a low number of photons are arriving at the detector. This is a clear drawback of self-demodulating detection. It is not present in homodyne demodulation where a strong demodulating LO can be guaranteed independently of the system response. Figure

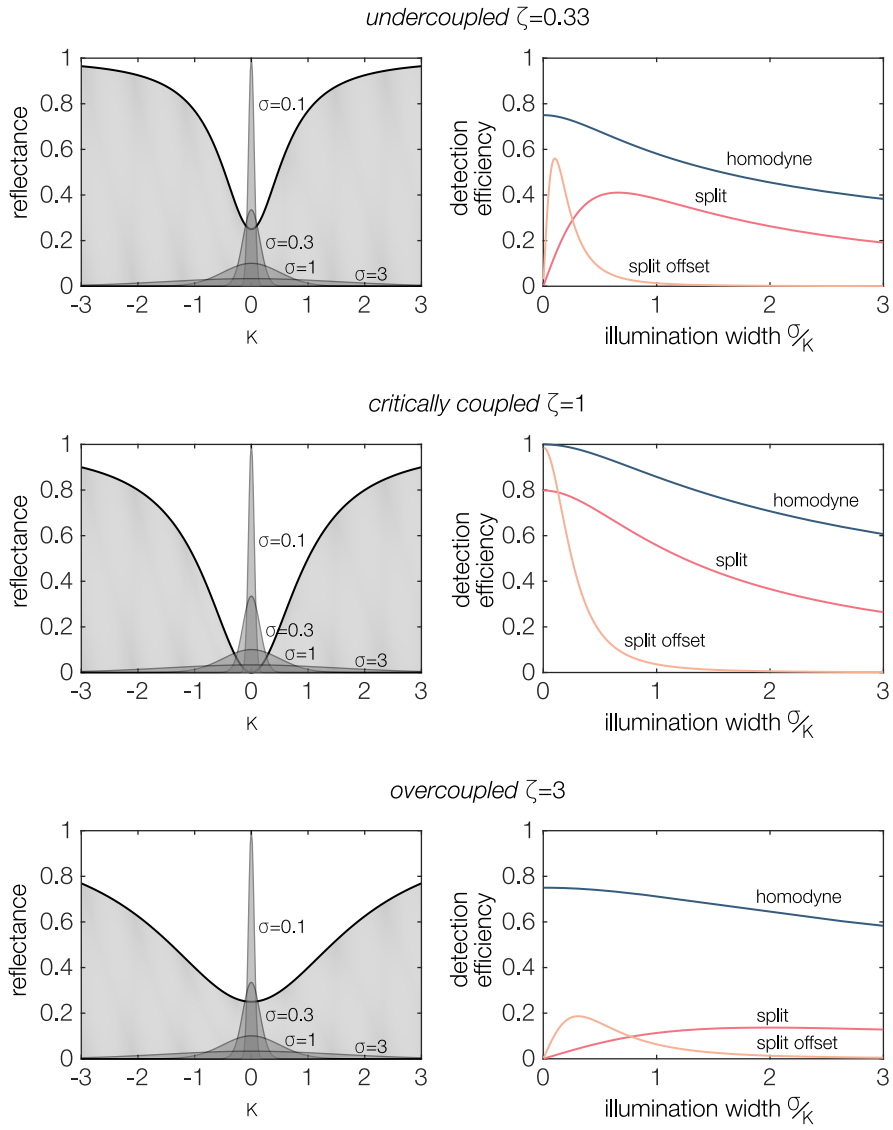

Figure 5.9: Detection efficiency of ATR shifts for Gaussian beam illumination. The highest detection efficiency is found for vanishing angular beam width and critical coupling with $\zeta = 1$ (see Equation 5.30). The homodyne detection using the sense mode v_s provides *optimal* demodulation and is superior to the split detection scheme under all conditions. The split detection scheme reaches only 80 % of the homodyne efficiency for fully centered illumination. Improvement is gained by slightly offsetting the illumination center (in this case 3σ).

5.10 shows the detection efficiency as a function of N, the number of photons coming from the light source. If N is relatively small, not only photon noise but also vacuum

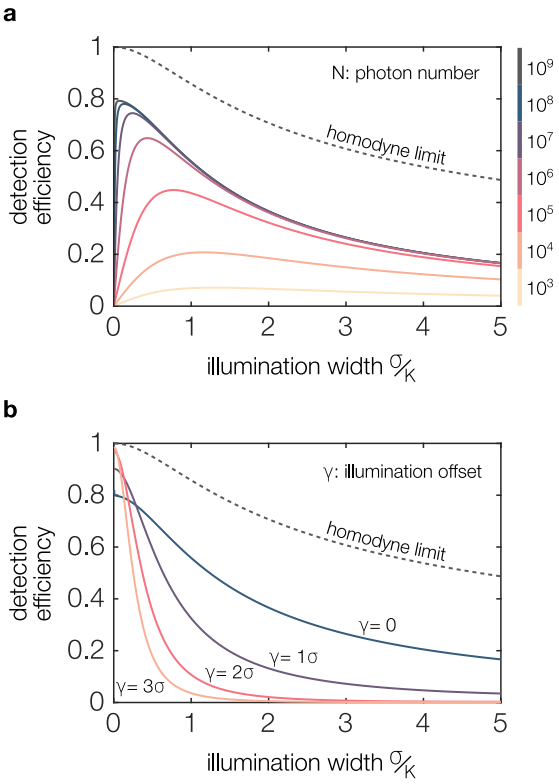

Figure 5.10: (a) Detection efficiency as a function of the total number of illuminating photons. The split detection suffers from a low number of photons that reach the detection in a critically coupled configuration. Using only a few photons will not only lead to a weak SNR, but will degrade the efficiency as the vacuum noise influence becomes significant. The homodyne scheme is shown for reference as optimal detection. (b) Detection efficiency as a function of the beam offset from the center. Using an offset allows the same detection efficiency as with homodyne detection for narrow beam. The offset from the center causes more light to be available for the self-demodulation.

fluctuations are relevant. Note, that these numbers are absolute counts rather than photon rates. A weak illumination with low photon rates can be compensated for by a longer integration time. The actual number N in experiments may differ substantially. A classical ATR setup with a 1 mW red laser emits 10^{12} photons in every 1 ms interval. In contrast, a system that employs an imaging detector such as a CCD or CMOS array is capable of measuring only a fraction of this number due to its limited full-well capacity. The full-well capacity describes the number of photoelectrons that a pixel based detector can accumulate before it saturates. Offsetting the split detection illumination by a small amount may circumvent some of the problems that the self-demodulating detection has.

In particular, it allows split detection the same precision as the homodyne scheme for very narrow illumination widths. The required offset γ depends on the beam width. A large offset works well for plane-wave-like beams, while for wide beams a more centered illumination is preferred.

5.8 Sensor resolution

In the previous section the improvements achieved by optimizing the illumination and detection in ATR based sensors were discussed. It was shown that the ultimate detectable refractive index change scales inversely to the number of involved photons. If this potential is fully utilized, improving the resonance width is the next best option to increase the overall sensitivity. The detection limit Δn is directly proportional to the propagation losses k_{p}'' of the mode that is excited with ATR spectroscopy. Here, SCTWs are an ideal platform for creating waveguides from a broad range of absorbing materials which allows the modal propagation to be custom fitted. Most of today's commercial SPRS systems work with Au thin films coated on prisms or glass slides, used in a Kretschmann configuration.[80] The typical illumination wavelengths lie in the VIS/NIR range with a tendency toward longer wavelengths due to reduced optical losses of Au in the NIR. Improvement for ATR based sensing could come in two ways. First, decreasing the film thickness as far as the material allows. This reduces the modal propagation losses and sharpens the reflectance dip. At the same time, the interaction length between the analyte and the mode is increased. Second, choosing different materials that give additional degrees of freedom for designing new sensing devices. In this case, improved detection efficiency would not necessarily stem from longer propagation lengths but from the improvements in the interaction between sensor and analyte. Using the polymer matrix as a depot for binding agents is one example.[123] Another example is the direct detection of swelling polymer brushes through the accompanied change of the waveguide thickness.

Exploiting the longer propagation length alone can easily improve the theoretical sensitivity by one order of magnitude and more, similar to how it has been shown with Au based LRSPPs.[124] In Figure 5.11 an SCTW based on Au:PNIPAM is compared to a conventional SPP sensor. Here, the same Au:PNIPAM ellipsometry values have been

used as previously. Using core materials with strong permittivity contrast and even thinner cores has the potential for even more sensitivity improvement.

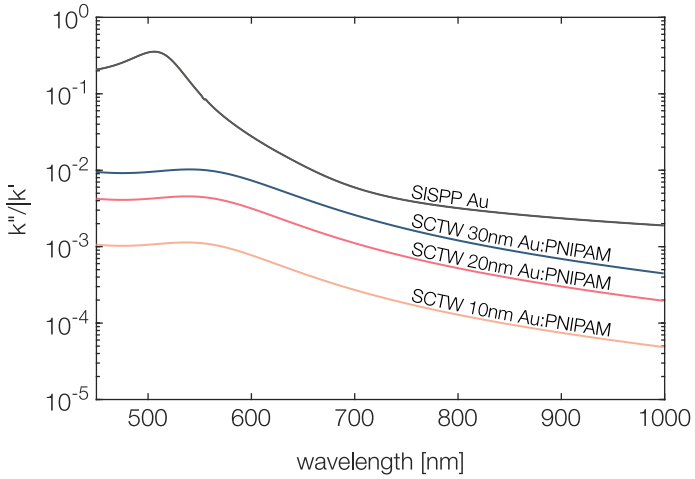

Figure 5.11: Normalized propagation losses as a function of the excitation wavelength. The single interface surface plasmon polariton (SISPP) in gold is the de facto standard for commercial SPRS systems. An SCTW with a 10nm Au:PNIPAM core can outperform this configuration by more than 1.5 orders of magnitude. Reducing the propagation losses has a direct effect on the sensor resolution as the smallest resolvable refractive index change Δn is proportional to the losses (see Equation 5.36).

Using the derived quantum noise sensitivity limit of ATR sensing, the performance of state-of-the-art commercial equipment can be put into perspective. While acquiring the device specifications from the manufacturers of commercial SPRS equipment, it was found that in all but one case the sensitivity was specified as an absolute value rather than specifically for the integration time. The sensitivity limit is, however, a function of the total number of the involved photons rather than the intensity. If we assume a constant illumination power in the device, increasing the integration time would result in higher resolution.

There is a limit that prohibits very long integration times: Thermal instabilities lead to drifts in the baseline of the signal. The refractive index drift, resulting from temperature changes, is in the order of 10^{-5} RIU/K for water. The *baseline drift* is a common specification for SPRS equipment. It usually lies between 10^{-9} and 10^{-8} RIU/s. The limiting influence of the drift scales linearly with the integration time. An optimal integration

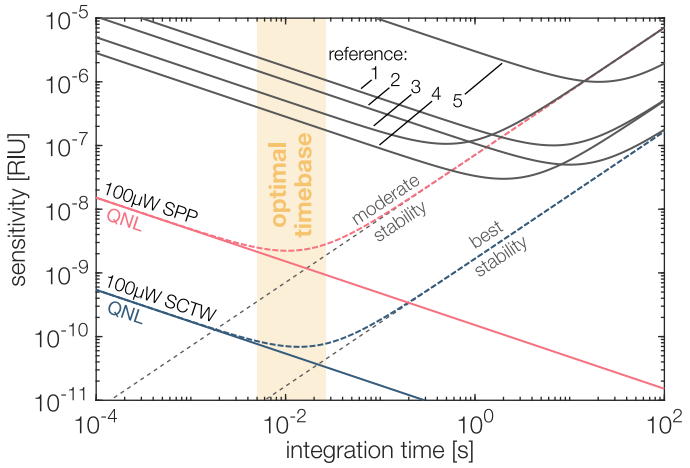

Figure 5.12: Plot showing the bulk refractive index sensitivity limited by quantum noise and thermal stability using a 100 µW laser source with 800 nm wavelength. The thermal stability was derived from manufacturer specifications of commercial SPRS equipment. Using the same data, the sensitivity curves for five devices were estimated as a reference. The estimation assumes thermal instability ($\propto t$) and photon noise ($\propto 1/\sqrt{t}$) for the (1) Biacore X100,[125] (2) Reichert 2SPR,[126] (3) PCbiosensors EVA2.0,[127] (4) Biacore T200,[128] and (5) Bio-Rad XPR36.[129] Optimal sensitivity is expected at the crossing of the QNL with the linear thermal stability. For small time constants, the sensitivity is bound by quantum noise, while for long time constants it is limited by thermal instabilities.

time can be found upon intersecting the QNL and the baseline drift. In Figure 5.12, five commercial devices are compared with the performance of a theoretical quantum noise limited detector with optimal illumination. The given sensitivity – being a function of the integration time – has been estimated from the specified sensitivity limit and the baseline drift. The touted sensitivity is assumed to have been measured with the optimal integration time, i.e. at the point where the detector noise crosses the stability limit. The comparison therefore relies on the marketing departments having done a good job in claiming the outermost sensitivity under ideal conditions.[a] Another assumption is that the sensitivity at the shorter end of the integration time-scale scales with $\frac{1}{\sqrt{N}}$ as the QNL. This is likely not true, yet it serves as a lower bound. In SPRS devices intensity is usually considered as the dominating noise source.[106] Balanced detection schemes

[a] Based on the author's experience this is a safe assumption. The author cannot remember a single case where a scientific instrument has performed significantly better than advertised on paper.

or low noise laser sources are still uncommon. For the theoretical sensitivity curves, a 100 µW coherent light source at 800 nm was assumed to be incident on the sensor. A conventional Au based SPP sensor and hypothetical 20 nm Au:PNIPAM SCTW sensor is shown. Besides the bare quantum noise limited sensitivity, two thermal baseline stability cases are shown. The two stability values have been taken from the best and from the worst stability values of the commercial devices. The figure clearly shows that the detection efficiency of today's SPRS equipment lies far from the QNL. Even the best reference has a sensitivity limit that is two to three orders of magnitude worse than the discussed homodyne or split detection. This significant gap can be explained as most of the sensors using arrayed photodetectors such as CCD or CMOS imagers. The full-well capacity of these detectors is very low compared to large scale photodiodes that can easily withstand tens of µW optical power. The balancing can be easily applied with two photodiodes by subtracting their photocurrents in a purely analog way. An arrayed detector is only able to digitally subtract the values after the analog-to-digital converter (ADC). The smallest differential signal is thereby limited to the ADC resolution which is typically between 10^{-2} and 10^{-5} depending on readout noise and ADC performance.

In an arrayed detection with a wide angular spectrum, the power level must be set conservatively, such that the detector is not saturated or damaged by the off-resonance light. The detector's dynamic range is thereby sacrificed for high intensity off-resonance light that shows little to no modulation on resonance shifts. An optimized detection scheme, as for the discussed homodyne scheme, allows for much higher incident power levels as only a fraction of the incident light is reflected to the detector. The upper limit of the dynamic range can be adjusted such that very weak signals can be detected.

Assuming that the estimated thermal stability limits of commercial equipment have been fully optimized, higher sensitivities require shorter integration times. The optimal timebase lies in the range of 10^1 to 10^2 Hz which is at least one order of magnitude below the calculated sweet spots of the referenced equipment. Increasing the sampling speed has, however, to be taken with a pinch of salt considering other time constants in the system. The reaction of the analyte has a limited reaction speed as it is based on diffusion.[130] On the other hand, a thermal drift is not random as it is quantum noise. It is predictable to a certain degree and can be modeled in order for it to be removed in the subsequent data analysis. Another compensation technique uses a second flow

channel to monitor thermal drifts and bulk refractive index changes.[131] The surface of the reference channel has no binding ligands. Both channels are close to each other so that they are in good thermal contact. It can be concluded that significant room for improvement is available that justifies optimization from a quantum-mechanical point of view.

5.9 Concluding remarks

A full quantum optics treatment of the surface plasmon resonance sensor was missing in literature and has been derived in this chapter. The noise sources for both split detection and homodyne detection have been identified. The SNR for a measurement with a finite number of photons was given. With the help of the SNR the ultimate resolution limit due to the photon quantization was calculated. It scales inversely with the resonance width and the square root of the photon number.

The mode used for illuminating the resonance has a decisive impact on the overall detection efficiency. Here, the optimal function has been found to be a plane wave illumination. Other, more practical illuminations patterns, have a lower efficiency. The homodyne detection scheme has the ability to extract the full absolute signal for any given illumination. A phase inverted LO sense mode that reproduces the mode's derivative is used for optimized demodulation of the signal. It possesses a much higher detection efficiency for beams with a wide angular width. Effective detection is important for applications that require high spatial resolution which is not feasible with narrow resonances. It was furthermore shown that improper coupling leads to a reduction of the SNR. The highest values are found under critical coupling conditions with vanishing intensity at the resonance center. It was deduced that using the incoherent split detection suffers from the problem that very few photons are available for the self-demodulation of the signal. This leads to additional degradation of the efficiency for weak illuminations. The quantum noise limit for SPRS was used to put the sensitivity of frequently used commercial equipment into perspective. It has been questioned in the past whether the theoretical limits of SPRS have already been reached due to illumination intensity noise.[106] It was argued that the ultimate sensitivity of surface plasmon resonance sensors has been reached and further enhancement can only come

through novel surface wave sensors. Balanced detection schemes, such as the proposed ones, can generally overcome intensity noise limits and are able to reach quantum noise limited performance. This benefit has been proven in the prominent experiments done in gravitational wave research.[132] But also much smaller setups have reached quantum noise limited detection with homodyning or heterodyning techniques.[133] In the light of the derived QNL for SRPS, the performance of state-of-the-art devices no longer looks as limited as it has been argued previously. It was demonstrated theoretically that at least two orders of magnitude sensitivity improvement are within reach. This massive gap between the QNL and the real world sensitivity of devices is believed to be a combination of uncompensated intensity noise, weak light sources and the shortcomings of arrayed detectors such as limited dynamic range, noise and full-well capacity.

An optimized balanced detection setup using a large area photodetector will be able to push the sensitivity much closer to the quantum noise limit, which will bring improvement to both spatial resolution and sensitivity. Heterodyne measurements with low intensity noise have been partially demonstrated in phase sensitive SPRS[134–136] or squeezed light SPRS.[137,138] However, the optimizations to the illumination and detection efficiency have been lacking in this context. The superior propagation length together with the broad range of suitable material makes SCTW a promising upgrade to SPRS systems used for molecular detection requiring the highest sensitivity.

Conclusion

This thesis was written with the intention of putting optical losses in waveguiding into perspective and to point out opportunities for the application of new and uncommon waveguide materials. Engineering light-matter interaction or shaping polarization and phase of light is hard to achieve without ever touching losses. A circumstance reflected in the Kramers-Kronig relations, that inextricably link dispersion and absorption. Absorption in waveguides is often considered as an undesirable effect with negative impact on the propagation length. However, with the right cladding, waveguides can in fact be made from highly absorbing materials. Below, each chapter is summarized and findings are presented.

In the first two chapters this counterintuitive concept was discussed thereby showing how material losses can contribute to enhanced propagation. The influence of the permittivity contrast was identified as the driving force behind low-loss waveguiding. Modes in strong absorbers were related to long-range surface plasmon polaritons and TM_0 modes. A continuous mode transformation was demonstrated together with the suggestion that grouping the three modes under symmetric cladding thin-film waveguide modes as a strict distinction seems impossible. Apart from the theoretical existence of modes with lossy materials, the permittivity landscape was visualized to illustrate the range of experimentally accessible values. Figures of merit were computed for all of the common optical materials, serving as a hands-on guide for choosing and comparing thin-film waveguide materials. A combination of SCTW from lossy dielectrics and metals is possible. Impedance matched patching of waveguide sections made from different materials is feasible due to the continuous mode transformation, serving as a path for loss-free coupling.

Chapter 3 was dedicated to spectral white-light interferometry, applied to ATR spec-

troscopy. Extraction of the coupling gap by means of a Fourier transformation was shown. The critical influence of the reflection phase was pointed out. Precompensation of reflection phase effects allows for absolute single digit nanometer accuracy. The method solves substantial experimental challenges that previously existed and often prevented the use of the Otto configuration. It is robust, yet very accurate and permits fine-grained control of the coupling gaps. The method enables broad-band ATR spectroscopy through precise tuning of the coupling. It eliminates the need for a series of samples as required with the Kretschmann configuration.

The concept of lossy waveguides was transferred to nano-engineered materials in chapter 4. The novel materials not only extend the range of nature-given material responses, but can also be made with tunable permittivity and thickness. Here, functionalized nano-particle filled polymer brush surfaces were used to demonstrate waveguiding with symmetric cladding. Despite their unusual and lossy optical properties, low-loss propagation comparable to long-range surface plasmon polaritons was achieved.

In chapter 5, a quantum optics approach was employed to model the sensitivity of ATR based sensing. The ultimate sensitivity limit of both split and homodyne detection was derived. Optimal illumination and detection modes were deduced and discussed. The influence of non-ideal Gaussian illumination was calculated, depicting the superiority of the homodyne detection scheme. The sensitivity limit was estimated for commercially available SPRS equipment. It was made evident that substantial improvements are achievable through optimization of the optical modes and the detector integration time.

At the end of this thesis I would like to venture a look ahead and briefly outline the prospects for this work. Plasmonics has a long history of serving as a launch pad for confined electromagnetic fields at the nanoscale. The strength of noble metals – being stable, inert, and optically linear – is also one of their weakness for the design of functionality. For applications with novel functionality such as quantum technology, materials having sharp and distinct energy levels are preferred over metals that have a quasi-continuous energy band from their free carriers. Therefore, applications of plasmonics usually bundle the metal with other materials such as semiconductors or dyes. Here, an SCTW provides a viable alternative where no metal is needed at all. The optically active or functionalized material itself is used for waveguiding. This, by design, eliminates detrimental emission quenching in the vicinity of metals. It is envisaged

that SCTWs with functionalized surfaces will bring a new generation of optical sensors. Nano-particle filled polymer brush surfaces have already previously been used in a variety of applications as optical sensors. Employing these as waveguides bridges the gap between transmissive sensor designs and commercial ATR-based surface plasmon resonance sensors. Clearly, the next step here is to develop an ATR geometry with a low-index polymer cladding to establish the compatibility with water-based analytes. This will allow the full potential of morphology changes to be harnessed.

Appendix A

Au:PNIPAM synthesis

The polymer brushes used in this work were kindly provided by the group of Regine von Klitzing, in particular Dikran Boyaciyan.

The synthesis of the brush nano-particle hybrid made use of the grafting method through the surface-initiated atom transfer radical polymerization (Si-ATRP). In order to yield polymer brushes, two synthesis steps are needed. As a first step, an initiator has to be attached to the surface as a monolayer. 2-bromo-2-methyl-N-(3-(triethoxysilyl)propyl)propan-amide (BTPAm) was used, which was synthesized according to a literature procedure.[139] Before generating a monolayer of BTPAm onto the SiO_2 substrate, the substrates were etched for 30 min using piranha solution (H_2SO_4/H_2O_2 1:1 v/v %). The freshly cleaned substrates were incubated in a solution of BTPAm and dry toluene (4 µl/10 ml BTPAm/dry Toluene) for 24 h at room temperature to generate a monolayer of BTPAm on the substrate. After completed deposition, the substrates were sonicated in toluene for 20 min, rinsed with Ethanol and dried under a stream of nitrogen.

The second step is the polymerization of PNIPAM at the surface. The synthesis of PNIPAM brushes was adapted from [75]. NIPAM monomer (2 g, 17.67 mmol) was dissolved in 35 ml of ultrapure water/MeOH (1:1 v/v), and the mixture was stirred (500 – 600 rpm) under rigorous nitrogen bubbling for 30 min. Then, PMDETA (150 µl, 0.718 µmol) and CuCl (0.0195 g, 0.197 mmol) were added at once. After stirring for another 30 min under nitrogen bubbling, the BTPAm-coated substrates were added,

and the reaction was carried out for 8 min in a nitrogen atmosphere. Then, the samples were removed quickly, sonicated for 10 min in ultrapure water and in MeOH for another 10 min followed by drying under a stream of nitrogen.

The MDA-capped Au-Nps were attached by incubating the PNIPAM brushes for 24 h in the native Au-Np suspension. After incubation, the samples were taken out, sonicated in ultrapure water for 1 min, and dried under a nitrogen stream.

Appendix B

Noise calculation

B.1 Noise variance for incoherent detection

Calculating the illumination dependent signal-to-noise ratio requires knowledge of the noise variance. For the split detection scheme, the noise power at the balanced detector is

$$\begin{aligned}
\hat{P}^{\text{noise}}_{\text{split}} &= \hat{P}^{\text{vac}}_{\text{split}} + \hat{P}^{\text{fluct}}_{\text{split}} \\
\hat{P}^{\text{vac}}_{\text{split}} &= \int_0^\infty \hat{I}^{\text{vac}}_{\text{refl}} \mathrm{d}\kappa - \int_{-\infty}^0 \hat{I}^{\text{vac}}_{\text{refl}} \mathrm{d}\kappa \\
&= \int_{-\infty}^\infty \operatorname{sign}(\kappa) \Big(|r|^2 \hat{a}\hat{a}^\dagger + |t|^2 \hat{c}\hat{c}^\dagger + rt^* \big(\hat{a}\hat{c}^\dagger + \hat{c}\hat{a}^\dagger\big) \Big) \, \mathrm{d}\kappa \\
\hat{P}^{\text{fluct}}_{\text{split}} &= \int_0^\infty \hat{I}^{\text{fluct}}_{\text{refl}} \mathrm{d}\kappa - \int_{-\infty}^0 \hat{I}^{\text{fluct}}_{\text{refl}} \mathrm{d}\kappa \\
&= \alpha \int_{-\infty}^\infty |r|^2 \big(u_{\text{f}}^* \hat{a} + u_{\text{f}} \hat{a}^\dagger\big) + \big(r^* t u_{\text{f}}^* \hat{c} + r t^* u_{\text{f}} \hat{c}^\dagger\big) \, \mathrm{d}\kappa.
\end{aligned}$$

For both cases, symmetry around the resonance center was assumed to simply merge the two integrals over half of the k–space. In the latter case the flip mode $u_{\text{f}}(\kappa) = \operatorname{sign}(\kappa)\, u(\kappa)$. Before the actual variance $\big\langle 0 \big| (\hat{P}^{\text{fluct}}_{\text{split}} + \hat{P}^{\text{vac}}_{\text{split}})^2 \big| 0 \big\rangle$ is calculated, we introduce the handy quadrature operator that contains the raising and lowering operators as well as a phase factor. It should be noted that the phase is also a function of κ:

$$\begin{aligned}
\hat{X}_a^{\phi(\kappa)}(\kappa) &= e^{\mathrm{i}\phi(\kappa)} \hat{a}(\kappa) + e^{-\mathrm{i}\phi(\kappa)} \hat{a}^\dagger(\kappa) \\
\hat{X}_c^{\theta(\kappa)}(\kappa) &= e^{\mathrm{i}\theta(\kappa)} \hat{c}(\kappa) + e^{-\mathrm{i}\theta(\kappa)} \hat{c}^\dagger(\kappa).
\end{aligned}$$

Orthogonality of the modes demands the commutation relations

$$\begin{aligned}\langle 0|\hat{X}_a^{\phi(\kappa)}(\kappa)\,\hat{X}_a^{\phi(\kappa')}(\kappa')|0\rangle &= \delta(\kappa-\kappa')\\ \langle 0|\hat{X}_c^{\theta(\kappa)}(\kappa)\hat{X}_c^{\theta(\kappa')}(\kappa')|0\rangle &= \delta(\kappa-\kappa')\\ \langle 0|\hat{X}_a^{\phi(\kappa)}(\kappa)\hat{X}_c^{\theta(\kappa')}(\kappa')|0\rangle &= 0.\end{aligned}$$

With the help of the quadrature operators we can rewrite the fluctuating power term in a compressed form

$$\hat{P}_{\text{split}}^{\text{fluct}} = \alpha\int_{-\infty}^{\infty}\left(|r|^2|u|\hat{X}_a^{\phi}+|r||t||u|\hat{X}_c^{\theta}\right)\mathrm{d}\kappa,$$

where the phase angles of the complex coefficient r,t, and u_f have been absorbed by the quadrature operator phases $\phi = \phi_{u_\mathrm{f}}$ and $\theta = -\phi_r + \phi_t - \phi$. The symmetry of u allows to substitute $|u_\mathrm{f}| = |u|$.

The final evaluation of the variance gives four different terms. Although quite lengthy, the calculation can be drastically reduced as follows:

$$\begin{aligned}\sigma^2_{\text{split}} &= \left\langle 0\middle|(\hat{P}_{\text{split}}^{\text{fluct}}+\hat{P}_{\text{split}}^{\text{vac}})^2\middle|0\right\rangle\\ &= \underbrace{\left\langle 0\middle|(\hat{P}_{\text{split}}^{\text{fluct}})^2\middle|0\right\rangle}_{I} + \underbrace{\left\langle 0\middle|(\hat{P}_{\text{split}}^{\text{fluct}}\hat{P}_{\text{split}}^{\text{vac}})\middle|0\right\rangle}_{II} + \underbrace{\left\langle 0\middle|(\hat{P}_{\text{split}}^{\text{vac}}\hat{P}_{\text{split}}^{\text{fluct}})\middle|0\right\rangle}_{III} + \underbrace{\left\langle 0\middle|(\hat{P}_{\text{split}}^{\text{vac}})^2\middle|0\right\rangle}_{IV}\end{aligned}$$

$$\begin{aligned}I &: \left\langle 0\middle|(\hat{P}_{\text{split}}^{\text{fluct}})^2\middle|0\right\rangle\\ &= \alpha^2\iint_{-\infty}^{\infty}\left\langle 0\middle||r(\kappa)||u(\kappa)|\left(|r(\kappa)|\hat{X}_a^{\phi}(\kappa)+|t(\kappa)|\hat{X}_c^{\theta}(\kappa)\right)\right.\\ &\cdot\left.|r(\kappa')||u(\kappa')|\left(|r(\kappa')|\hat{X}_a^{\phi}(\kappa')+|t(\kappa')|\hat{X}_c^{\theta}(\kappa')\right)\middle|0\right\rangle\mathrm{d}\kappa\,\mathrm{d}\kappa'\\ &= \alpha^2\int_{-\infty}^{\infty}|r|^2|u|^2\left(|r|^2\left\langle 0\middle|(\hat{X}_a^{\phi})^2\middle|0\right\rangle+|t|^2\left\langle 0\middle|(\hat{X}_c^{\theta})^2\middle|0\right\rangle\right)\mathrm{d}\kappa\\ &= \alpha^2\int_{-\infty}^{\infty}|r|^2|u|^2\left(|r|^2+|t|^2\right)\mathrm{d}\kappa\\ &= \alpha^2\int_{-\infty}^{\infty}|r|^2|u|^2\,\mathrm{d}\kappa\\ II &: \left\langle 0\middle|(\hat{P}_{\text{split}}^{\text{fluct}}\hat{P}_{\text{split}}^{\text{vac}})\middle|0\right\rangle\\ &= \alpha\iint_{-\infty}^{\infty}\left\langle 0\middle||r(\kappa)||u(\kappa)|\left(|r(\kappa)|\hat{X}_a^{\phi}(\kappa)+|t(\kappa)|\hat{X}_c^{\theta}(\kappa)\right)\right.\end{aligned}$$

$$
\begin{aligned}
&\cdot \left(\operatorname{sign}(\kappa')\left(|r(\kappa')|^2 \hat{a}\hat{a}^\dagger + |t(\kappa')|^2 \hat{c}\hat{c}^\dagger + r(\kappa')t^*(\kappa')(\hat{a}\hat{c}^\dagger + \hat{c}\hat{a}^\dagger)\right)\right)\Big|0\Big\rangle \,\mathrm{d}\kappa \,\mathrm{d}\kappa' \\
&= \alpha \int_{-\infty}^{\infty} \Big\langle 0\Big| |r(\kappa)||u(\kappa)|\Big(|r(\kappa)|(e^{\mathrm{i}\phi}\hat{a}(\kappa) + e^{-\mathrm{i}\phi}\hat{a}^\dagger(\kappa)) + |t(\kappa)|(e^{\mathrm{i}\theta}\hat{c}(\kappa) + e^{-\mathrm{i}\theta}\hat{c}^\dagger(\kappa))\Big) \\
&\cdot \left(\operatorname{sign}(\kappa')\left(|r(\kappa)|^2 \hat{a}\hat{a}^\dagger + |t(\kappa)|^2 \hat{c}\hat{c}^\dagger + r(\kappa)t^*(\kappa)(\hat{a}\hat{c}^\dagger + \hat{c}\hat{a}^\dagger)\right)\right)\Big|0\Big\rangle \,\mathrm{d}\kappa \\
&= 0
\end{aligned}
$$

$$
III : \left\langle 0\middle|(\hat{P}^{\mathrm{vac}}_{\mathrm{split}}\hat{P}^{\mathrm{fluct}}_{\mathrm{split}})\middle|0\right\rangle = 0
$$

$$
\begin{aligned}
IV &: \left\langle 0\middle|(\hat{P}^{\mathrm{vac}}_{\mathrm{split}})^2\middle|0\right\rangle \\
&= \iint_{-\infty}^{\infty} \Big\langle 0\Big|\Big(\operatorname{sign}(\kappa)\left(|r(\kappa)|^2 \hat{a}\hat{a}^\dagger + |t(\kappa)|^2 \hat{c}\hat{c}^\dagger + r(\kappa)t^*(\kappa)(\hat{a}\hat{c}^\dagger + \hat{c}\hat{a}^\dagger)\right)\Big) \\
&\cdot \left(\operatorname{sign}(\kappa')\left(|r(\kappa')|^2 \hat{a}\hat{a}^\dagger + |t(\kappa')|^2 \hat{c}\hat{c}^\dagger + r(\kappa')t^*(\kappa')(\hat{a}\hat{c}^\dagger + \hat{c}\hat{a}^\dagger)\right)\right)\Big|0\Big\rangle \,\mathrm{d}\kappa \,\mathrm{d}\kappa' \\
&= \int_{-\infty}^{\infty} \Big\langle 0\Big|\Big(\operatorname{sign}(\kappa)^2\left(|r(\kappa)|^2 \hat{a}\hat{a}^\dagger + |t(\kappa)|^2 \hat{c}\hat{c}^\dagger + r(\kappa)t^*(\kappa)(\hat{a}\hat{c}^\dagger + \hat{c}\hat{a}^\dagger)\right)\Big) \\
&\cdot \left(|r(\kappa)|^2 \hat{a}\hat{a}^\dagger + |t(\kappa)|^2 \hat{c}\hat{c}^\dagger + r(\kappa)t^*(\kappa)(\hat{a}\hat{c}^\dagger + \hat{c}\hat{a}^\dagger)\right)\Big|0\Big\rangle \,\mathrm{d}\kappa \\
&= \int_{-\infty}^{\infty} |r(\kappa)|^4 \left\langle 0\middle|\hat{a}\hat{a}\hat{a}^\dagger\hat{a}^\dagger\middle|0\right\rangle + 2|r(\kappa)|^2|t(\kappa)|^2 \left\langle 0\middle|\hat{a}\hat{c}\hat{a}^\dagger\hat{c}^\dagger\middle|0\right\rangle + |t(\kappa)|^4 \left\langle 0\middle|\hat{c}\hat{c}\hat{c}^\dagger\hat{c}^\dagger\middle|0\right\rangle \\
&+ r(\kappa)t^*(\kappa)r^*(\kappa)t(\kappa)\left\langle 0\middle|(\hat{a}\hat{c}^\dagger + \hat{c}\hat{a}^\dagger)^2\middle|0\right\rangle \mathrm{d}\kappa \\
&= \int_{-\infty}^{\infty} |r(\kappa)|^4 + 2|r(\kappa)|^2|t(\kappa)|^2 + |t(\kappa)|^4 \mathrm{d}\kappa \\
&= \int_{-\infty}^{\infty} (|r(\kappa)|^2 + |t(\kappa)|^2)^2 \mathrm{d}\kappa \\
&= \int_{-\infty}^{\infty} 1 \,\mathrm{d}\kappa.
\end{aligned}
$$

Here, the first term was reduced exploiting the orthogonality of the quadrature operators. The second and third terms evaluate to zero as both contain only uneven numbers of concatenated ladder operators. The fourth term IV represents the vacuum fluctuation and is independent of r, t, and u. It may seem to diverge given that it is integrated over κ. However, for a finite number of photons – spread all modes in the $k-$space – α also needs to be normalized by $\int_{-\infty}^{\infty} 1 \,\mathrm{d}\kappa$. Therefore, $|\alpha|^2$ is proportional to the overall number of photons in the system.

$$
\begin{aligned}
\sigma^2_{\mathrm{split}} &= \left\langle 0\middle|(\hat{P}^{\mathrm{fluct}}_{\mathrm{split}} + \hat{P}^{\mathrm{vac}}_{\mathrm{split}})^2\middle|0\right\rangle \\
&= \int_{-\infty}^{\infty} \alpha^2 |r|^2 |u|^2 + 1 \,\mathrm{d}\kappa
\end{aligned}
$$

B.2 Noise variance for coherent detection

Calculation of the noise variances for the coherent detection is similar to the incoherent case. As the local oscillator is assumed to possess a large number of photons at any time, the vacuum fluctuations $\hat{P}^{\text{vac}}_{\text{homo}}$ can be safely ignored:

$$
\begin{aligned}
\sigma^2_{\text{homo}} &= \left\langle 0 \middle| (\hat{P}^{\text{fluct}}_{\text{homo}})^2 \middle| 0 \right\rangle \\
&= \int_{-\infty}^{\infty} \int_{-\infty}^{\infty} \Big\langle 0 \Big| \Big(\beta |v(\kappa)||r(\kappa)| \hat{X}_a^{\phi'}(\kappa) \\
&+ \beta |v(\kappa)||t(\kappa)| \hat{X}_c^{\theta'}(\kappa) + \alpha |u(\kappa)||r(\kappa)| \hat{X}_b^{\varphi'}(\kappa) \Big) \\
&\cdot \Big(\beta |v(\kappa')||r(\kappa')| \hat{X}_a^{\phi'}(\kappa') + \beta |v(\kappa')||t(\kappa')| \hat{X}_c^{\theta'}(\kappa') \\
&+ \alpha |u(\kappa')||r(\kappa')| \hat{X}_b^{\varphi'}(\kappa') \Big) \Big| 0 \Big\rangle \, \mathrm{d}\kappa \, \mathrm{d}\kappa' \\
&= \int_{-\infty}^{\infty} \Big(\beta^2 |v|^2 |r|^2 \left\langle 0 \middle| (\hat{X}_a^{\phi'})^2 \middle| 0 \right\rangle + \beta^2 |v|^2 |t|^2 \left\langle 0 \middle| (\hat{X}_c^{\theta'})^2 \middle| 0 \right\rangle \\
&+ \alpha^2 |u|^2 |r|^2 \left\langle 0 \middle| (\hat{X}_b^{\varphi'})^2 \middle| 0 \right\rangle \Big) \, \mathrm{d}\kappa \\
&= \int_{-\infty}^{\infty} \Big(\beta^2 |v|^2 |r|^2 + \beta^2 |v|^2 |t|^2 + \alpha^2 |u|^2 |r|^2 \Big) \, \mathrm{d}\kappa \\
&= \int_{-\infty}^{\infty} \Big(\beta^2 |v|^2 (|r|^2 + |t|^2) + \alpha^2 |u|^2 |r|^2 \Big) \, \mathrm{d}\kappa \\
&= \beta^2 \int_{-\infty}^{\infty} |v|^2 \, \mathrm{d}\kappa \; + \; \alpha^2 \int_{-\infty}^{\infty} |u|^2 |r|^2 \, \mathrm{d}\kappa \\
&= \beta^2 \; + \; \alpha^2 \int_{-\infty}^{\infty} |u|^2 |r|^2 \, \mathrm{d}\kappa .
\end{aligned}
$$

The largest noise variance comes clearly from the LO and is present independently of the system response r, as expected.

Appendix C

Ellipsometry Data

The following datasets have been used throughout the manuscript.

Ag K. M. McPeak, S. V. Jayanti, S. J. P. Kress, S. Meyer, S. Iotti, A. Rossinelli, and D. J. Norris. Plasmonic films can easily be better: Rules and recipes, *ACS Photonics* **2**, 326-333 (2015)

Al K. M. McPeak, S. V. Jayanti, S. J. P. Kress, S. Meyer, S. Iotti, A. Rossinelli, and D. J. Norris. Plasmonic films can easily be better: Rules and recipes, *ACS Photonics* **2**, 326-333 (2015)

AlSb S. Zollner, C. Lin, E. Schönherr, A. Böhringer, M. Cardona. The dielectric function of AlSb from 1.4 to 5.8 eV determined by spectroscopic ellipsometry, *J. Appl. Phys.* **66**, 383-387 (1989)

Au K. M. McPeak, S. V. Jayanti, S. J. P. Kress, S. Meyer, S. Iotti, A. Rossinelli, and D. J. Norris. Plasmonic films can easily be better: Rules and recipes, *ACS Photonics* **2**, 326-333 (2015) *Note: if not stated otherwise, Au permittivity values from this work were used*

Au S. Babar and J. H. Weaver. Optical constants of Cu, Ag, and Au revisited, *Appl. Opt.* **54**, 477-481 (2015)

Au H.-J. Hagemann, W. Gudat, and C. Kunz. Optical constants from the far infrared to the x-ray region: Mg, Al, Cu, Ag, Au, Bi, C, and Al_2O_3, *J. Opt. Soc. Am.* **65**, 742-744 (1975)

Au P. B. Johnson and R. W. Christy. Optical Constants of the Noble Metals, *Phys. Rev. B* **6**, 4370-4379 (1972)

Au R. L. Olmon, B. Slovick, T. W. Johnson, D. Shelton, S.-H. Oh, G. D. Boreman, and M. B. Raschke. Optical dielectric function of gold, *Phys Rev. B* **86**, 235147 (2012)

Au A. D. Rakić, A. B. Djurišic, J. M. Elazar, and M. L. Majewski. Optical properties of metallic films for vertical-cavity optoelectronic devices, *Appl. Opt.* **37**, 5271-5283 (1998)

B_4C J. I. Larruquert, A. P. Pérez-Marín, S. García-Cortés, L. Rodríguez-de Marcos, J. A. Aznàrez, J. A. Méndez. Self-consistent optical constants of sputter-deposited B_4C thin films, *J. Opt. Soc. Am. A* **29**, 117-123 (2012)

Be A. D. Rakić, A. B. Djurišic, J. M. Elazar, and M. L. Majewski. Optical properties of metallic films for vertical-cavity optoelectronic devices, *Appl. Opt.* **37**, 5271-5283 (1998)

Bi H.-J. Hagemann, W. Gudat, and C. Kunz. Optical constants from the far infrared to the x-ray region: Mg, Al, Cu, Ag, Au, Bi, C, and Al_2O_3, *J. Opt. Soc. Am.* **65**, 742-744 (1975)

$BiFeO_3$ A. Kumar, R. C. Rai, N. J. Podraza, S. Denev, M. Ramirez, Y.-H. Chu, L. W. Martin, J. Ihlefeld, T. Heeg, J. Schubert, D. G. Schlom, J. Orenstein, R. Ramesh, R. W. Collins, J. L. Musfeldt and V. Gopalan. Linear and nonlinear optical properties of $BiFeO_3$, *Appl. Phys. Lett.* **92**, 121915 (2008)

C H.-J. Hagemann, W. Gudat, and C. Kunz. Optical constants from the far infrared to the x-ray region: Mg, Al, Cu, Ag, Au, Bi, C, and Al_2O_3, *J. Opt. Soc. Am.* **65**, 742-744 (1975)

C J. I. Larruquert, L. V. Rodríguez-de Marcos, J. A. Méndez, P. J. Martin, A. Bendavid. High reflectance ta-C coatings in the extreme ultraviolet, *Opt. Exp.* **21**, 27537-27549 (2013)

C J. W. Weber, V. E. Calado and M. C. M. van de Sanden. Optical constants of graphene measured by spectroscopic ellipsometry, *Appl. Phys. Lett.* **97**, 091904 (2010)

C S. Kedenburg, M. Vieweg, T. Gissibl, and H. Giessen. Linear refractive index and absorption measurements of nonlinear optical liquids in the visible and near-infrared spectral region, *Opt. Mat. Express* **2**, 1588-1611 (2012)

CdS R. E. Treharne, A. Seymour-Pierce, K. Durose, K. Hutchings, S. Roncallo, D. Lane, Optical design and fabrication of fully sputtered CdTe/CdS solar cells, *J. Phys: Conf. Ser.* **286**, 012038, (2011)

CdTe R. E. Treharne, A. Seymour-Pierce, K. Durose, K. Hutchings, S. Roncallo, D. Lane, Optical design and fabrication of fully sputtered CdTe/CdS solar cells, *J. Phys: Conf. Ser.* **286**, 012038, (2011)

$CH_3NH_3PBi_3$ L. J. Phillips, A. M. Rashed, R. E. Treharne, J. Kay, P. Yates, I. Mitrovic, A. Weerakkody, S. Hall, K. Durose, Dispersion relation data for methylammonium lead triiodide perovskite deposited on a (100) silicon wafer using a two-step vapour-phase reaction processs, *Data in Brief* **5**, 926-928 (2015)

Co P. B. Johnson and R. W. Christy. Optical constants of transition metals: Ti, V, Cr, Mn, Fe, Co, Ni, and Pd, *Phys. Rev. B* **9**, 5056-5070 (1974)

$CoSi_2$ Sopra S.A., Optical database. http://www.sspectra.com/sopra.html

Cr A. D. Rakić, A. B. Djurišic, J. M. Elazar, and M. L. Majewski. Optical properties of metallic films for vertical-cavity optoelectronic devices, *Appl. Opt.* **37**, 5271-5283 (1998)

Cu K. M. McPeak, S. V. Jayanti, S. J. P. Kress, S. Meyer, S. Iotti, A. Rossinelli, and D. J. Norris. Plasmonic films can easily be better: Rules and recipes, *ACS Photonics* **2**, 326-333 (2015)

Fe P. B. Johnson and R. W. Christy. Optical constants of transition metals: Ti, V, Cr, Mn, Fe, Co, Ni, and Pd, *Phys. Rev. B* **9**, 5056-5070 (1974)

GaAs G.E. Jellison Jr. Optical functions of GaAs, GaP, and Ge determined by two-channel polarization modulation ellipsometry, *Opt. Mat.* **1**, 151-160 (1992)

GaN T. Kawashima, H. Yoshikawa, S. Adachi. Optical properties of hexagonal GaN, *J. Appl. Phys.* **82**, 3528-3535 (1997)

GaInP M. Schubert, V. Gottschalch, C. M. Herzinger, H. Yao, P. G. Snyder and J. A. Woollam. Optical constants of $Ga_xIn_{1-x}P$ lattice matched to GaAs, *J. Appl. Phys.* 77, 3416 (1995)

GaP D.E. Aspnes and A. A. Studna. Dielectric functions and optical parameters of Si, Ge, GaP, GaAs, GaSb, InP, InAs, and InSb from 1.5 to 6.0 eV, *Phys. Rev. B* **27**, 985-1009 (1983)

GaSb R. Ferrini, M. Patrini, and S. Franchi. Optical functions from 0.02 to 6 eV of $Al_xGa_{1-x}Sb$/GaSb epitaxial layers, *J. Appl Phys.* **84**, 4517-4524 (1998)

Ge G.E. Jellison Jr. Optical functions of GaAs, GaP, and Ge determined by two-channel polarization modulation ellipsometry, *Opt. Mat.* **1**, 151-160 (1992)

HfN G. V. Naik, J. Kim, and A. Boltasseva. Oxides and nitrides as alternative plasmonic materials in the optical range, *Optical Materials Express* **1.6**, 1090-1099 (2011)

Hg T. Inagaki, E. T. Arakawa, and M. W. Williams. Optical properties of liquid mercury, *Phys. Rev. B* **23**, 5246-5262 (1981)

In_2O_3-SnO_2 R. J. Moerland and J. P. Hoogenboom. Subnanometer-accuracy optical distance ruler based on fluorescence quenching by transparent conductors, *Optica* **3**, 112-117 (2016)

In A. I. Golovashkin, I. S. Levchenko, G. P. Motulevich, A .A. Shubin. The optical properties of niobium, *Sov. Phys. JETP* **24**, 1093-1099 (1967)

InAs D. E. Aspnes and A. A. Studna. Dielectric functions and optical parameters of Si, Ge, GaP, GaAs, GaSb, InP, InAs, and InSb from 1.5 to 6.0 eV, *Phys. Rev. B* **27**, 985-1009 (1983)

InP D. E. Aspnes and A. A. Studna. Dielectric functions and optical parameters of Si, Ge, GaP, GaAs, GaSb, InP, InAs, and InSb from 1.5 to 6.0 eV, *Phys. Rev. B* **27**, 985-1009 (1983)

Ir M. A. Ordal, R. J. Bell, R. W. Alexander, L. A. Newquist, M. R. Querry. Optical properties of Al, Fe, Ti, Ta, W, and Mo at submillimeter wavelengths, *Appl. Opt.* **27**, 1203-1209 (1988)

Li T. Inagaki et al. Optical properties of solid Na and Li between 0.6 and 3.8 eV, *Phs. Rev. B* **13**, 2305-313 (1976)

Lu S. García-Cortés, L. Rodríguez-de Marcos, J. I. Larruquert, J. A. Aznàrez, J. A. Méndez, L. Poletto, F. Frassetto, A. M. Malvezzi, A. Giglia, N. Mahne and S. Nannarone. Transmittance and optical constants of Lu films in the 3-1800 eV spectral range, *J. Appl. Phys.* **108**, 063514 (2010)

Mg H.-J. Hagemann, W. Gudat, and C. Kunz. Optical constants from the far infrared to the x-ray region: Mg, Al, Cu, Ag, Au, Bi, C, and Al_2O_3, *J. Opt. Soc. Am.* **65**, 742-744 (1975)

Mn P. B. Johnson and R. W. Christy. Optical constants of transition metals: Ti, V, Cr, Mn, Fe, Co, Ni, and Pd, *Phys. Rev. B* **9**, 5056-5070 (1974)

Mo Sopra S.A., Optical database. http://www.sspectra.com/sopra.html

MoO_3 M. Vos, B. Macco, N. F. W. Thissen, A. A. Bol, W. M. M. Kessels. Atomic layer deposition of molybdenum oxide from $(N^tBu)_2(NMe_2)_2Mo$ and O_2 plasma, *J. Vac. Scia. Technol. A* **34**, 01A103 (2015)

MoS_2 Y. Li, A. Chernikov, X. Zhang, A. Rigosi, H. M. Hill, A. M. van der Zande, D. A. Chenet, E. Shih, J. Hone, and T. F. Heinz: Measurement of the optical dielectric function of monolayer transition-metal dichalcogenides: MoS2, MoSe2, WS2, and WSe2, *Physical Review B* **90.20**, 205422 (2014).

MoS C. Yim, M. O'Brien, N. McEvoy, S. Winters, I. Mirza, J. G. Lunney and G. S. Duesberg. Investigation of the optical properties of MoS_2 thin films using spectroscopic ellipsometry, *Appl. Phys. Let.* **104**, 103114 (2014)

$MoSe_2$ Y. Li, A. Chernikov, X. Zhang, A. Rigosi, H. M. Hill, A. M. van der Zande, D. A. Chenet, E. Shih, J. Hone, and T. F. Heinz: Measurement of the optical dielectric function of monolayer transition-metal dichalcogenides: MoS2, MoSe2, WS2, and WSe2, *Physical Review B* **90.20**, 205422 (2014).

$MoTe_2$ A. R. Beal and H. P. Huges. Kramers-Kronig analysis of the reflectivity spectra of 2H-MoS_2, 2H-$MoSe_2$, and 2H-$MoTe_2$, *J. Phys. C* **12**, 881 (2001)

Na T. Inagaki et al. Optical properties of solid Na and Li between 0.6 and 3.8 eV, *Phs. Rev. B* **13**, 2305-2313 (1976)

Nb A. I. Golovashkin, I. E. Leksina, G. P. Motulevich and A. A. Shubin. The optical properties of niobium, *Sov. Phys. JETP* **29**, 27-34 (1969)

Ni A. D. Rakić, A. B. Djurišic, J. M. Elazar, and M. L. Majewski. Optical properties of metallic films for vertical-cavity optoelectronic devices, *Appl. Opt.* **37**, 5271-5283 (1998)

Pb A. I. Golovashkin and G. P. Motulevich. Optical properties of lead in the visible and infrared spectral ranges, *Sov. Phys. JETP* **26**, 881-887 (1968)

PbSe S. Adachi. *Optical Constants of Crystalline and Amorphous Semiconductors*, Springer, New York (1999)

Pd A. D. Rakić, A. B. Djurišic, J. M. Elazar, and M. L. Majewski. Optical properties of metallic films for vertical-cavity optoelectronic devices, *Appl. Opt.* **37**, 5271-5283 (1998)

Pt A. D. Rakić, A. B. Djurišic, J. M. Elazar, and M. L. Majewski. Optical properties of metallic films for vertical-cavity optoelectronic devices, *Appl. Opt.* **37**, 5271-5283 (1998)

Rh J. H. Weaver, C. G. Olson, and D. W. Lynch. Optical investigation of the electronic structure of bulk Rh and Ir, *Phys. Rev. B* **15**, 4115 (1977)

Si M. A. Green and M. J. Keevers. Optical properties of intrinsic silicon at 300 K, *Progress in photovoltaics* **3**, 189-192 (1995)

SiC J. I. Larruquert, A. P. Pérez-Marín, S. García-Cortés, L. Rodríguez-de Marcos, J. A. Aznàrez, J. A. Méndez. Self-consistent optical constants of SiC thin films, *J. Opt. Soc. Am. A* **28**, 2340-2345 (2011)

SiO G. Hass and C. D. Salzberg. Optical properties of silicon monoxide in the wavelength region from 0.24 to 14.0 microns, *J. Opt. Soc. Am.* **44**, 181-183 (1954)

SiO_2 I. H. Malitson. Interspecimen comparison of the refractive index of fused silica, *J. Opt. Soc. Am.* **55**, 1205-1208 (1965)

Sn A. I. Golovashkin and G. P. Motulevich. Optical and electrical properties of tin, *Sov. Phys. JETP* **19**, 310-317 (1964)

Ta M. A. Ordal, R. J. Bell, R. W. Alexander, L. A. Newquist, M. R. Querry. Optical properties of Al, Fe, Ti, Ta, W, and Mo at submillimeter wavelengths, *Appl. Opt.* **27**, 1203-1209 (1988)

TaN G. V. Naik, J. Kim, and A. Boltasseva. Oxides and nitrides as alternative plasmonic materials in the optical range, *Optical Materials Express* **1.6**, 1090-1099 (2011)

Ta_2O_5 L. Gao, F. Lemarchand, and M. Lequime. Exploitation of multiple incidences spectrometric measurements for thin film reverse engineering, *Opt. Express* **20**, 15734-15751 (2012)

Ti A. D. Rakić, A. B. Djurišic, J. M. Elazar, and M. L. Majewski. Optical properties of metallic films for vertical-cavity optoelectronic devices, *Appl. Opt.* **37**, 5271-5283 (1998)

TiN G. V. Naik, J. Kim, and A. Boltasseva. Oxides and nitrides as alternative plasmonic materials in the optical range, *Optical Materials Express* **1.6**, 1090-1099 (2011)

W A. D. Rakić, A. B. Djurišic, J. M. Elazar, and M. L. Majewski. Optical properties of metallic films for vertical-cavity optoelectronic devices, *Appl. Opt.* **37**, 5271-5283 (1998)

VO_2 A. Joushaghani. Micro-and nano-scale optoelectronic devices using vanadium dioxide. Diss. (2014)

WS_2 Y. Li, A. Chernikov, X. Zhang, A. Rigosi, H. M. Hill, A. M. van der Zande, D. A. Chenet, E. Shih, J. Hone, and T. F. Heinz: Measurement of the optical dielectric function of monolayer transition-metal dichalcogenides: MoS2, MoSe2, WS2, and WSe2, *Physical Review B* **90.20**, 205422 (2014).

WSe_2 Y. Li, A. Chernikov, X. Zhang, A. Rigosi, H. M. Hill, A. M. van der Zande, D. A. Chenet, E. Shih, J. Hone, and T. F. Heinz: Measurement of the optical dielectric function of monolayer transition-metal dichalcogenides: MoS2, MoSe2, WS2, and WSe2, *Physical Review B* **90.20**, 205422 (2014).

ZrN G. V. Naik, J. Kim, and A. Boltasseva. Oxides and nitrides as alternative plasmonic materials in the optical range, *Optical Materials Express* **1.6**, 1090-1099 (2011)

Publications and conference contributions

Publications related to this work

Pufahl, K.; Boyaciyan, D.; Heckmann, J.; Grosse, N. B.; von Klitzing, R.; Woggon, U. Symmetric Cladding Thin Film Waveguides: From Lossy Media to Disordered Nanostructures.*ACS Photonics* **2018**, *5*, 5110–5118, DOI: 10.1021/acsphotonics.8b01533

Pufahl, K.; Passler, N. C.; Grosse, N. B.; Wolf, M.; Woggon, U.; Paarmann, A. Controlling nanoscale air-gaps for critically coupled surface polaritons by means of non-invasive white-light interferometry.*Appl. Phys. Lett.* **2018**, *113*, 161103, DOI: 10.1063/1.5049230

Pufahl, K.; Grosse, N. B.; Woggon, U. K. The quantum noise limit of surface-plasmon resonance sensing *in preparation*

Other publications

Grosse, N. B.; Franz, P.; Heckmann, J.; Pufahl, K.; Woggon, U. Utilizing strongly absorbing materials for low-loss surface-wave nonlinear optics.*Phys. Rev. A* **2018**, *97*, 43844, DOI: 10.1103/PhysRevA.97.043844

Heckmann, J.; Pufahl, K.; Franz, P.; Grosse, N. B.; Li, X.; Woggon, U. Plasmon-enhanced

nonlinear yield in the Otto and Kretschmann configurations.*Phys. Rev. B* **2018**, *98*, 115415, DOI: 10.1103/PhysRevB.98.115415

Conference contributions

Pufahl, K.; Heckmann, J.; Woggon, U. K.; **Grosse, N. B.** In *Proc. META'16*, 2016, pp 1266–1267

Heckmann, J.; **Pufahl, K.**; Grosse, N. B.; Sipe, J. E.; Woggon, U. K. In *Proc. META'16*, 2016, pp 1411–1412

Pufahl, K.; Kesal, D.; Franz, P.; Heckmann, J.; Grosse, N. B.; Christau, S.; Lehmann, M.; von Klitzing, R.; Woggon, U. K. In, NNN TELECOM workshop Le Mans: 2017

Franz, P.; Heckmann, J.; **Pufahl, K.**; Grosse, N. B.; Woggon, U. K. In *Nonlinear Opt.* 2017, NF2A.3, DOI: 10.1364/NLO.2017.NF2A.3

Pufahl, K.; Boyaciyan, D.; Heckmann, J.; Franz, P.; Grosse, N. B.; von Klitzing, R.; **Woggon, U. K.** In *Front. Opt. / Laser Sci.* Optical Society of America: 2018, FW6E.2

References

[1] Ye, W. N.; Xiong, Y. Review of silicon photonics: History and recent advances.*J. Mod. Opt.* **2013**, *60*, 1299–1320, DOI: 10.1080/09500340.2013.839836.

[2] Sorger, V. J.; Oulton, R. F.; Ma, R. M.; Zhang, X. Toward integrated plasmonic circuits.*MRS Bull.* **2012**, *37*, 728–738, DOI: 10.1557/mrs.2012.170.

[3] Fang, Y.; Sun, M. Nanoplasmonic waveguides: Towards applications in integrated nanophotonic circuits.*Light Sci. Appl.* **2015**, *4*, DOI: 10.1038/lsa.2015.67.

[4] Davis, T. J.; Gómez, D. E.; Roberts, A. Plasmonic circuits for manipulating optical information.*Nanophotonics* **2017**, *6*, 543–559, DOI: 10.1515/nanoph-2016-0131.

[5] Charbonneau, R.; Lahoud, N.; Mattiussi, G.; Berini, P. Demonstration of integrated optics elements based on long-ranging surface plasmon polaritons.*Opt. Express* **2005**, *13*, 977–984, DOI: 10.1364/OPEX.13.000977.

[6] Yu, N.; Genevet, P.; Kats, M. a.; Aieta, F.; Tetienne, J.-P.; Capasso, F.; Gaburro, Z. Light Propagation with Phase Discontinuities Reflection and Refraction.*Science (80-.).* **2011**, *334*, 333–337, DOI: 10.1126/science.1210713.

[7] Meinzer, N.; Barnes, W. L.; Hooper, I. R. Plasmonic meta-atoms and metasurfaces.*Nat. Photonics* **2014**, *8*, 889–898, DOI: 10.1038/nphoton.2014.247.

[8] Yu, N.; Capasso, F. Flat optics with designer metasurfaces.*Nat. Mater.* **2014**, *13*, 139–150, DOI: 10.1038/nmat3839.

[9] Hsiao, H.; Chu, C. H.; Tsai, D. P. Fundamentals and Applications of Metasurfaces.*Small Methods* **2017**, *1*, 1600064, DOI: 10.1002/smtd.201600064.

[10] Khurgin, J. B. Ultimate Limit of Field Confinement by Surface Plasmon Polaritons.*Faraday Discuss.* **2015**, *178*, 109–122, DOI: 10.1039/C4FD00193A.

[11] Kovacs, G. J. Surface Polariton in the ART Angular Spectra of a Thin Iron Film Bounded by Dielectric Layers.*J. Opt. Soc. Am.* **1978**, *68*, 1325–1332.

[12] Yang, F.; Sambles, J. R.; Bradberry, G. W. Long-range coupled surface exciton polaritons.*Phys. Rev. Lett.* **1990**, *64*, 559–562, DOI: 10.1103/PhysRevLett.64.559.

[13] Yang, F.; Sambles, J. R.; Bradberry, G. W. Long-range surface modes supported by thin films.*Phys. Rev. B* **1991**, *44*, 5855–5872, DOI: 10.1103/PhysRevB.44.5855.

[14] Takabayashi, M.; Shiba, H.; Haraguchi, M.; Fukui, M. Studies on Surface Polaritons in Ultrathin Films Sandwiched by Identical Dielectrics.*J. Phys. Soc. Japan* **1992**, *61*, 2550–2556, DOI: 10.1143/JPSJ.61.2550.

[15] Takabayashi, M.; Haraguchi, M.; Fukui, M. Propagation length of guided waves in lossy Si film sandwiched by identical dielectrics.*J. Opt. Soc. Am. B* **1995**, *12*, 2406–2411, DOI: 10.1364/JOSAB.12.002406.

[16] Giannini, V.; Zhang, Y.; Forcales, M.; Rivas, J. G. Long-range surface polaritons in ultra-thin films of silicon.*Opt. Express* **2008**, *16*, 19674–19685, DOI: 10.1364/OE.16.019674.

[17] Arnold, C.; Zhang, Y.; Rivas, J. G. Long range surface polaritons supported by lossy thin films.*Appl. Phys. Lett.* **2010**, *96*, DOI: 10.1063/1.3364938.

[18] Pufahl, K.; Boyaciyan, D.; Heckmann, J.; Grosse, N. B.; von Klitzing, R.; Woggon, U. Symmetric Cladding Thin Film Waveguides: From Lossy Media to Disordered Nanostructures.*ACS Photonics* **2018**, *5*, 5110–5118, DOI: 10.1021/acsphotonics.8b01533.

[19] Pufahl, K.; Passler, N. C.; Grosse, N. B.; Wolf, M.; Woggon, U.; Paarmann, A. Controlling nanoscale air-gaps for critically coupled surface polaritons by means of non-invasive white-light interferometry.*Appl. Phys. Lett.* **2018**, *113*, 161103, DOI: 10.1063/1.5049230.

[20] Maier, S. A., *Plasmonics: Fundamentals and applications*, 2007, DOI: 10.1007/0-387-37825-1.

[21] Sarid, D.; Challener, W., *Modern Introduction to Surface Plasmons*, 2013, DOI: 10.1017/cbo9781139194846.

[22] Fontana, E.; Pantell, R. H. Characterization of multilayer rough surfaces by use of surface-plasmon spectroscopy.*Phys. Rev. B* **1988**, *37*, 3164–3182, DOI: 10.1103/PhysRevB.37.3164.

[23] Gollub, J. N.; Smith, D. R.; Vier, D. C.; Perram, T.; Mock, J. J. Experimental characterization of magnetic surface plasmons on metamaterials with negative permeability.*Phys. Rev. B* **2005**, *71*, 195402, DOI: 10.1103/PhysRevB.71.195402.

[24] D'yakonov, M. I. New type of electromagnetic wave propagating at an interface.*Sov. Phys. JETP* **1988**, *67*, 714–716.

[25] Yeh, P.; Yariv, A.; Hong, C.-S. Electromagnetic propagation in periodic stratified media I General theory*.*J. Opt. Soc. Am.* **1977**, DOI: 10.1364/JOSA.67.000423.

[26] Polo, J. A.; Lakhtakia, A. Surface electromagnetic waves: A review.*Laser Photonics Rev.* **2011**, *5*, 234–246, DOI: 10.1002/lpor.200900050.

[27] Takayama, O.; Bogdanov, A. A.; Lavrinenko, A. V. Photonic surface waves on metamaterial interfaces.*J. Phys. Condens. Matter* **2017**, *29*, DOI: 10.1088/1361-648X/aa8bdd.

[28] Uller, K. Beiträge zur Theorie der elektromagnetischen Strahlung, Ph.D. Thesis, 1903.

[29] Zenneck, J. Über die Fortpflanzung ebener elektromagnetischer Wellen längs einer ebenen Leiterfläche und ihre Beziehung zur drahtlosen Telegraphie.*Ann. Phys.* **1907**, *328*, 846–866, DOI: 10.1002/andp.19073281003.

[30] Sommerfeld, A. Über die Ausbreitung der Wellen in der drahtlosen Telegraphie.*Ann. Phys.* **1909**, *333*, 665–736, DOI: 10.1002/andp.19093330402.

[31] Kahan, T.; Eckart, G. On the Electromagnetic Surface Wave of Sommerfeld.*Phys. Rev.* **1949**, *76*, 406–410, DOI: 10.1103/PhysRev.76.406.

[32] Bashkuev, Y. B.; Khaptanov, V. B.; Dembelov, M. G. Experimental proof of the existence of a surface electromagnetic wave.*Tech. Phys. Lett.* **2010**, *36*, 136–139, DOI: 10.1134/S1063785010020136.

[33] Kukushkin, A. V. A technique for solving the wave equation and prospects for physical applications arising therefrom.*Physics-Uspekhi* **1993**, *36*, 81.

[34] Kukushkin, A. V.; Rukhadze, A. A.; Rukhadze, K. Z. On the existence conditions for a fast surface wave.*Physics-Uspekhi* **2012**, *55*, 1124.

[35] Wait, J. R. The Ancient and Modern History of EM Ground-Wave Propagation.*IEEE Antennas Propag. Mag.* **1998**, *40*, 7–24, DOI: 10.1109/74.735961.

[36] Jangal, F.; Bourey, N.; Darces, M.; Issac, F.; Hélier, M. Observation of Zenneck-Like Waves over a Metasurface Designed for Launching HF Radar Surface Wave.*Int. J. Antennas Propag.* **2016**, DOI: 10.1155/2016/6184959.

[37] Norton, K. A. Propagation of Radio Waves over a Plane Earth.*Nature* **1935**, *135*, 954–955, DOI: 10.1038/135954a0.

[38] Collin, R. E. Hertzian dipole radiating over a lossy earth or sea: Some early and late 20th-century controversies.*IEEE Antennas Propag. Mag.* **2004**, DOI: 10.1109/MAP.2004.1305535.

[39] Burke, J. J.; Stegeman, G. I.; Tamir, T. Surface-polariton-like waves guided by thin, lossy metal films.*Phys. Rev. B* **1986**, *33*, 5186–5201, DOI: 10.1103/PhysRevB.33.5186.

[40] Berini, P. Long-range surface plasmon polaritons.*Adv. Opt. Photon.* **2009**, *1*, 484–588, DOI: 10.1364/AOP.1.000484.

[41] Crook, R. J.; Yang, F.; Sambles, J. R. Long-range optical modes supported by a strongly absorbing thin organic film.*J. Opt. Soc. Am. B* **1993**, *10*, 237, DOI: 10.1364/josab.10.000237.

[42] Crook, R. J.; Yang, F.; Sambles, J. R. An investigation of p- and s-polarized long-range optical modes supported by a strongly absorbing normal uniaxial thin organic film.*J. Mod. Opt.* **1993**, *40*, 243–253, DOI: 10.1080/09500349314550261.

[43] Yang, F.; Sambles, J. R. Determination of the optical permittivity and thickness of absorbing films using long range modes.*J. Mod. Opt.* **1997**, *44*, 1155–1163, DOI: 10.1080/09500349708230726.

[44] Jackson, J. D., *Classical Electrodynamics*, 3rd, 1999, DOI: 10.1119/1.19136.

[45] Polyanskiy, M. N. Refractive index database, https://refractiveindex.info.

[46] Filmetrics Inc. Refractive Index Database, https://www.filmetrics.com/refractive-index-database.

[47] Sopra S.A. Optical database, http://www.sspectra.com/sopra.html.

[48] Berini, P. Figures of merit for surface plasmon waveguides.*Opt. Express* **2006**, *14*, 13030, DOI: 10.1364/OE.14.013030.

[49] McPeak, K. M.; Jayanti, S. V.; Kress, S. J. P.; Meyer, S.; Iotti, S.; Rossinelli, A.; Norris, D. J. Plasmonic films can easily be better: Rules and recipes.*ACS Photonics* **2015**, *2*, 326–333, DOI: 10.1021/ph5004237.

[50] Grosse, N. B.; Franz, P.; Heckmann, J.; Pufahl, K.; Woggon, U. Utilizing strongly absorbing materials for low-loss surface-wave nonlinear optics.*Phys. Rev. A* **2018**, *97*, 43844, DOI: 10.1103/PhysRevA.97.043844.

[51] Grigorenko, A. N.; Nikitin, P. I.; Kabashin, A. V. Phase jumps and interferometric surface plasmon resonance imaging.*Appl. Phys. Lett.* **1999**, *75*, 3917–3919, DOI: 10.1063/1.125493.

[52] Stegeman, G. I.; Wallis, R. F.; Maradudin, A. A. Excitation of surface polaritons by end-fire coupling.*Opt. Lett.* **1983**, *8*, 386, DOI: 10.1364/ol.8.000386.

[53] Raether, H. Surface plasmons on smooth and rough surfaces and on gratings.*Springer-Verlag, New York* **1988**, *111*, 136, DOI: 10.1007/BFb0048317.

[54] Keilmann, F. Surface-polariton propagation for scanning near-field optical microscopy application.*J. Microsc.* **1999**, *194*, 567–570, DOI: 10.1046/j.1365-2818.1999.00495.x.

[55] Otto, A. Excitation of nonradiative surface plasma waves in silver by the method of frustrated total reflection.*Zeitschrift für Phys.* **1968**, *216*, 398–410, DOI: 10.1007/BF01391532.

[56] Bergh, R. A.; Kotler, G.; Shaw, H. J. Single-mode fibre optic directional coupler.*Electron. Lett.* **1980**, *16*, 260–261, DOI: 10.1049/el:19800191.

[57] Betzig, E.; Lewis, A.; Harootunian, A.; Isaacson, M.; Kratschmer, E. Near Field Scanning Optical Microscopy (NSOM): Development and Biophysical Applications.*Biophys. J.* **1986**, *49*, 269–279, DOI: https://doi.org/10.1016/S0006-3495(86)83640-2.

[58] Axelrod, D. Cell-substrate contacts illuminated by total internal reflection fluorescence.*J. Cell Biol.* **1981**, *89*, 141–145, DOI: 10.1083/jcb.89.1.141.

[59] Kretschmann, E.; Raether, H. Radiative decay of nonradiative plasmons excited by light.*Z. Naturforsch. A* **1968**, *23*, 2135–2136.

[60] Wood, E.; Sambles, J.; Pudonin, F.; Yakovlev, V. Degenerate long range surface modes, supported on thin nickel films.*Opt. Commun.* **1996**, *132*.

[61] Fleming, A. J. A review of nanometer resolution position sensors: Operation and performance.*Sensors Actuators A Phys.* **2013**, *190*, 106–126, DOI: https://doi.org/10.1016/j.sna.2012.10.016.

[62] Passler, N. C.; Razdolski, I.; Gewinner, S.; Schöllkopf, W.; Wolf, M.; Paarmann, A. Second-Harmonic Generation from Critically Coupled Surface Phonon Polaritons.*ACS Photonics* **2017**, *4*, 1048–1053, DOI: 10.1021/acsphotonics.7b00118.

[63] Falge, H. J.; Otto, A. Dispersion of Phonon-Like Surface Polaritons on α-Quartz Observed by Attenuated Total Reflection.*Phys. Status Solidi* **1973**, *56*, 523–534, DOI: 10.1002/pssb.2220560213.

[64] Futamata, M.; Borthen, P.; Thomassen, J.; Schumacher, D.; Otto, A. Application of an ATR method in Raman spectroscopy.*Appl. Spectrosc.* **1994**, *48*, 252–260, DOI: 10.1366/0003702944028524.

[65] Knox, W. H.; Pearson, N. M.; Li, K. D.; Hirlimann, C. A. Interferometric measurements of femtosecond group delay in optical components.*Opt. Lett.* **1988**, DOI: 10.1364/OL.13.000574.

[66] Kovács, A. P.; Osvay, K.; Bor, Z.; Szipöcs, R. Group-delay measurement on laser mirrors by spectrally resolved white-light interferometry.*Opt. Lett.* **1995**, DOI: 10.1364/OL.20.000788.

[67] Diddams, S.; Diels, J.-C. Dispersion measurements with white-light interferometry.*J. Opt. Soc. Am. B* **1996**, DOI: 10.1364/JOSAB.13.001120.

[68] Gosteva, A.; Haiml, M.; Paschotta, R.; Keller, U. Noise-related resolution limit of dispersion measurements with white-light interferometers.*J. Opt. Soc. Am. B* **2005**, DOI: 10.1364/JOSAB.22.001868.

[69] Amotchkina, T. V.; Tikhonravov, A. V.; Trubetskov, M. K.; Grupe, D.; Apolonski, A.; Pervak, V. Measurement of group delay of dispersive mirrors with white-light interferometer.*Appl. Opt.* **2009**, DOI: 10.1364/AO.48.000949.

[70] Christau, S.; Möller, T.; Brose, F.; Genzer, J.; Soltwedel, O.; von Klitzing, R. Effect of gold nanoparticle hydrophobicity on thermally induced color change of PNIPAM brush/gold nanoparticle hybrids.*Polymer (Guildf).* **2016**, *98*, 454–463, DOI: 10.1016/j.polymer.2016.03.088.

[71] Guo, F.; Guo, Z. Inspired smart materials with external stimuli responsive wettability: A review.*RSC Adv.* **2016**, *6*, 36623–36641, DOI: 10.1039/c6ra04079a.

[72] Yu, Y.; Cirelli, M.; Kieviet, B. D.; Kooij, E. S.; Vancso, G. J.; de Beer, S. Tunable friction by employment of co-non-solvency of PNIPAM brushes.*Polymer (Guildf).* **2016**, *102*, 372–378, DOI: 10.1016/j.polymer.2016.08.029.

[73] Lewandowski, W.; Fruhnert, M.; Mieczkowski, J.; Rockstuhl, C.; Górecka, E. Dynamically self-assembled silver nanoparticles as a thermally tunable metamaterial.*Nat. Commun.* **2015**, *6*, 6590, DOI: 10.1038/ncomms7590.

[74] Gupta, S.; Agrawal, M.; Uhlmann, P.; Simon, F.; Stamm, M. Poly(n-isopropyl acrylamide)-gold nanoassemblies on macroscopic surfaces: fabrication, characterization, and application.*Chem. Mater.* **2010**, *22*, 504–509, DOI: 10.1021/cm9031336.

[75] Christau, S.; Moeller, T.; Genzer, J.; Koehler, R.; Von Klitzing, R. Salt-Induced Aggregation of Negatively Charged Gold Nanoparticles Confined in a Polymer Brush Matrix.*Macromolecules* **2017**, *50*, 7333–7343, DOI: 10.1021/acs.macromol.7b00866.

[76] Leroux, Y.; Eang, E.; Fave, C.; Trippe, G.; Lacroix, J. C. Conducting polymer/gold nanoparticle hybrid materials: A step toward electroactive plasmonic devices.*Electrochem. commun.* **2007**, *9*, 1258–1262, DOI: 10.1016/j.elecom.2007.01.015.

[77] Lian, Z.; Qi, S.; Zhou, J.; Schmid, F. Solvent determines nature of effective interactions between nanoparticles in polymer brushes.*J. Phys. Chem. B* **2015**, *119*, 4099–4108, DOI: 10.1021/jp511911g.

[78] Zhang, Y.; Guan, Y.; Zhou, S. Synthesis and volume phase transitions of glucose-sensitive microgels.*Biomacromolecules* **2006**, *7*, 3196–3201, DOI: 10.1021/bm060557s.

[79] Tokareva, I.; Minko, S.; Fendler, J. H.; Hutter, E. Nanosensors based on responsive polymer brushes and gold nanoparticle enhanced transmission surface plasmon resonance spectroscopy.*J. Am. Chem. Soc.* **2004**, *126*, 15950–15951, DOI: 10.1021/ja044575y.

[80] Homola, J., *Surface plasmon resonance (SPR) sensors*, 2006, DOI: 10.1007/b100321.

[81] Lange, H.; Juárez, B. H.; Carl, A.; Richter, M.; Bastús, N. G.; Weller, H.; Thomsen, C.; Von Klitzing, R.; Knorr, A. Tunable plasmon coupling in distance-controlled gold nanoparticles.*Langmuir* **2012**, *28*, 8862–8866, DOI: 10.1021/la3001575.

[82] Bloom, D. M.; Yardley, J. T.; Young, J. F.; Harris, S. E. Infrared up-conversion with resonantly two-photon pumped metal vapors.*Appl. Phys. Lett.* **1974**, *24*, 427–428, DOI: 10.1063/1.1655246.

[83] Bethune, D. S.; Smith, R. W.; Shen, Y. R. Optical Quadrupole Sum-Frequency Generation in Sodium Vapor.*Phys. Rev. Lett.* **1976**, *37*, 431–434, DOI: 10.1103/PhysRevLett.37.431.

[84] Boyd, R. W.; Scully, M. O. Efficient infrared imaging upconversion via quantum coherence Efficient infrared imaging upconversion via quantum coherence.*Appl. Phys. Lett.* **2000**, *77*, 3559–356, DOI: 10.1063/1.1329160.

[85] Heckmann, J.; Pufahl, K.; Franz, P.; Grosse, N. B.; Li, X.; Woggon, U. Plasmon-enhanced nonlinear yield in the Otto and Kretschmann configurations.*Phys. Rev. B* **2018**, *98*, 115415, DOI: 10.1103/PhysRevB.98.115415.

[86] Bloembergen, N.; Chang, R. K.; Jha, S. S.; Lee, C. H. Optical second-harmonic generation in reflection from media with inversion symmetry.*Phys. Rev.* **1968**, DOI: 10.1103/PhysRev.174.813.

[87] Boyd, R. W., *Nonlinear Optics*, 3rd; Academic Press: 2008.

[88] Rudnick, J.; Stern, E. A. Second-harmonic radiation from metal surfaces.*Phys. Rev. B* **1971**, *4*, 4274–4290, DOI: 10.1103/PhysRevB.4.4274.

[89] Sipe, J. E.; So, V. C.; Fukui, M.; Stegeman, G. I. Second harmonic generation at metal surfaces.*Solid State Commun.* **1980**, *34*, 523–526, DOI: 10.1016/0038-1098(80)90142-8.

[90] Gordon, J. G.; Ernst, S. Surface plasmons as a probe of the electrochemical interface.*Surf. Sci.* **1980**, *101*, 499–506, DOI: 10.1016/0039-6028(80)90644-5.

[91] Bo, L.; Claes, N.; Ingemar, L. Surface plasmon resonance for gas detection and biosensing.*Sensors and Actuators* **1983**, *4*, 299–304, DOI: 10.1016/0250-6874(83)85036-7.

[92] Wittekindt, C.; Fleckenstein, B.; Wiesmüller, K. H.; Eing, B. R.; Kühn, J. E. Detection of human serum antibodies against type-specifically reactive peptides from the N-terminus of glycoprotein B of herpes simplex virus type 1 and type 2 by surface plasmon resonance.*J. Virol. Methods* **2000**, *87*, 133–144, DOI: 10.1016/S0166-0934(00)00160-9.

[93] Dillon, P. P.; Daly, S. J.; Manning, B. M.; O'Kennedy, R. Immunoassay for the determination of morphine-3-glucuronide using a surface plasmon resonance-based biosensor.*Biosens. Bioelectron.* **2002**, *18*, 217–227, DOI: 10.1016/S0956-5663(02)00182-3.

[94] Homola, J.; Jiang, S.; Yu, Q.; Ladd, J.; Boozer, C.; Chen, S. DNA-Directed Protein Immobilization on Mixed Self-Assembled Monolayers via a Streptavidin Bridge.*Langmuir* **2004**, *20*, 8090–8095, DOI: 10.1021/la049867r.

[95] Homola, J. Surface plasmon resonance sensors for detection of chemical and biological species.*Chem. Rev.* **2008**, *108*, 462–493, DOI: 10.1021/cr068107d.

[96] Indyk, H. E.; Persson, B. S.; Caselunghe, M. C.; Moberg, A.; Filonzi, E. L.; Woollard, D. C. Determination of vitamin B12 in milk products and selected foods by optical biosensor protein-binding assay: Method comparison.*J. AOAC Int.* **2002**, *85*, 72–81.

[97] Oh, B. K.; Lee, W.; Lee, W. H.; Choi, J. W. Nano-scale probe fabrication using self-assembly technique and application to detection of Escherichia coli O157:H7.*Biotechnol. Bioprocess Eng.* **2003**, DOI: 10.1007/BF02942270.

[98] Cacciatore, G.; Petz, M.; Rachid, S.; Hakenbeck, R.; Bergwerff, A. A. Development of an optical biosensor assay for detection of β-lactam antibiotics in milk using the penicillin-binding protein 2x*.*Anal. Chim. Acta* **2004**, *520*, 105–115, DOI: 10.1016/j.aca.2004.06.060.

[99] Dupont, D.; Muller-Renaud, S. Quantification of proteins in dairy products using an optical biosensor.*J. AOAC Int.* **2006**, *89*, 843–848.

[100] Waswa, J. W.; Debroy, C.; Irudayaraj, J. Rapid detection of Salmonella enteritidis and Escherichia coli using surface plasmon resonance biosensor.*J. Food Process Eng.* **2006**, DOI: 10.1111/j.1745-4530.2006.00071.x.

[101] Soh, N.; Tokuda, T.; Watanabe, T.; Mishima, K.; Imato, T.; Masadome, T.; Asano, Y.; Okutani, S.; Niwa, O.; Brown, S. A surface plasmon resonance immunosensor for detecting a dioxin precursor using a gold binding polypeptide.*Talanta* **2003**, *60*, 733–745, DOI: 10.1016/S0039-9140(03)00139-5.

[102] Wu, C. M.; Lin, L. Y. Immobilization of metallothionein as a sensitive biosensor chip for the detection of metal ions by surface plasmon resonance.*Biosens. Bioelectron.* **2004**, *20*, 864–871, DOI: 10.1016/j.bios.2004.03.026.

[103] Gobi, K. V.; Tanaka, H.; Shoyama, Y.; Miura, N. Continuous flow immunosensor for highly selective and real-time detection of sub-ppb levels of 2-hydroxybiphenyl by using surface plasmon resonance imaging.*Biosens. Bioelectron.* **2004**, *20*, 350–357, DOI: 10.1016/j.bios.2004.02.003.

[104] Tanaka, H.; Shoyama, Y.; Gobi, K. V.; Miura, N.; Kim, S. J. Enhanced Sensitivity of a Surface-plasmon-resonance (SPR) Sensor for 2,4-D by Controlled Functionalization of Self-assembled Monolayer-based Immunosensor Chip.*Chem. Lett.* **2006**, *35*, 1132–1133, DOI: 10.1246/cl.2006.1132.

[105] Lechuga, L.; Marco, M. P.; Radjenovic, J.; Martínez, E.; Navarro, A.; Ramón, J.; Barceló, D.; Farré, M.; Mauriz, E. Part per trillion determination of atrazine in natural water samples by a surface plasmon resonance immunosensor.*Anal. Bioanal. Chem.* **2007**, *388*, 207–214, DOI: 10.1007/s00216-007-1214-2.

[106] Piliarik, M.; Homola, J. Surface plasmon resonance (SPR) sensors: approaching their limits?*Opt. Express* **2009**, *17*, 16505, DOI: 10.1364/oe.17.016505.

[107] Schottky, W. Über spontane Stromschwankungen in verschiedenen Elektrizitätsleitern.*Ann. Phys.* **1918**, *362*, 541–567, DOI: 10.1002/andp.19183622304.

[108] Piliarik, M.; Homola, J. Surface plasmon resonance (SPR) sensors: approaching their limits?*Opt. Express* **2009**, DOI: 10.1364/OE.17.016505.

[109] Yeatman, E. M. Resolution and sensitivity in surface plasmon microscopy and sensing.*Biosens. Bioelectron.* **1996**, *11*, DOI: 10.1016/0956-5663(96)83298-2.

[110] Prabowo, B. A.; Purwidyantri, A.; Liu, K. C. Surface Plasmon Resonance Optical Sensor: A Review on Light Source Technology.*Biosensors* **2018**, *8*, DOI: 10.3390/bios8030080.

[111] Delaubert, V.; Treps, N.; Lassen, M.; Harb, C. C.; Fabre, C.; Lam, P. K.; Bachor, H. A. TEM10 homodyne detection as an optimal small-displacement and tilt-measurement scheme.*Phys. Rev. A - At. Mol. Opt. Phys.* **2006**, *74*, 1–10, DOI: 10.1103/PhysRevA.74.053823.

[112] Fox, M., *Quantum Optics: an Introduction*; Fox, M., Ed.; Oxford University Press: 2006, DOI: 10.1017/CBO9781107415324.004.

[113] Loudon, R., *The Quantum Theory of Light*, 3rd; Oxford University Press: 2005, DOI: 10.1119/1.1987930.

[114] Walls, D. F. Squeezed states of light.*Nature* **1983**, *306*, 141–146, DOI: 10.1038/306141a0.

[115] Ferdinand, A. R.; DiMario, M. T.; Becerra, F. E. Multi-state discrimination below the quantum noise limit at the single-photon level.*npj Quantum Inf.* **2017**, 1–7, DOI: 10.1038/s41534-017-0042-2.

[116] Escher, B. M.; De Matos Filho, R. L.; Davidovich, L. General framework for estimating the ultimate precision limit in noisy quantum-enhanced metrology.*Nat. Phys.* **2011**, *7*, 406–411, DOI: 10.1038/nphys1958.

[117] Yuen, H. P.; Chan, V. W. S. Noise in homodyne and heterodyne detection.*Opt. Lett.* **1983**, *8*, 177–179, DOI: 10.1364/OL.8.000345.

[118] Carleton, H. R.; Maloney, W. T. A Balanced Optical Heterodyne Detector.*Appl. Opt.* **2008**, *7*, 1241, DOI: 10.1364/ao.7.001241.

[119] Schumaker, B. L. Noise in homodyne detection.*Opt. Lett.* **1984**, *9*, 189, DOI: 10.1364/ol.9.000189.

[120] Zhang, H. Q.; Boussaad, S.; Tao, N. J. High-performance differential surface plasmon resonance sensor using quadrant cell photodetector.*Rev. Sci. Instrum.* **2003**, *74*, 150–153, DOI: 10.1063/1.1523649.

[121] Song, F. Detection of oligonucleotide hybridization at femtomolar level and sequence-specific gene analysis of the Arabidopsis thaliana leaf extract with an ultrasensitive surface plasmon resonance spectrometer.*Nucleic Acids Res.* **2002**, *30*, 72e–72, DOI: 10.1093/nar/gnf072.

[122] Vahlbruch, H. Squeezed Light for Gravitational Wave Astronomy, Ph.D. Thesis, Gottfried Wilhelm Leibniz Universität Hannover, 2008.

[123] Toma, M.; Jonas, U.; Mateescu, A.; Knoll, W.; Dostalek, J. Active control of SPR by thermoresponsive hydrogels for biosensor applications.*J. Phys. Chem. C* **2013**, *117*, 11705–11712, DOI: 10.1021/jp400255u.

[124] Slavík, R.; Homola, J. Ultrahigh resolution long range surface plasmon-based sensor.*Sensors Actuators, B Chem.* **2007**, *123*, 10–12, DOI: 10.1016/j.snb.2006.08.020.

[125] GE Healthcare UK Ltd. Biacore X100 Datasheet.

[126] Reichert Inc. Reicher 2SPR Specifications.

[127] PCbiosensors EVA 2.0 Specifications.

[128] GE Healthcare UK Ltd. Biacore T200 Datasheet.

[129] Bio-Rad Laboratories Inc. Bio-Rad XPR36 Datasheet.

[130] Schuck, P.; Zhao, H. In *Surf. plasmon Reson.* Springer: 2010, pp 15–54, DOI: 10.1007/978-1-60761-670-2.

[131] Nenninger, G. G.; Clendenning, J. B.; Furlong, C. E.; Yee, S. S. Reference-compensated biosensing using a dual-channel surface plasmon resonance sensor system based on a planar lightpipe configuration.*Sensors Actuators, B Chem.* **1998**, *51*, 38–45, DOI: 10.1016/S0925-4005(98)00218-4.

[132] Abbott, B. P. et al. Observation of gravitational waves from a binary black hole merger.*Phys. Rev. Lett.* **2016**, *116*, 1–16, DOI: 10.1103/PhysRevLett.116.061102.

[133] Stevenson, A. J.; Gray, M. B.; Bachor, H.-A.; McClelland, D. E. Quantum-noise-limited interferometric phase measurements.*Appl. Opt.* **1993**, *32*, 3481, DOI: 10.1364/ao.32.003481.

[134] Nelson, S. G.; Johnston, K. S.; Yee, S. S. High sensitivity surface plasmon resonance sensor based on phase detection.*Sensors Actuators, B Chem.* **1996**, *35*, 187–191, DOI: 10.1016/S0925-4005(97)80052-4.

[135] Shen, S.; Liu, T.; Guo, J. Optical phase-shift detection of surface plasmon resonance.*Appl. Opt.* **2008**, *37*, 1747, DOI: 10.1364/ao.37.001747.

[136] Deng, S.; Wang, P.; Yu, X. Phase-sensitive surface plasmon resonance sensors: Recent progress and future prospects.*Sensors (Switzerland)* **2017**, *17*, DOI: 10.3390/s17122819.

[137] Fan, W.; Lawrie, B. J.; Pooser, R. C. Quantum plasmonic sensing.*Phys. Rev. A - At. Mol. Opt. Phys.* **2015**, *92*, 1–5, DOI: 10.1103/PhysRevA.92.053812.

[138] Pooser, R. C.; Lawrie, B. Plasmonic Trace Sensing below the Photon Shot Noise Limit.*ACS Photonics* **2016**, *3*, 8–13, DOI: 10.1021/acsphotonics.5b00501.

[139] Laurent, P.; Souharce, G.; Duchet-Rumeau, J.; Portinha, D.; Charlot, A. 'Pancake' vs. brush-like regime of quaternizable polymer grafts: an efficient tool for nano-templating polyelectrolyte self-assembly.*Soft Matter* **2012**, *8*, 715–725, DOI: 10.1039/C1SM06362F.

[140] Pufahl, K.; Grosse, N. B.; Woggon, U. K. The quantum noise limit of surface-plasmon resonance sensing.

[141] Pufahl, K.; Heckmann, J.; Woggon, U. K.; **Grosse**, **N. B.** In *Proc. META'16*, 2016, pp 1266–1267.

[142] Heckmann, J.; **Pufahl**, **K.**; Grosse, N. B.; Sipe, J. E.; Woggon, U. K. In *Proc. META'16*, 2016, pp 1411–1412.

[143] **Pufahl**, **K.**; Kesal, D.; Franz, P.; Heckmann, J.; Grosse, N. B.; Christau, S.; Lehmann, M.; von Klitzing, R.; Woggon, U. K. In, NNN TELECOM workshop Le Mans: 2017.

[144] Franz, P.; Heckmann, J.; **Pufahl**, **K.**; Grosse, N. B.; Woggon, U. K. In *Nonlinear Opt.* 2017, NF2A.3, DOI: 10.1364/NLO.2017.NF2A.3.

[145] Pufahl, K.; Boyaciyan, D.; Heckmann, J.; Franz, P.; Grosse, N. B.; von Klitzing, R.; **Woggon**, **U. K.** In *Front. Opt. / Laser Sci.* Optical Society of America: 2018, FW6E.2.

Acknowledgements

First, I would like to express my sincere gratitude to Ulrike Woggon who has given me the opportunity to work on symmetric cladding thin-film waveguides. She has been very patient and allowed me to take the time I needed for my curiosity and to understand the concepts of SCTWs.

I would like the thank the whole of AG Woggon for its continuous support throughout the last four years while working on this thesis. It has been a very pleasant time with all of you. I have learned a lot from you and I consider that a very important set of skills. In particular, Nicolai has told me so many tips and tricks for working with optics that have proven very useful. Many times, it these small tricks – not written in any book – that not only make your life easier, but also decide whether a complicated experiment succeeds or fails. Basti, Mirco and Oliver have contributed in many ways to this thesis, most notably by having scientific discussions over coffee. Jenny is thanked for help navigating through the bureaucracy jungle. She always had an eye on forms and deadlines thereby allowing me to focus on scientific work instead.

I also thank Regine von Klitzing and her group who have broad polymer brushes to my attention. In particular, Dikran Boyaciyan who synthesized the Au:PNIPAM samples as well as other brush films that did not make it into this thesis.

I also thank everyone who was involved on the experimental side by preparing samples and helping with the measurements:

Chris Scharfenorth and Heike Grundlach for providing the necessary optical coatings and help with cleaning optical components.

Sven Peters and Adrian Blümich from Sentech Instruments for contributing ellipsometry measurements of the PNIPAM samples.

Christoph Fahrenson for the SEM microscopy images and preparation that was done at the ZELMI, TU Berlin.

Michael Schneider for help and introduction into AFM microscopy that was very helpful for the sample characterization.

The team of the mechanical workshop for machining all the custom parts that were required for the ATR setup.

I express my gratitude to the Deutsche Forschungsgemeinschaft (DFG) that provided the funding for my position as a researcher which enabled me to write this thesis.

I thank Charlotte Köhler and Hanna Schulte-Strotmes for great support preparing the manuscript.

A very special thanks goes to my parents that have continuously supported of my curiosity and guidance throughout my life. Finally, I would like to express gratitude to Ina Budde, my lovely partner, who supported me throughout this thesis and who has been very patient with the creative mess surrounding me. Thank you.